Master of Science Thesis · July 4th 2014

Temperature and Load Effects in Modelling and Experimental Verification of Acoustic Emission Signals for Structural Health Monitoring Applications

M.J.G.N. Boon M.Sc.

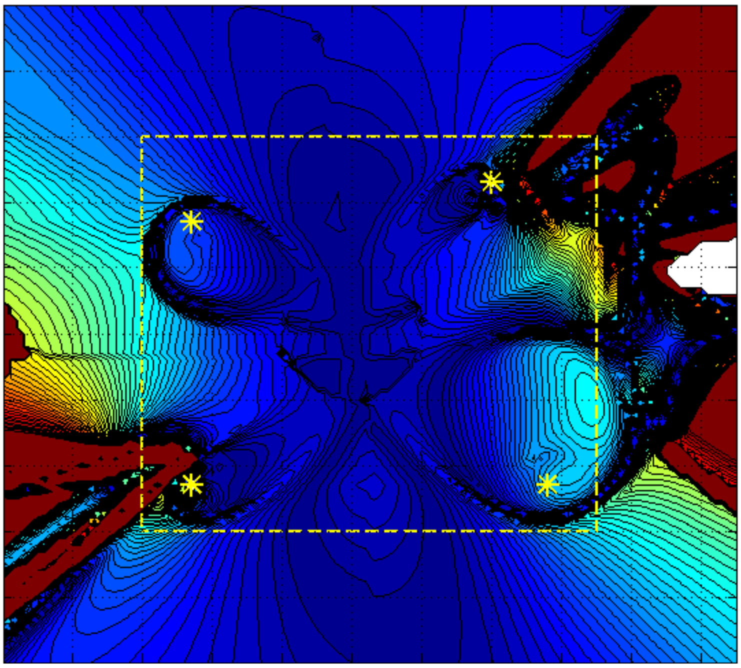

Faculty of Aerospace Engineering · Delft University of Technology

Temperature and Load Effects in Modelling and Experimental Verification of Acoustic Emission Signals for Structural Health Monitoring Applications

Master of Science Thesis

For obtaining the degree of Master of Science in Aerospace Engineering
at Delft University of Technology

M.J.G.N. Boon M.Sc.

July 4^{th} 2014

Faculty of Aerospace Engineering – Delft University of Technology

The work in this thesis was supported by Cranfield University. Their cooperation is gratefully acknowledged.

Delft University of technology
Faculty of Aerospace Engineering
Department of Aerospace Structures and Materials
Structural Integrity & Composites Chair

GRADUATION COMMITTEE

Dated: 04-07-2014

Chair holder:

____
prof.dr.ir. R. Benedictus

Committee members:

____
dr. M.J. Martinez

____
dr. ir. D. Zarouchas

____
dr. D. Gagar

____
dr.ir. W.J.C. Verhagen

Sometimes I am thinking for hours, and still I am not getting anything down on paper,
another time I achieve exactly the same results in five minutes.

H. Finkers (Comedian)

Abstract / Summary

The present study focuses on understanding the effect of load and temperature on Acoustic Emission (AE) signal propagation in an Aluminium 2024-T3 panel. In addition, the ability of an AE system to locate damage under these operational and environmental conditions was evaluated. The work was performed in two stages. In stage one, the wave group velocities of guided Lamb waves were measured for a range of temperatures from -40 ˚C to 70 ˚C. At each temperature level, six different static loads were applied that ranged from 0 MPa to 250 MPa in increments of 50 MPa. A mathematical analytical model for the effect of temperature on the wave group velocities was re-produced in order to verify it through experimental and FEM results. Furthermore, experimental and FEM results have been obtained for the effect of load and the combined case. It was observed that the variation of temperature and load altered the wave group velocities. The results showed that an increase in the temperature resulted in a decrease of the wave group velocity and vice versa. Furthermore, external applied loads resulted that the change group velocity varies linearly with increasing stress and has a sinusoidal dependence with the angle between sensor path and loading direction. Which meant that the wave group velocity decreased for small angles, increased for large angles and varied with a sinusoidal behaviour for the other angles between the propagation path and the loading direction. The effect of temperature and load can be super imposed onto each other. Experimentally obtained wave group velocities with temperature were within an error of 6% to the analytical solution and for the FEM results this was within 3%. In stage two, a representative AE signal, simulating a fracture phenomenon was emitted from a randomly selected point. Using values of wave velocity measured in stage one, the location of the representative AE signal under these conditions was calculated and errors were determined. It was found that the location algorithm was not sensitive to wave group velocities changes due to temperature and loads, thus providing an accurate location of the source within 1cm, for a specimen size of 65 by 60 cm. The experimentally obtained localization results were also supported with results from a numerical model that calculated location errors for many locations in and outside the array. The effects of temperature and load were taken into account in the Time Differences Of Arrival (TDOA) function for a known location. These TDOA were then fed into a location algorithm (Geiger’s method). It was found that location errors due to temperature or load were within 1.5 cm and were at some areas more significantly affected than at other locations. The reduced location accuracy of these source locations can be related to the angle dependent effect of load on wave group velocities. Source locations that have an angle between most sensors paths and loading direction that fits the largest change in wave velocity were found to be more significantly affected. The experimental results also presented problems with threshold selection during the experiments. A low AE threshold could translate into too much noise in the acquired signals, which can result in wrongfully triggering, while a high AE threshold could translate into incorrect group velocity measurements because a later part of the waveform would be used for triggering. Therefore the development of an threshold independent trigger mechanism is a recommendation for further research as well as investigating the effect of EOC in complex or composite structures.

Preface

I am pleased to be able to present this master thesis. I could not have done this without the help and support of many people, which I would like to thank for all they have done during my studies and especially these past nine months when I did my thesis project.

First of all, I would like to thank my supervisor Dr. Marcias Martinez who helped me structure the entire thesis very well from the beginning and supported me with whatever I needed when I needed it, also his enthusiasm and jokes every now and then were very much appreciated. My second supervisor Dr. ir. Dimitrios Zarouchas supported me very well during the experiments and his door was always open for questions. Furthermore, I would like to thank ir. Darun Baranzanchy. With his help explaining all the previous work he had done leading up to my thesis. I also would like to thank Maria Barroso Romero for having numerous discussions with me. In the beginning the scope of this thesis benefited significantly from the discussions with Professor Peter Foote and dr. Daniel Gagar from Cranfield University, also later discussion proved to be fruitful.

During the experimental phase I worked with a new AE system from Vallen Systeme. I would like to thank them and in particular Thomas Thenikl to explain the workings of the system and discuss the problems I faced with it during many conference calls. Also feedback given by him on the experiments was very relevant.

Then I would like to thank two of my best friends Hung Tran and Kelvin Ng for being my friends first of all but also because of their support and taking part in discussions related to my thesis. Last but not least I would like to thank my family and in specific my father and mother who have been a great support during this thesis.

When looking back on this thesis I am happy to have chosen this topic of SHM. It was interesting and it taught me things I wanted to learn; including being more skilled in programming and FEM methods, focus and persistence. Furthermore, it was a good decision to do my thesis within the university, which offered me a great opportunity in doing research and seeing how research is done by others. The student room in which many master students were located to do their master thesis was a nice environment to be working in. It was good to be around people who are in the same boat; it is both enjoyable and supporting at the same time. Finally, I would like to thank the reader of this thesis for putting the time and effort to read it.

Abbreviations

AE	Acoustic Emission
CBM	Condition Based Monitoring
CTE	Coefficient of Thermal Expansion
EOC	Environmental and Operational Conditions
FE(M)	Finite Element (Method)
GW	Guided Wave
SHM	Structural Health Monitoring
NDE	Non Destructive Evaluation
NDT	Non Destructive Testing
OBS	Optimum Baseline Subtraction
SHM	Structural Health Monitoring
SH	Shear Horizontal wave
SV	Shear Vertical wave
TDOA	Time Difference of Arrival
TOA/TOF	Time of Arrival / Flight

Frequently used symbols

ρ	Density
ω	Angular frequency
Δt	Time step
σ	Stress
A_0	Anti-symmetric natural wave
d_{ij}	Piezoelectric coupling matrix
E	Stiffness matrix
fh	Frequency-thickness
f	Frequency
k	Wave number
L_e	Maximum element size of mesh element
S_0	Symmetric natural wave
v_g	Group velocity
v_L	Longitudinal velocity
v_p	Phase velocity
v_T	Tangential velocity

Table of Contents

List of Figures

List of Tables

Chapter 1: Introduction

In order to ensure structural integrity, aircraft structures are subjected to regular maintenance programs. Early damage detection is preferable and helps to reduce maintenance and repair costs. However, these regular maintenance programs based on manual non-destructive inspection can involve complicated time-consuming operations impacting the maintenance costs [1]. Reduction in operational and maintenance costs of aircraft structures can be achieved using Structural Health Monitoring (SHM) methods, which provide continuous assessment of structural integrity during service [2]. Elastic waves travelling inside the structure can be used for Non Destructive Testing (NDT) of the structural health and so are useful for application in SHM techniques in a real time operational environment. Aircraft contain many thin walled (plate-like) structures (especially in the skin) which facilitate propagation of elastic waves, also referred to as guided Lamb Waves. This means that the waves are guided by the structural elements of an aircraft. These waves can be detected via arrays of embedded or permanently attached transducer networks in structures. The presence of damage inferred with the monitoring system operating in either the active or passive mode. The active mode involves actuation and detection of these waves, while the passive mode involves only detection of the waves dynamically generated from a damage site [2]. These SHM techniques have the ability to assess the structural health on a real time basis while the aircraft is in-service, which can positively influence aircraft maintenance procedures and enable the transition from being schedule driven to becoming condition based. This can lead to a reduction in the scheduled maintenance time, a reduction in maintenance cost and can help to maintain safety [2].

During its lifetime the aircraft structure faces many different Environmental and Operational Conditions (EOC), sustaining fatigue, loads and extreme temperature variations. These conditions also affect the wave propagation in the structure and the SHM system's response. The influence of these EOC on the measured signal need to be understood to be able to correctly detect and localize damage in a real time operational service environment. Load and temperature have been reported as the most influential EOC on received signals [3-4]. The thesis described in this report is focused on understanding how loads and temperature affect the propagation of acoustic waves and the ability of AE algorithm's to detect and localize damage in a structure.

1.1 Research Problem

Environmental and Operational Conditions (EOC), in particular temperature and loads affect the properties of guided Lamb waves and as such their ability to correctly detect and localize damage in SHM applications. In recent years, research on these EOC in the field of acoustic based SHM mainly focused on understanding the effect of EOC for the active guided Lamb wave approach. Furthermore the literature has not focused on investigating combined effects of multiple EOC. Sohn [3] states that environmental and operational variation is one of the main obstacles for deploying active SHM system for in-service structures because these changes can often mask subtler structural changes caused by damage [4].

Less attention has been given to investigate how EOC affect the AE technique. The advantage of AE is that the recorded signal is entirely caused by the damage and the EOC will affect the wave propagation properties. The AE approach has no influence of an actuated signal as is in the active SHM approach. The actuated signal makes it difficult to recognise the part of the signal that is related to damage, which is important for damage detection. Therefore, false positives due to effect of EOC may not be so much of a problem in AE approach as compared to the active approach. However, the waveform of an AE signal is not a Hanning window, which is optimized to reduce the bandwidth. Therefore it is more prone to dispersion, which is the phenomenon that the wave velocity depends on the frequency. For localization purposes one constant velocity of the wave is desirable. These differences between the active and AE SHM approach result that the waveform and velocity of an AE signal is affected differently to temperature and loads than the active SHM approach. Gagar *et al.* [5] have shown that AE signals can be measured in complex wing-box structures. They showed that there is signal coupling between the spar and the skin, which enables signal transfer from spars to skin, providing that the AE technique is effective for location analysis in complex structures. As such AE is a promising technique for damage location analysis. It is therefore valuable to investigate how AE signals are affected by EOC and how that influences the localization capability in order to assess this technology for a real time operational service environment. The combination of these two techniques in a hybrid (active-passive) SHM system can potentially provide reliable results. To develop a hybrid system, first the effects of EOC on AE system should be understood to be able to understand how to combine both systems in one.

1.2 Research Objective & Research Questions

As already stated in the introduction this research project aims to understand the effect of EOC (in specific; temperature and load) on AE signals and therefore the objective can be formulated as:

> *To understand how and to what extent load and temperature affect Acoustic Emission signals and damage localization in a simple metal plate structure and to assess this technique for real time monitoring of aircraft structures in an operational service environment.*

Based on the afore mentioned objective, the main research question can be formulated as follows:

> *How and to what extent does load and temperature affect the measured Acoustic Emission signal and the ability to detect and localize damage?*

The present study was focused on understanding the effect of load and temperature on the AE signal propagation and the ability of an AE system to identify and locate damage, both numerically and experimentally. In order to answer the main research question three sub questions have been developed and can be stated as follows:

1) How does load or temperature affect the propagation properties of elastic waves?

2) How load or temperature affects the capability to localize damage of AE signals?

3) How do FEM simulations with influence of EOC compare to experimentally obtained results in metallic plates?

To indicate the boundaries of this research project a short discussion about what is out of scope will follow now. First of all Ostachowicz *et al.* [6] described four factors of effective diagnostics for SHM. From those four factors this thesis focussed on detection and localization of damage and not on identification or prediction of damage and future safe life. Secondly the sensitivity change of the sensor with temperature was out of scope. This research focused on simple metal plate like structures and not on complex or composite structures. Furthermore, this thesis focused on the effect of homogenous temperature change and static loads, all other EOC were not investigated, such as humidity, fatigue etc. Also damage is simulated by a source and real damages were not investigated.

1.3 Research Approach

To answer the research question outlined above, the chosen methodology consisted of a combination of the FE method and an experimental study. The overview of the work to be performed has been organized as shown in Figure 1.3.1.

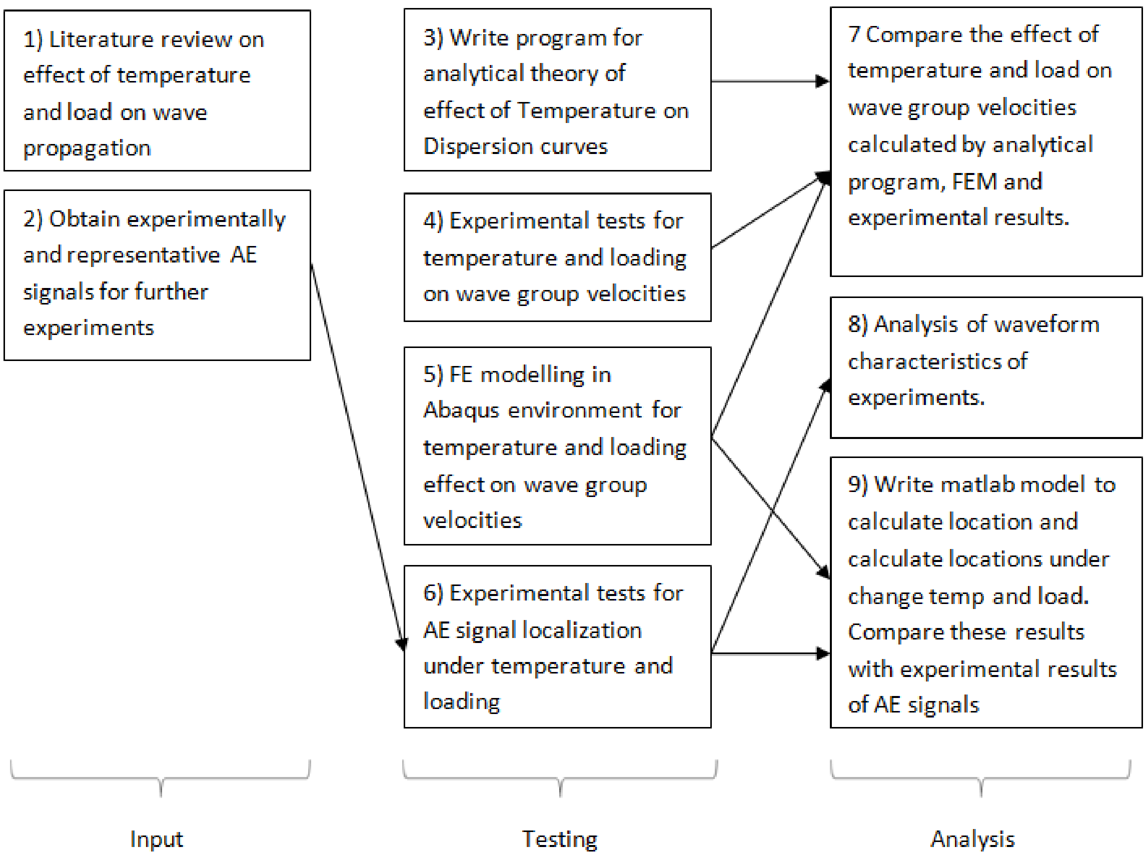

Figure 1.3.1: Overview of project scope.

The remainder of this thesis was performed in three stages. The first step in this work was to perform a literature review to understand the current state of the research in this field. More specifically it meant to investigate the current understanding of the effect of temperature and load on the acoustic based SHM methods for thin metal plates. Also a representative AE signal has been acquired with a pencil lead break test (Hsu-Nielson test, [7]).

In the second stage of this work an mathematical analytical program that incorporates the effect of temperature on the dispersion curves is reproduced from the literature to be able to verify this theory with experimental and FE results. The wave group velocities under varying conditions of temperature and load have been measured experimentally in an active approach. These experiments have been verified with the FE method in the (Abaqus/CAE) modelling environment [8]. In order to understand the effect of temperature and applied load on the AE signals, a homogenous temperature from -40 ˚C to 70 ˚C in 9 steps was considered. At each temperature level, six different static loads were applied that ranged from 0 to 250 MPa (in steps of 50 MPa). Also a design of experiment study was conducted in order to evaluate the effect of both temperatures and loads on AE signal localization using the representative AE signal emitted from a random location.

Then in the third stage of this thesis the analysis was done to compare the result of the FEM modelling, analytical and the experimental results of the change in wave group velocity due to temperature and load. Also a location algorithm (Geiger's method) has been written to calculate locations of many simulated sources. The travel time from source to sensors of these simulated sources is updated for the changes in wave velocity due to temperature and load. In this way, location errors that were introduced in the location algorithm due to the effect of temperature and load could be measured. Results from this program were also compared to the experimental results obtained.

1.4 Report structure

The remaining part of this report has been structured as follows. Firstly in Chapter 2 the results of a literature review about the effect of temperature and load on wave propagation are presented. Next, the third chapter describes the analytical solutions for the effect of temperature on the dispersion curves. In this chapter, temperature invariant points are also discussed. Then, in chapter 4 the test methodology is explained, also the details of the experimental setup and the FE models are discussed. Chapter 5 will present the results from the changes in wave group velocities with temperature and load. Furthermore, experimental results of location sensitivity of AE signals under temperature and load is provided. Then, Chapter 6 numerically investigates the localization accuracy under the effects of temperature and load. Finally, Chapter 7 discusses the conclusions of this research and provide recommendations for further research.

Chapter 2: Literature Study

The current literature study discusses the effects and current problems of EOC (in particular temperature and load) on guided Lamb waves for SHM monitoring purposes. In recent years, research into these EOC on the field of SHM has mainly focused on understanding the individual effects of several EOC for an active guided Lamb wave approach. However less attention has been given to passive approaches such as AE. Propagation of waves in thin plates for the active approach is described by Lamb waves. For AE in thin plates the 2D assumption that is made in the Lamb wave theory can also be made resulting in the same physical description of how waves propagate for both approaches but with changes in the waveform. Therefore the effects of EOC on both active and passive SHM approaches are discussed in this chapter. However, the passive approach will only be focused on AE. The literature from the active approach is used to understand the AE approach. As discussed in the introduction, temperature and load not only affect the way in which the wave propagates but also affects the SHM system sensitivity by affecting the properties of the transducers.

The structure of this chapter is based on how the signal propagates through the SHM process. The active approach for SHM starts with actuating a signal with a transducer while for the passive approach the signal is actuated by a fracture phenomenon inside or on the plate. The wave then propagates through the plate to several transducers where it can be recorded. After the signal has been received, post processing starts and the analysis of the signal is executed by establishing whether damage is present in the structure.

The flow of the signal as described above results in the following structure of this chapter. It starts with background information about the current approach how to maintain safety of aircraft structures, followed by a general introduction to Lamb waves and SHM. Section 2.3 deals with the AE technique and the signal features of typical AE signals and Section 2.4 will explain the workings and properties of piezoelectric transducers which are used for measuring elastic waves in structures. Section 2.5 deals with the effect of temperature and load on the wave propagation properties in the plate for the active approach. Next, in Sections 2.6 compensation techniques for the effect of temperature in an active SHM approach will be discussed. Section 2.7 discusses localization of damage for both active and passive SHM approaches. Finally Section 2.8 summarizes the main conclusions that are important regarding the modelling and further parts of this report.

2.1 Background

When aircraft structures are in service damage is inevitable and can occur due to four degradation mechanisms: fatigue, environmental, accidental damage [9] and overloading. To maintain structural integrity or in other words the ability of a structure to function as required [10] a maintenance program is needed. Maintenance can be defined as "*the process of ensuring that a system continually performs its intended function at its designed-in level of reliability and safety*" by Kinnison [11, p. 34].

There are basically three design paradigms applied in aircraft structures: the 'safe life', 'damage tolerant', and 'fail safe' approaches. The first one assumes that fatigue failure is not supposed to occur in the design life of a structural element which, is assured by testing a component for fatigue and replacing it at the end of this life [10]. Therefore it is also called 'safety by replacement'. The second approach is the damage tolerant approach, which accounts for damage and is based on worst-case fatigue growth calculations, thus ensures that fatigue cracks don't grow beyond a certain length [10]. This approach is supported by inspection intervals also based on the crack growth rate and it is therefore also called 'safety by inspection'. Thirdly the 'fail safe' concept is a damage tolerant approach based upon multiple load paths. When one load path fails due to damage all the load is taken by another load path, this is therefore also called 'safety by design'.

Most aircraft parts are designed based on a damage tolerant philosophy and therefore inspections are required in the maintenance programs. This takes the aircraft out of service for its scheduled maintenance check. NDT methods are already used during these maintenance checks. However bringing these methods to an operational environment is the next step. The maintenance approaches used differ per type of failure, which can be gradual, time delayed or sudden failures. The different types of failures can be maintained with different approaches. Such maintenance approaches can be divided into preventive (actions before functional failure) and corrective maintenance (actions after functional failure) [10]. All these maintenance programs involve complicated time-consuming operations impacting the maintenance costs [1] and safety. SHM methods have the ability to change aircraft maintenance procedures from scheduled driven to condition based. This will lead to many advantages: 1) cutting down on period on which structures are offline, 2) cost savings and reducing labour, 3) confidence levels in operating the structure would increase, and 4) safety of the users is better ensured [2]. Therefore, the aerospace industry addresses an increasing demand for lower operational and maintenance costs by pointing to Structural Health Monitoring (SHM) strategies that can assess the structural integrity during service [12].

2.2 Introduction to Acoustic based SHM

This Section discusses general concepts of acoustic based SHM and compares the active approach to the AE approach, to see how they relate to each other.

SHM as discussed in the introduction is a way of detecting and characterizing the structural damage, and can be described as "*the process of acquiring and analyzing data from on-board sensors to evaluate the health of a structure.*" [13, p. 4]. The health of a structure relates to the structural integrity which is defined by J. Homan as "*A measure of the quality of construction and the ability of the structure to function as required*" [10, p. 10]. When the structural health is maintained the structural integrity is also preserved. The effectiveness of SHM approaches can be characterized according to Ostachowicz [6] in four levels: 1) detection (whether damage exists), 2) location (locating the damage), 3) identification (Determining damage type & size) and 4) prediction (Providing information regarding the remaining safe operational time until next repair). SHM systems can be broadly defined into two approaches; active and passive approaches. In the active approach a signal is actuated bu the user at a specified time. The signal propagates through the plate and is affected by attenuation, EOC and the damage. As discussed in section 1.2 it is difficult to distinguish the effect of EOC from signal changes due to damage, which leads to an increase of false positives. In the passive SHM approach such as AE the signal originates from a damage site in the plate. The signal is then affected by the attenuation, dispersion and EOC during propagation in the plate. Detecting damage in the recorded signal in the AE approach does not require the subtraction of the actuated signal as in the active approach. Therefore any recorded signal is already due to damage and will only be affected by EOC. Therefore the lack of actuated signal in the AE approach will lead to fewer false positives due to the effect EOC. On the other hand, the type of waves in the active approach can be controlled in frequency content and time of excitation, which has advantages as will be shown later in this Section. In the active approach the state of the structure can be also assessed at any given time but with the passive approach only indications of structural degradation can be assessed when they occur and therefore this doesn't give an overview of the current structural health. Table 2.1 summarizes the previously discussed properties of both approaches for comparison.

Table 2. 1: Properties of both active and passive SHM approach.

Active SHM approach	Passive SHM approach
Measurement of structural health can always take place and takes a short time.	Indication of damage only during structural degradation, monitoring is continuous.
Recorded signal contains an actuated wave from and possible signal changes from the damage and EOC.	Recorded signal wave contains possible signal changes from the damage and EOC
False positives may occur because the actuated wave is affected by EOC.	False positives due to EOC are less likely to occur, due to lack of a user actuated signal.
Actuated waveform can be controlled.	Waveform cannot be controlled.
Wave affected by temperature and load.	Wave affected by temperature and load.
Received signal gives overview of the damage in the entire specimen .	Received signal indicate structural degradation but it does not give overview of the entire structural health.
Location where the signal is actuated is not the damage location.	Location where the signal is actuated is the damage location.

The types of waves that are used to describe the propagation of waves in plates in both the active and passive approach are Lamb waves. According to Croxford *et al.* [14] Lamb waves are very useful for SHM: "*Acoustic waves in the tens to hundreds of kilohertz range are arguably the only detection mechanism that combines reasonable sensitivity to damage with significant propagation range*" [14, p. 2961].

Guided waves (GW's) are a type of elastic waves because they propagate in elastic mediums along the path of the structure. Lamb waves are guided waves that are bounded by two surfaces and can be divided into longitudinal P-waves and shear waves (Shear Vertical SV or Shear Horizontal SH). Depending on the distribution of displacements two forms of Lamb waves can be distinguished which are the symmetric modes, written as S_0, S_1, S_2…S_n, and the anti-symmetric modes, written as A_0, A_1, A_2…A_n, both forms are represented in Figure 2.2.1. The S_0 is also called the extensional wave while the A_0 is called the flexural wave, both are called natural waves.

a) b)

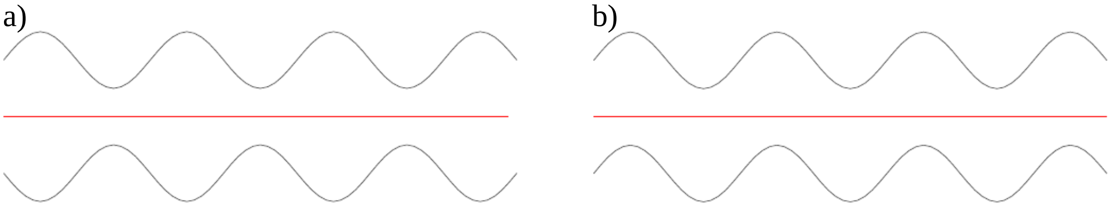

Figure 2.2.1: Schematic representation of Lamb wave modes in cross Section of a finite plate; a) symmetric (longitudinal P-wave); and b) anti-symmetric (out of plane SV- & SH-wave) [15].

The guided Lamb waves can be actuated and sensed with piezoelectric transducers. When a piezoelectric transducer actuates a Lamb wave both a symmetric and an anti-symmetric wave will be sent out simultaneously. The two symmetric and anti-symmetric Lamb waves have their own sensitivities to damage and as such they are useful in different applications. The sensitivity of the natural symmetric mode or S_0 depends on the depth of discontinuity and it is therefore good for measuring cracks. The sensitivity of the natural anti-symmetric mode or A_0 has greatest sensitivity on the surface of the objects and can serve as an indicator of delamination, transverse cracks and layer separation in composites [6].

Guided Lamb waves propagate large distances in plates but they are dispersive, which means that the velocity depends on the material properties and the frequency-thickness product of the wave and plate. This results in dispersion curves, of which an example is given in Figure 2.2.2. Because every wave travelling at a particular frequency has its own velocity when interpreting the signal it is most convenient to have a frequency range that is as narrow as possible (narrow bandwidth). Therefore one advantage that the active method has over the passive method is that using a narrow band can minimize the dispersion, and for example this can be achieved by applying a Hanning window. This window combines a carrier wave and modulation wave into a wave packet as indicated in Figure 2.2.3.

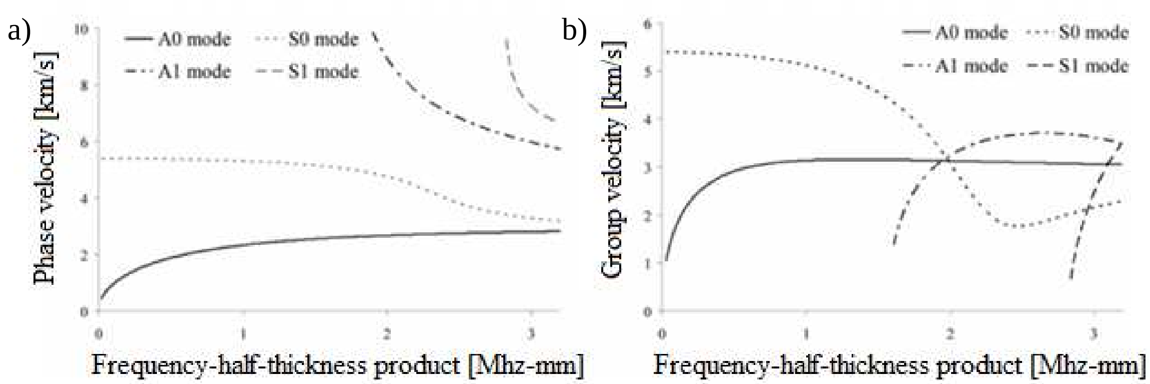

Figure 2.2.2: Dispersion curves for of isotropic plate with Young's modulus of 69 [GPa]; a) phase velocity; b) group velocity [2].

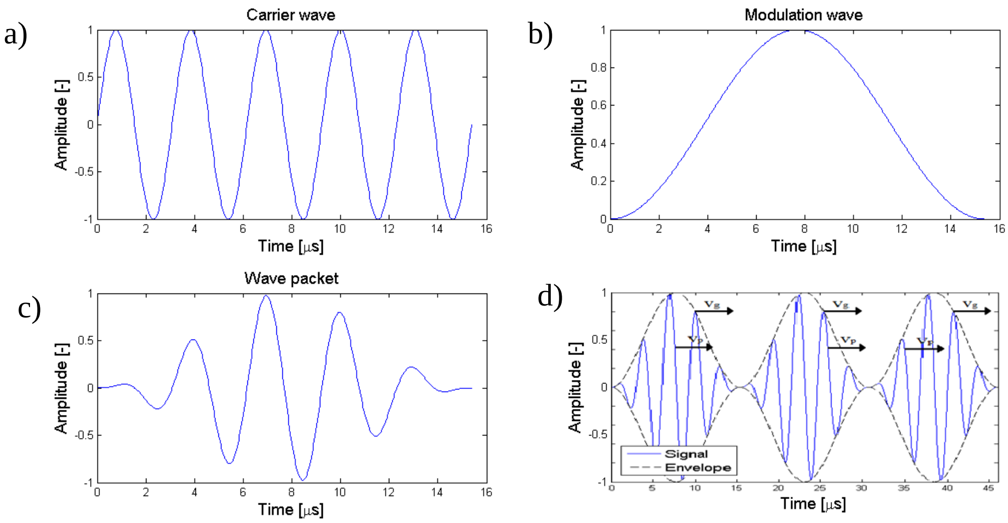

Figure 2.2.3: Wave packet as a superposition of a carrier wave and a modulating wave; a) carrier wave (frequency = 325 kHz); b) modulation wave; c) wave packet (Hanning window); d) 3 wave packets with envelope.

Waves in general have phase and group-velocity, which are especially recognizable in wave packets. The phase velocity is the speed of the individual frequency components, and it can be calculated with:

$$v_p = \frac{\lambda}{T} = \frac{\omega}{k} \tag{2.1}$$

Where λ, ω, T and k are the wavelength, angular frequency, time period and wave number respectively. The group velocity is the speed at which a wave packet (group of frequencies) travels, or in other words, the group velocity is the rate at which the variations in amplitude of the wave propagate through space [16], mathematically it can be calculated as:

$$v_g = \frac{\partial \omega}{\partial k} \tag{2.2}$$

The group velocity is used for measuring the Time Of Flight (TOF), from which the distance travelled or the velocity can be calculate by using the basic formula for isotropic materials:

$$t = \frac{d}{v_g} \tag{2.3}$$

Where t, d and v_g are the TOF, the distance travelled and the propagation velocity (group velocity) respectively. One aspect of propagating waves apart from dispersion is attenuation. Attenuation is the decrease in amplitude of a wave while propagating. During this propagation in a plate the energy is constantly converted back and forward between kinetic and elastic potential energy, a loss in this conversion results in decrease of the amplitude [17]. According to D. Egle in [18, p. 91] there are several sources that can cause attenuation. Firstly, there is the geometric spreading because the wave spreads in all directions of the plate and therefore the energy of the wave is divided over a greater area the further it travels. Secondly, there are energy loss mechanisms such as the conversion of mechanical energy to thermal energy (due to internal friction). Thirdly, there is dispersion that can lead to attenuation and finally there is scatter and diffraction, which can occur at complex boundaries and discontinuities. Fourthly, there can be a loss of the signal at the structure sensor interaction, the sensors itself, in the Data Acquisition system or during post processing of the signal can also lead to loss of signal.

2.3 Acoustic Emission

This Section discusses AE waves, how they originate and their characteristics. AE is defined by the International Organization for Standardization (ISO) as: "*a class of phenomena whereby transient elastic waves are generated by the rapid release of energy from localized sources within a material, or the transient waves so generated*" [19]. Other names for the same phenomena are: stress wave emission and micro seismic activity. AE waves have measurable amplitudes for a frequency range of about 100 kHz to 400 MHz [9] [20].

AE signals are excited during fracture phenomena in the material [20]. There are several sources of AE but 80% of the signals are emitted as a result of events near the crack tip [21] [22]. Sources of AE in metals are due to the initiation and growth of cracks, slip and dislocation movements, melting, twinning, and phase transformations. Gagar *et al.* [23] classified the AE sources associated with cracks into three groups. The first is related to crack extension. The second group is plasticity at the crack tip resulting in emissive particle failure (e.g. non-metallic inclusions) at the origin of the crack tip. Since these particles are less ductile than the surrounding material, they tend to break more easily when the metal is strained, thus resulting in an AE signal [20]. Thirdly, events such as fretting at material and crack surfaces which are related to the rubbing of crack surfaces and slip failure can cause AE signals.

Once damage/fracture occurs, the released energy is translated to elastic wave that propagates through the medium. Because this report focuses on thin plates, it is assumed that the AE waves in our study propagates as a guided wave through the plate. The shape and the frequencies in the moving wave packet do not form an optimized signal as in the case of an active Lamb wave signal, and so the AE signal is more dispersive as compared to a Hanning windowed burst signal. In the AE technique the piezoelectric sensors of SHM system are constantly listening to the structure, once a sensor receives a signal that is above a pre-defined threshold it starts recording. With TDOA methods the location can be calculated, this will be explained in more detail in a later Section. The signal generated by AE is between 50 and 300 kHz as can be seen in the frequency spectrum of Figure 2.3.1. The frequency spectrum may well be different in each signal which is why a broadband sensor should be used. The non-linear sensitivity over the frequency range of most sensors should be accounted for.

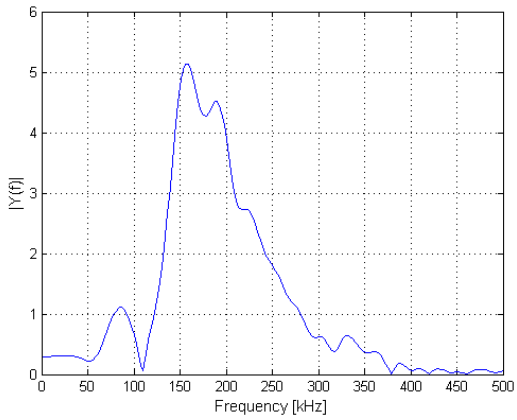

Figure 2.3.1: Frequency spectrum of typical AE source of pencil lead break.[1]

Gagar *et al.* [5] has shown that AE signals can be measured in complex wing-box structures. They showed that there is signal coupling between the spar and the skin, which enables signal transfer from spars to skin. This showed that the AE technique is effective for location analysis in complex structures. As such AE is a promising technique for location analysis. The velocity of wave depends on the frequency and thickness of a wave and plate, but also on temperature and load. AE signal are dynamically excited across a wide range of frequencies and their propagation characteristics at these frequencies will be affected differently due to temperature and load, and these effects will be described in more detail in later parts of this chapter. Understanding how these effects affect the signal propagation is important in order to determine how to localize damage using AE.

Gagar in [9] showed that during a life cycle of a fatigue crack the moment of excitation does not only occur at maximum stress levels as can be seen from Figure 2.3.2 which shows the distribution of AE signals with cyclic stress. This indicates that various sources produce AE signals at different lengths of crack growth, which shows the potential to measure crack length of different sizes with SHM applications.

[1] Data for Power spectrum of typical AE source by pencil lead break tests is obtained from D. Gagar (Cranfield University).

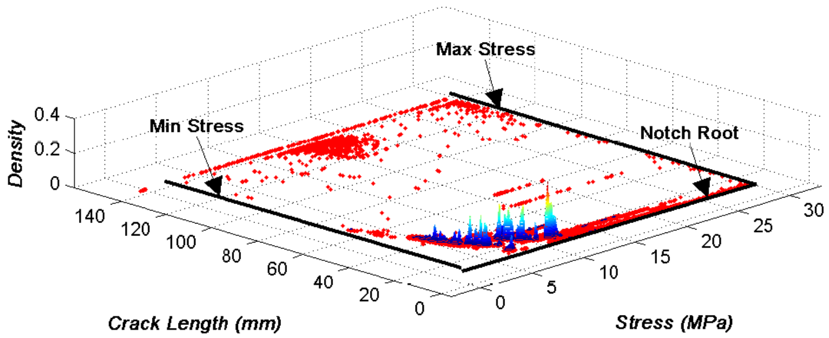

Figure 2.3.2: AE hit density in loading cycles [9].

2.3.1 Parameters of AE burst signal

The AE burst received at the sensor is characterized by a rapid increase to the maximum amplitude and then a near exponential decay to the level of the background noise [24] as illustrated in Figure 2.3.1. This signal can be described according to a set of signal characteristics. Some of the most common characteristics are the following and come from ISO 12716 2001:

<u>Hit & Event:</u> One can speak of a 'hit' when a measured signal exceeds a threshold, where one waveform corresponds to one hit. The waveform must not be confused with individual waves that make up a waveform. An event can be described as the source of a signal; one event can lead to multiple hits because every sensor can receive the hit and its reflections. In experimental setups the signal is measured for an indicated time after the threshold has been reached.

<u>Count:</u> The count is the number of times a signal exceed the threshold, in Figure 2.3.3 nine counts can be observed. Another form of 'count' is the 'count to peak', which is the number of times that a signal exceeds a threshold until the peak of the signal is reached.

<u>Amplitude:</u> Amplitude is the magnitude of the received signal.

<u>Rise time:</u> The rise time is the interval from the triggering time of the AE signal to the time of peak amplitude.

<u>Peak-amplitude:</u> The highest amplitude in the signal envelope.

<u>Energy</u>: Energy is the area under the envelope of the signal.

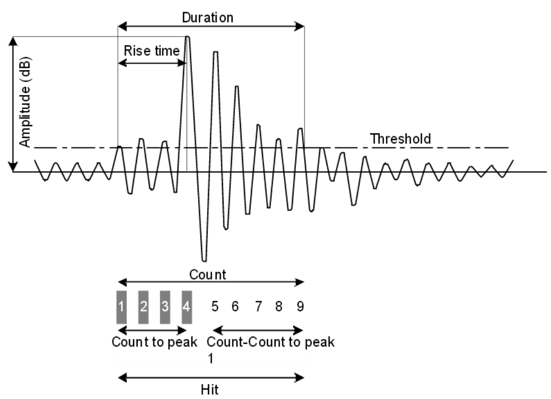

Figure 2.3.3: AE signal parameters [20].

2.4 Transducers

Piezoelectric transducers are often used for acoustic based SHM because they can both receive and send guided Lamb waves and are therefore ideal for active and passive approaches for SHM. A transducer is a general name for any sensor or actuator, but all three names are often used in the literature. Piezoelectric transducers are lightweight and easy to apply and are therefore often used in acoustic based SHM systems [2]. This Section will discuss the working principle of piezoelectric transducers and how it is influenced by temperature and load.

Piezoelectric transducers are built from ceramic materials that have a piezoelectric effect as originally described by Jacques and Pierre Curie in 1880 [25]. The piezoelectric effect relates to the generation of mechanical strains due to electrical charge and conversely the generation of electrical charge due to mechanical strains. The piezoelectric effect is caused by the crystal structure of the material. On a nano-scale a charge distribution is created due to the positive and negative ions in the crystal structure [26]. A medium contains many small domains with different charge orientations. When applying an electric field these domains align in the direction of the electrical field. This results in a polarized material as shown in Figure 2.4.1. When removing the electrical field, the ferromagnetic domains will not move back to their original directions but will move instead to a domain formation that has a minimum state of energy that is close to the direction of the electrical field [26]. This effect results in hysteresis loops in the electrical field versus polarization relation as shown in Figure 2.4.2.

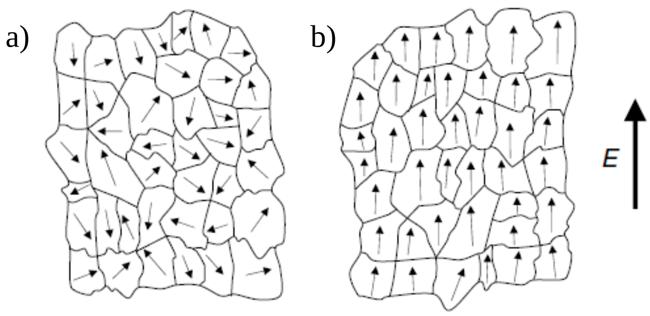

Figure 2.4.1: Polarization hysteresis loop, electrical field vs. polarization [27].

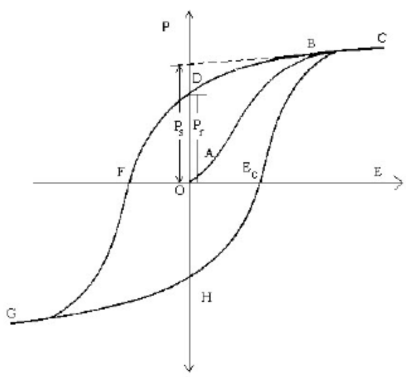

Figure 2.4.2: A typical hysteresis loop, electrical field vs. polarization [27].

When deforming the material once the material has been polarized will lead to a deformation of the crystal structure and therefore a change in charge. The inverse is also true because when applying a charge the crystal structure wants to adapt to the charge and so this results in a material deformation. This piezoelectric effect can be described by a set of strain-charge constitutive relations (Strain-charge form), which are given in tensor form by [27]:

$$S_{ij} = s^{E}_{ijk} T_{kl} + d_{kji} E_k \tag{2.4a}$$
$$D_i = d_{ikl} T_{kl} + \varepsilon^{T}_{ik} E_{kt} \tag{2.4b}$$

Where S, T, E, D, θ are the strain, stress, electric field, electric charge tensors and the temperature variation from ambient temperature respectively. s_{ijk} is the compliance tensor that couples strain per unit stress, d_{kji} and d_{ikl} is the piezoelectric coupling tensor in two forms (one of the forms is the transverse of the first), ε_{ik} is the permittivity matrix, δ_{ij} is the Kronecker delta. This formulation can also be written in three other forms that relate the four field variables in different forms [28].

To measure guided Lamb waves under temperature and stress the constitutive relations of piezoelectric materials can be reduced to a form that relates stress to charge. This means that there is no electrical potential applied. The resulting formula can be found in relation 2.5.

$$\begin{Bmatrix} D_1 \\ D_2 \\ D_3 \end{Bmatrix} = \begin{bmatrix} d_{11} d_{12} d_{13} d_{14} d_{15} d_{16} \\ d_{21} d_{22} d_{23} d_{24} d_{25} d_{26} \\ d_{31} d_{32} d_{33} d_{34} d_{35} d_{36} \end{bmatrix} \begin{Bmatrix} T_1 \\ T_2 \\ T_3 \\ T_4 \\ T_5 \\ T_6 \end{Bmatrix} \tag{2.5}$$

The piezoelectric coupling matrix contains many zeros, which is the result of the direction of polarization. Piezoelectric materials can be polarized in many directions leading to several different possible motions. SHM techniques generally use piezoelectric transducers that are polarized along the thickness direction. This has the advantage that the properties in all the directions in plane will be the same, see Figure 2.4.3 for an example of such a sensor. This means that this type of sensors actuates and measures guided Lamb waves with the same sensitivity in all direction in the plane of the plate.

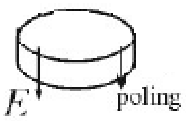

Figure 2.4.3: Through thickness polarized piezoelectric transducer.

This polarization through the thickness leads to the following piezoelectric coupling matrix:

$$d_{ij} = \begin{bmatrix} 0 & 0 & 0 & 0 & d_{15} & 0 \\ 0 & 0 & 0 & d_{24} & 0 & 0 \\ d_{31} & d_{32} & d_{33} & 0 & 0 & 0 \end{bmatrix} \tag{2.5a}$$

It is common for the manufacturer of the piezoelectric ceramics to provide the material constants. It is often the case that due to the crystallographic arrangement of the material, $d_{31} = d_{32}$ and $d_{15} = d_{24}$ [29]. Raghavan *et al.* in [30] investigated the bonding layer of piezoelectric transducers for a temperature range of 20˚C to 150˚C. They concluded that the Epotek 353ND is a suitable bonding agent that does not degrade under thermal variations (the sensor amplitude and the shape remained within the margins of error).

2.5 Wave propagation with EOC

Propagation of waves can be described by velocity profiles of the dispersion curves as has been as has been discussed in Section 2.2 and illustrated in Figure 2.2.2. These curves relate the frequency-thickness of the wave and plate combination to the speed of the wave and thereby describe the way the wave propagates. The theory describing the wave propagation of Lamb waves in isotropic media without EOC was established in 1917 by Horace Lamb [31]. In the active approach a Hanning window can narrow the amount of frequencies to a small band and so the velocity of the wave can be focused. AE signals are dynamically excited across a wide band of frequencies which propagate at different velocities according to the dispersion effect, which makes it difficult to predict which velocity the wave has. The wave velocities are affected with temperature and load. This Section therefore focuses on the previous research conducted on the effect of temperature and load on the dispersion curves. It is divided into three sub- Sections, firstly the effect of temperature is discussed, followed by the effect of loading and finally a combination of both is considered.

2.5.1 Effect of Temperature on Lamb Waves

Thermo-elasticity can be defined as the way in which wave speeds change with temperature. Lee *et al.* [4] experimentally observed that the effect of temperature change on an aluminium plate is so substantial that it outweighs the signal changes observed when damage is introduced and analysed with an active system. They also found no presence of hysteresis effects between heating and cooling steps. One of the first to analytically investigate the effect of temperature on guided waves performed by Sharma *et al.* [32] who developed an analytical theory that included a separate term for the effect of temperature in the thermo-elastic constitution equation, however all the material properties were assumed to be constant.

Konstantinidis *et al.* [33] experimentally investigated an aluminium plate and showed that temperature has an effect on time shift and frequency shift. Time shift can be attributable to three phenomena, firstly, there is the thermal expansion/contraction of the specimen, which changes the propagation distance, density and thickness; secondly, there is the change in Young's modulus that affects the propagation properties of the wave and thirdly there are the temperature induced changes in transducers and their bonds that can results in delay of the signal. The effect of transducers and the bond can be minimized if adhesives and transducers are carefully selected. A frequency shift of a maximum value of 135 Hz was measured over a temperature range of 10˚C. This frequency shift does however have very little effect (-55dB) on the change in propagation velocities and is therefore not so significant when compared to the effect of changes in Young's modulus (-26 dB for a 10 ˚C temperature change). In Figure 2.5.1 the effect on the signal of four effects is shown for a 10 ˚C temperature difference. It shows that the effect of change in thickness and propagation distance on frequency shift is very small. The Figure also shows that the Young's modulus has the most significant effect.

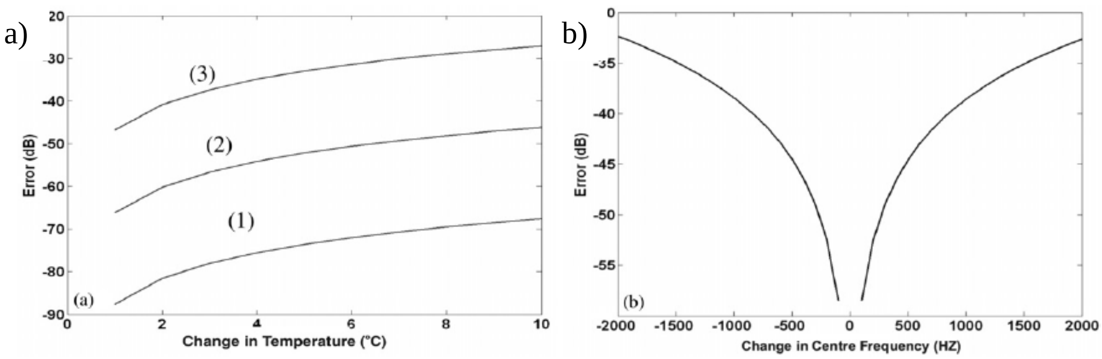

Figure 2.5.1: a) Error with temperature variation (T_0 is 25 ˚C) due to; 1) change in plate thickness; 2) change in propagation distance; and 3) change in Young's modulus. b) Error caused by frequency shift [33].

Raghaven *et al.* [30] investigated the effect of considerable temperature variations (20˚C - 150˚C) on Lamb wave propagation for the use of GW-SHM in spacecrafts. They reason that Young's modulus, piezoelectric properties, thermal expansion; damping and pyroelectric effects are influenced by temperature, however they only investigated the first three effects. Thermal expansion can be calculated when the CTE is known and very small. The other two effects are represented in Figure 2.5.2 where the piezoelectric properties change by a maximum of 7% over the temperature range whereas the elastic properties change significantly over the given temperature range. In the same article [30] it was concluded that the amplitude drops significantly with temperature but there is negligible shape distortion. Damage detection of a half-plate thickness indentation with temperature compensation was very difficult above 80˚C but a through thickness hole was detectable at all temperatures.

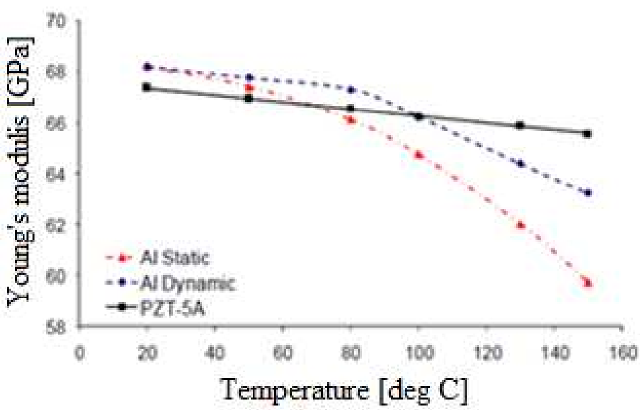

Figure 2.5.2: Young's modulus of aluminium alloy 7075 (static) with temperature, alloy 5052 (dynamic) [30].

Gandhi *et al.* [34] investigated the effect of temperature on the dispersion curves by using a perturbation theory, which amounts to an approximation of reality. Dodson [35] states that until 2012 the majority of the analysis of thermal effects on dispersion curves was numerically and empirically based. He therefore investigated how dispersion curves analytically change with temperature over a large range of frequencies. In a later article Dodson *et al.* [36] extended the dispersion curve theory of Horace Lamb by including the effect of temperature in the equation of motion and also acknowledging the effect of changing young's modulus with temperature. They were able to use this approach because a change in temperature will expand / contract the substrate in all directions, the properties remain the same in all those direction and therefore isotropy can still be assumed. They developed the change in velocity for a range of temperatures as can be seen in Figure 2.5.3. The Figure shows that two temperature invariant points exist for a frequency of 2.642 and 3.251 MHZ-mm. In theory these points have a constant group velocity for varying temperature conditions. These invariant points lay in the frequency-thickness area where higher modes occur therefore these two points are not really applicable when limiting the frequency range to natural modes.

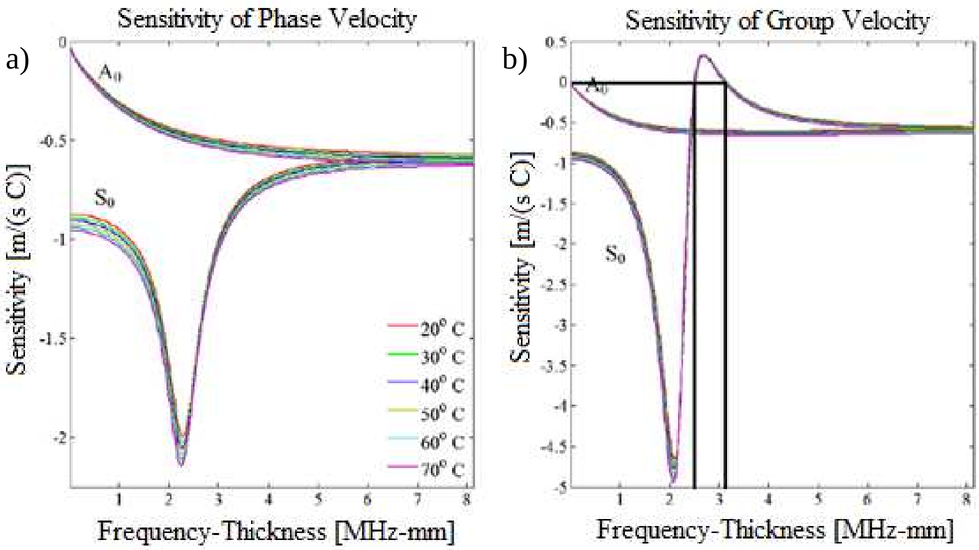

Figure 2.5.3: Normalized Sensitivity of a) phase velocity b) group velocity [36].

2.5.2 Effect of Load on Lamb Waves

Acousto-elasticity can be defined as the change in elastic wave speeds with stress [37]. This Section discusses previous research into the acousto-elastic effect on the dispersion curves in plates.

Gandhi *et al.* [38] were one of the first who investigated the effect of uniaxial stress on Lamb wave propagation. They numerically simulated and experimentally verified how the effect of stress on plates affects the propagation characteristics of the received signal. They concluded two effects, which are changes in strain and the acousto-elastic effect. The strain affects the dimensions, which in turn influences the transducer distance and the acousto-elastic effect. The strain makes an isotropic plate anisotropic by applying load and so the propagation of waves becomes directionally dependent. Therefore to generate a theory describing these effects the Christoffel equation for anisotropic media is used, which is mathematically described as:

$$(\rho\omega^2\delta_{im} - C_{iklm}k_k k_l)u_m = 0 \tag{2.6}$$

Where ρ, ω, k_k, k_l are the density, angular frequency, wavenumber in k and wavenumber in l respectively. u_m is the displacement in m, C_{iklm} is the elasticity tensor and δ_{im} is the Kronecker delta. The variation of phase velocity is very close to linear whereas the angular dependency closely fits a sin(2φ) curve. The absolute value of these results can hardly be generalised because it depends on the frequency. In a follow up article by Michaels *et al.* [39] the effect of stress compared to damage was experimentally demonstrated and they concluded that signal changes from considerable loads are significantly larger than those from damage (in this case with a mass). They therefore advocate that damage detection, which rely upon signal change coefficients, are likely to fail in the presence of loading variations.

Gandhi *et al.* [37] also studied the effect of bi-axially stressed plates. The already developed theory to predict Lamb wave propagation was again used for initially isotropic plates in biaxial applied stress. They merely verified the theory by means of a uni-axial test, but stated that the directional effects of both uni-axial loads can be superimposed on each other. Once again as in their previous research, they concluded that phase velocity changes linearly with increasing stress and that it has a sinusoidal dependence with the angle between sensor path and loading direction for a single frequency as can be seen in Figure 2.5.4. The angle dependent profile also results in a loading invariant point around 27 degrees for the S_0 mode under uni-axial loading for an aluminium 6061-T6 plate. They also investigated these effects under changing frequencies, which is shown for the A_0 mode and S_0 mode in Figures 2.5.5a and 2.5.5b respectively. It can be seen that for the S_0 mode the angle under which the loading invariant point exist decreases when the frequency-thickness increases. However this seems to stabilize at 45 degrees when the frequency-thickness goes above 4 MHz-mm. For the A_0 mode the has an isotropic change in phase velocities for a frequency-thickness product of 0.187 [MHz-mm], which means that there is still a change in wave velocity with temperature however there is no angle dependent change in wave velocity. It is important to note that the group velocities were not calculated by these authors.

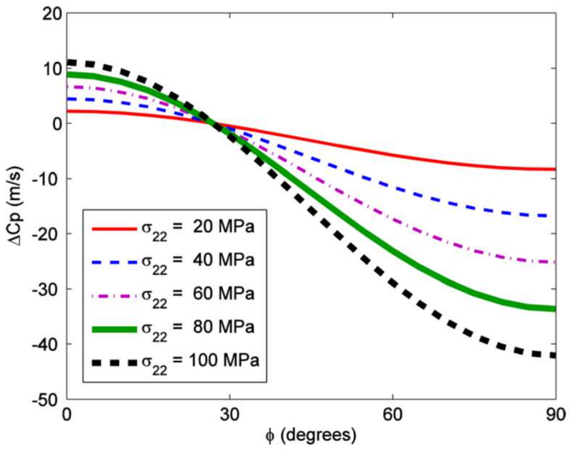

Figure 2.5.4: Change in phase velocity versus propagation angle for the S_0 mode in aluminium (thickness of 6.35 mm) at 250 kHz and for different uni-axial loads applied along the y-axis (90˚) [37].

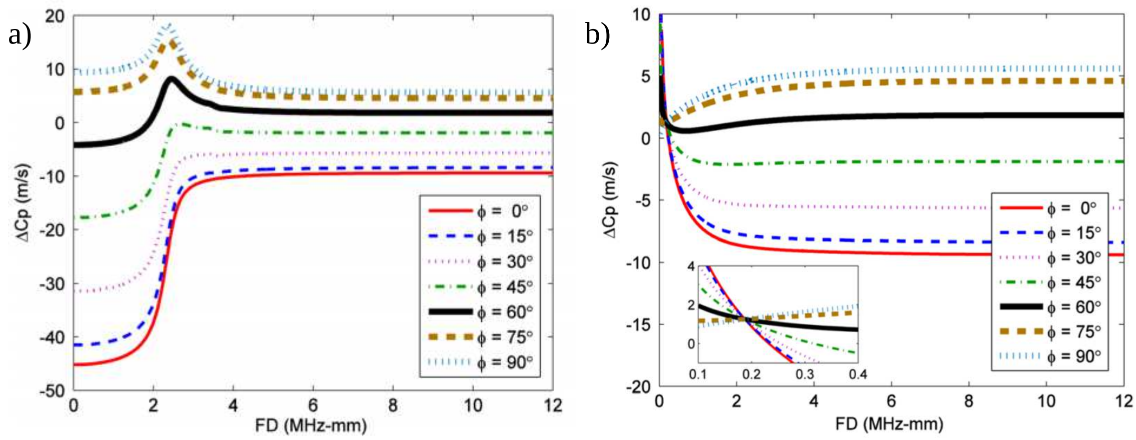

Figure 2.5.5: Change in phase velocity versus frequency in aluminium under 100 MPa loading at various angles; a) S_0 mode; b) A_0 mode [37] [40]. [39]

The theory seems to follow the same trend as the experimental results that Gandhi *et al.* [37] produced, however they only experimentally focused on signal change coefficients and change in phase velocities. They reason that differences between theory and experiments are related to difficulties in accurately obtaining third order elastic constants. Lee *et al.* [41] compared experimentally the anisotropic effect of applied loads on the direct arrivals of various Lamb wave modes for the phase velocity and compared those to both the theory and to the isotropic effect of temperature. They conclude that ''*results are in good agreement with theory and time shifts caused by applied loads are of the same order as those caused by temperature changes and cannot be ignored in the context of structural health monitoring*'' Lee *et al.* [41, p. 181].

Song *et al.* [42] investigated the effect of the pre-stressed plate with piezoelectric transducer interaction to GW propagation. They are the first to investigate both tensile and compressive stresses. They observe increasing phase velocities with increasing tensile stress and vice versa for the compressive case for the A_0 mode. However, they only look at the change in phase velocity for the direction in line with the loading and therefore they don't observe the anisotropic effect described by Gandhi *et al.* in [37].

To compensate for the anisotropic effect of loading Shi *et al.* [43] developed an inverse method based on the theoretical work of Gandhi *et al.* [37]. The inverse method estimates applied loads from observed changes in phase velocity for propagation paths at multiple angles. The method cannot meet the accuracy of strain gauges. They reasoned the main advantage of the inverse method is the lack of additional sensors. This method was not applicable when multiple EOC occur simultaneously because the observed changes in phase velocity were the result of all EOC and not only load.

2.5.3 Effects of both Temperature and Loads on Lamb Waves

The literature addressing thermo-elastic effects discussed in the previous Section shows that homogenous temperature variations influence: expansion/contraction of the substrate, piezoelectric properties and so the dispersions curves. The literature addressing acoustic-elastic effects shows that pre-stresses affect the deformation of the substrate, piezoelectric properties, the dispersions curves and it additionally makes the substrate anisotropic which means that properties of the wave depend on the direction of propagation.

Until now this Section has separately discussed the research that has been carried out on both temperature and load effects on dispersion curves. To the writers knowledge so far there has been only one researcher, Dodson [35], which focussed on combining both effects into one theory. Dodson starts with the theory developed by Gandhi *et al.* [38] that describe the dispersion curves with pre-stresses, he then uses the Christoffel equations for anisotropic media. The analytical work, which has been developed for isotropic media, is rewritten for anisotropic media. Then these two are combined into a single theory, which results in a new thermo-acoustic-elastic tensor, which describes the changes in acoustic-elastic behaviour with temperature.

2.6 Compensation methods for effect of Temperature inactive approach

The literature describes that the major EOC is temperature, and therefore researchers have developed several compensation techniques, which will be discussed in this section. These methods are however only applicable to the active SHM approach.

<u>Baseline subtraction:</u> Interpretation of raw signals might be very complicated because of the multiple reflections found in complex aerospace structures. To avoid this interpretation of the raw signal baseline subtraction techniques are commonly used. One major drawback is that significant signal changes be created due to EOC such as temperature and loads. Lowe et al. [44] state that the ideal amplitude level of the residual signal after baseline subtraction should be close to -40 dB relative to the amplitude of the first arrival because reflection from defects are likely to produce levels of -30 dB or lower.

<u>Optimal baseline subtraction (OBS):</u> This approach uses multiple baselines for every EOC to reduce the error with that specific EOC. A problem with OBS is that multiple EOC require a baseline for every combination of the EOC. This will increase the set of baselines increasingly faster with every factor that needs be taken into account. Konstantinidis et al. [33] state that memory is becoming very cheap these days and is therefore not the limiting factor for this approach.

<u>Signal Stretch:</u> Signal stretch is an approach that dilates the signal so that it matches the reference baseline signal. Uniform temperature change results in a change in wave velocity and a expansion/contraction of the structure itself. The signal stretch strategy compensates for these effects by applying an inverse dilation to the time axis of the current signal and then subtracts the baseline signal. When dilating the time axis the individual wave packets are also dilated which results in a frequency shift, however this frequency shift does not occur in reality [45]. The frequency shift can be rather significant for large temperature variations but

compensation is not necessary when OBS is applied. Therefore the time-stretch model is not generally true [46]. Croxford et al. [14] assume that temperature causes a shift in time of arrival of the signal. Starting with formula 2.3 for the TOF, which is $t = d/v_{gr}$ and differentiating it with respect to temperature leads to:

$$\frac{\partial t}{\partial \theta} = \frac{1}{v_g}\frac{\partial d}{\partial \theta} - \frac{d}{v_g^2}\frac{\partial v_g}{\partial \theta} \qquad (2.7)$$

The t, θ, d and v_g are the time, temperature, length of the plate and the group velocity. The relation between distance and temperature is $\frac{\partial d}{\partial \theta} = \alpha d$ where α is the Coefficient of Thermal Expansion (CTE). They assume that the relation between wave velocity (due to changes in stiffness) and temperature can be written as $\frac{\partial v_g}{\partial T} = \beta$. This together result in:

$$\delta t = \frac{d}{v_g}\left(\alpha - \frac{\beta}{v_g}\right)\delta T \qquad (2.8)$$

With this method they calculate errors between the baseline and thermal variations in the presence of damage.

Several different signal stretch approaches have been developed: 1) Optimal Signal Stretch (OSS): this approach is an optimization strategy for finding a scale factor α that minimizes the squared error between a baseline and a measured data. 2) Local Peak Coherence (LPC): this approach is an estimation technique based on approximating a stretching operation as a series of time-dependent delay operations. 3): Scale-Invariant Correlation Coefficient (SICC): This is an approach to optimize a scale factor, like OSS. This last approach is faster than the other two.

Wilcox et al. [47] conclude that when signal stretch is used a subsequent time shift may also improve the performance (especially convenient when sensor properties change with EOC. Croxford et al. [48] repeat the same research as [47] and conclude that a combination of both OBS and BSS is a practical solution to temperature compensation. However these approaches discussed above are still applied to only the effect of temperature. Other EOC introduce more effects that need to be compensated for, making it difficult to find one method that can compensate for all effects. Therefore a current problem for the active approach is to find new methods that can compensate for the effects of multiple EOC so to be able to find the signal changes due to damage.

2.7 Damage localization

Section 2.5 discussed the effect of temperature and load on the wave velocities in the dispersion curves. The change in wave velocities will impact the location algorithms and so the accuracy of the calculated location. This Section will discuss damage localization approaches for both active and passive approaches. Approaches differ because for the active approach the location is known where the signal is actuated, while for the AE approach the location is unknown. This Section is divided into two sub sections; first localization methods used in the active approach are discussed to understand how temperature and load affect localizing the damage. Then secondly damage localization for the AE approach is discussed.

2.7.1 Damage localization for the active GW approach

Damage localization with the active approach is based on extracting time of arrival. The actuated signal starts the recoding and by comparing the time difference between the actuated and signal and received signal the TOA can be obtained, which can then be used to perform the localization. Mostly one point on the waveform is used for calculation of the travel time of the wave (more often called Time Of Arrival TOA). This point is often the peak value because the Hanning window is focussed at one frequency and the peak value in the waveform is a stable point.

Damage localization for isotropic media which are not affected by temperature variation or loading can be calculated with an ellipse method suggested by Konstantinidis *et al.* [33]. A subtracted time signal f_j can be used through the following formula to generate intensity I_j of damage at every location:

$$I_j(x, y) = f_j\left(t = \frac{\sqrt{(x_t-x)^2+(y_t-y)^2}+\sqrt{(x_r-x)^2+(y_r-y)^2}}{v_g}\right) \qquad (2.9)$$

This will lead to an ellipse of the maximum intensity where the foci are the j^{th} transducer pair. Where (x, y) is the coordinate of the image point, $f_j(t)$ = the subtracted time series, (x_t, y_t) are the coordinates of the actuator and (x_r, y_r) are the coordinates of the receiver and v_g is the group velocity of the wave. In order to locate defects, the crossings from the ellipse from each transducer pair indicate potential locations of damage. This can be done by summing up the intensity of the ellipses of all the transducer pairs:

$$I = \sum_{j=1}^{n} I_j \qquad (2.10)$$

Where n is the amount of transducer pairs available in the array of transducers. Damage localization in materials that are anisotropic due to pre-stresses (or in composite materials) result in an angle dependent velocity profile, which makes it difficult to select one velocity for the location algorithm. For anisotropic materials the ellipsoid becomes angle dependent and so the ellipse shape transforms into an irregular shape dependent on velocity profile and the frequency-thickness of the material. Moll *et al.* [49] extended the ellipse method for this anisotropic behaviour. They recognise that the path from the actuator to the damage and the path from the damage to sensor are susceptible to different propagation properties as can be seen in Figure 2.7.1a. The group velocity of both paths depends on the angle, frequency-thickness and EOC. Therefore the total TOA is equal to the sum of travel time from actuator to damage and the travel time of damage to sensor, mathematically this is:

$$\mathrm{TOA} = \mathrm{TOA}_1 + \mathrm{TOA}_2 \tag{2.11}$$

By filling the geometric relations of formula 2.12 and 2.13 into formula 2.11 result in formula 2.14 which can give a solution for the upper triangle of Figure 2.7.1a:

$$\frac{\sin(\theta_2)}{TOF_1 c_{gr}(fd,\theta_1+\tau,EOC)} = \frac{\sin(\theta_3)}{L} \tag{2.12}$$

$$\frac{\sin(\theta_1)}{TOF_1 c_{gr}(fd,-\theta_2+\tau,EOC)} = \frac{\sin(\theta_3)}{L} \tag{2.13}$$

$$TOF \sin(\pi - \theta_1 - \theta_2) = \frac{L\sin(\theta_2)}{c_{gr}(fd,\theta_1+\tau,EOC)} + \frac{L sin(\theta_1)}{c_{gr}(fd,\pi-\theta_2-\tau,EOC)} \tag{2.14}$$

This relation contains two variables and cannot be solved analytically; hence it is transformed to an error function, which has to be numerically solved for zero. The new relations formula 2.12 to 2.14 result in non-elliptical curves as a result of the anisotropic wave propagation in a plate, this can be seen in Figure 2.7.1b.

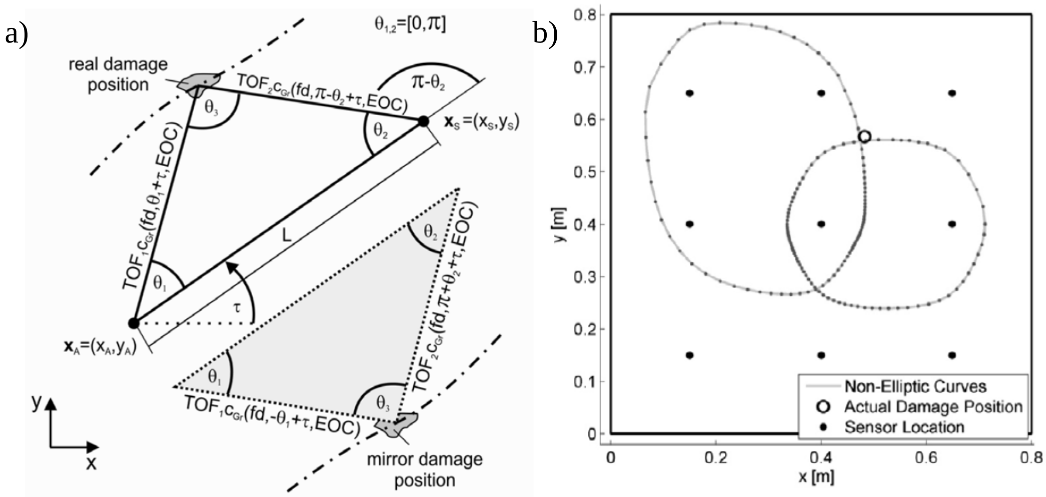

Figure 2.7.1: a) Schematic for damage localization in anisotropic plate-like structures [49]; b) Non-elliptical curves as a result of the anisotropic wave propagation in the plate [49].

This approach requires a priori knowledge how wave velocities change with the angle, demanding better knowledge of the effect of temperature and load on the group velocity. This method can improve localization however it is computational expensive and the a priori knowledge of the changing wave velocities will often be unknown because the strength of the EOC can vary freely, therefore this is not ideal for real time monitoring.

2.7.2 Damage localization for the Acoustic Emission approach

The passive approach (such as AE) is based on the signal crossing a predefined threshold to start the recording after which it is recorded for a specified amount of time. This means that the AE signal can actuate at a certain moment in time, after which it travels and reaches the sensors, which will start the recording once the threshold is crossed. This approach will result in Time Difference Of Arrival (TDOA) of the first hit signal with respect to all the other sensors, from which a location can be calculated. When the wave has been generated damage localization can be performed in two steps. The first is to establish the arrival times and the second is to locate the damage from these arrival times [50], which requires estimates of wave speed [9].

To obtain TDOA a reference point in the waveform should be used to calculate the TDOA. The reference point in the waveform taken for this is usually the first threshold crossing, but also the peak amplitude can be used. Both have their advantages and disadvantages. When measuring an AE wave the first threshold crossing can be influenced by attenuation of the signal, which can result in longer TDOA than in reality. On the other hand, peak amplitude changes with dispersion and attenuation and is likely to be less stable than using the first threshold crossing. This is because the peak amplitude can shift more due to an AE wave packet containing many different frequencies that make up the wave and each frequency has its own speed [50]. Once these TDOA have been obtained localization algorithms can calculate locations of the source. Current approaches are limited in use because they all assume a constant group velocity. In a 1-D case, the TDOA can be calculated with formula 2.15.

$$d_1 = \frac{1}{2}(\mathrm{D}-\Delta \mathrm{t}\cdot v_g) \tag{2.15}$$

Where 'v_g' is the group velocity of the wave, 'D' is the distance between the transducer pair, 'd_1' is the distance from the source to the closest transducer and 'Δt' is the TDOA measured at both transducers, this can be seen in Figure 2.6.2.

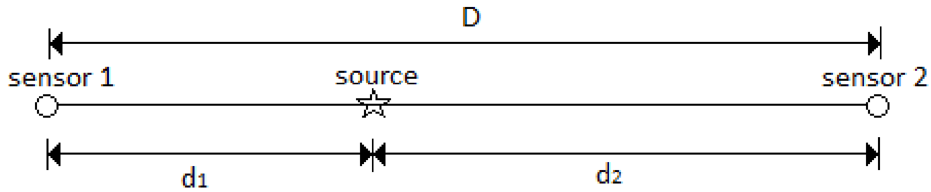

Figure 2.7.2: Schematic for one dimension localization using TDOA.

The relations for 2D localizing damage in isotropic materials are given by formula 2.16-2.18. The distance between two points in a 2-D plane is expressed by formula 2.16 and can be extended to 3-D. The TDOA method in the AE approach complicates localization.

$$d_i{}^2 = (x_i - x_L)^2 + (y_i - y_L)^2 \tag{2.16}$$

Each TDOA is a difference in distance to the transducer relative to the distance to the first hit transducer, which mathematically can be expressed as:

$$\Delta t_i = t_i - t_1 = \frac{d_i - d_1}{v_g} \qquad \text{(With } 2 \leq i \leq \text{\# of transducers)} \tag{2.17}$$

When combining formula 2.16 and 2.17 it results in:

$$\Delta t_i = \frac{\left[\sqrt{(x_i - x_L)^2 + (y_i - y_L)^2} - \sqrt{(x_1 - x_L)^2 + (y_1 - y_L)^2}\right]}{v_g} \tag{2.18}$$

Where 'x_L' and 'y_L' is the unknown location of the source, 'x_i' and 'y_i' is the location of the sensors, 'd_i' is the distance from the source to sensor 'i', 't_1' is the travel time from the source to the sensor that received the first signal (in other words the closest sensor) and 'Δt_i' is the travel time to the remaining sensors. The difference between $t_i - t_1$is the TDOA. Equation 2.18 has two unknowns and therefore three transducers are minimally required to solve it, but four and five transducers can be used to obtain less ambiguous results [51]. When more than three sensors are added then an over determined system of relations is obtained and a regression analysis such as least-squares method can help to solve it.

Ernst and Dual [52] introduced a new approach to locate AE sources in 2-D with one sensor through a numerical approach that uses the dispersive nature of guided wave in a time reversal simulation approach. This method can be computational expensive and therefore not ideal for real time monitoring. They state that because this approach uses the entire waveform it has the potential to be more accurate than TOA/TDOA methods because of an uncertainty principle making it difficult to exactly localize a signal in both frequency and time-domain.

2.8 Analysis of Literature study

EOC such as temperature and load can affect the guided waves in SHM systems. Signal changes due to these EOC can be more significant than the signal changes due to a defect for active approaches, which make it difficult to detect signal changed due to damage. Several attempts have been taken to develop methods to compensate for temperature effects. However, methods are still limited in application because they require large amounts of baselines. Furthermore there have not been attempts to compensate for combined effects from temperature and load. This is affecting implementation of active SHM approach for real time monitoring in operational environment. AE approaches do not require compensation methods for distinguishing signal changes due to damage because the signal is actuated by the damage. However, for localization effects of EOC should be understood.

There have been several studies to identify the individual effects of temperature and load. Temperature influences many properties but most significantly impacts the stiffness, density and thermal expansion coefficients. The stiffness and density changes directly influence the lamb wave relations resulting in changes in velocity with temperature. Other studies investigated the effect of load on Lamb wave propagation. Load affects the local stress distribution and the distance between the sensors. The stress distribution makes a material anisotropic and wave velocities become directional dependent and change linearly with load, however these results have not experimentally been verified for the group velocity. Furthermore, these effects of temperature and load have been investigated for the active SHM approach. However, for the passive approach such as AE, the effect of EOC can be very different because there is no actuated signal that needs to be distinguished for signal detection. The combination of these two techniques in a hybrid (active-passive) SHM system can potentially provide reliable results.

To develop a hybrid system, first the effects of EOC on AE system should be understood to be able to understand how to combine both systems in one. Therefore understanding the impact of EOC on the acoustic emission approach for SHM is important to be able to assess this technology for real time monitoring in an operational service environment.

Chapter 3: Analytical description of effect of Temperature on Lamb waves

The literature study showed that temperature is seen as one of the largest effects on propagating waves. Furthermore, the theory developed by Dodson & Inman is not experimentally verified. Therefore this chapter describes the analytical modelling of the effect of temperature on the dispersion curves for aluminium 2024-T3. Section 3.1 starts with the analytical relations from Dodson *et al.* [36], which describes the dispersion curves with temperature and how these curves have been solved iteratively. Section 3.2 discusses the changes in material properties with temperature. Section 3.3 gives the results of the changes in wave speed with temperature. Then this chapter ends with Section 3.4 which will focus in more detail on the temperature invariant points that were described by Dodson and Inman [36].

3.1 Isotropic thermo-elastic Lamb wave relations

The derivation of the isotropic thermo-elastic lamb wave relations are based on the equation of motion as a function of temperature in combination with the continuity stress/strain equation. The mathematical derivations of these equations are beyond the scope of this research study. However, the presented formulation in this Section can be used as the basis for a dispersion curve equation as a function of temperature.

Dodson and Inman [36] have developed the Lamb wave relations for free infinite plates with homogenous temperature changes; stated as $(\theta(\bar{x},t) = \theta(t))$. Because the plate thickness is very small compared to the other two dimensions plane strain is assumed. The starting point for these relations is the equation of motion, which mathematical can be expressed as:

$$\big(\lambda(\theta) + \mu(\theta)\big)\nabla\nabla\bar{u}(\bar{x},t) + \mu(\theta)\nabla^2\bar{u}(\bar{x},t) = \rho(\theta)\ddot{\bar{u}}(\bar{x},t) \tag{3.1}$$

Here θ stands for the absolute temperature [˚K], and $\rho(\theta)$, $\lambda(\theta)$, $\mu(\theta)$ are the temperature dependent mass density, and the two Lame's elastic moduli respectively. Furthermore the variable $\bar{u}(\bar{x},t)$ symbolizes the displacement vector. Using a Helmholtz decomposition for the displacement vector two differential equations are obtained for the translational and rotational parts of the equations. The solutions of these equations can be inserted into the constitutive relation that relates strain to stress which takes the effect of temperature change into account, this can be written as in formula 3.2. This formula is obtained from Ignaczak *et al.* [53].

$$\sigma_{ij}(\bar{x},t) = \lambda(\theta)S_{kk}(\bar{x},t)\delta_{ij} + 2\mu S_{ij}(\bar{x},t) - (3\lambda(\theta) + 2\mu(\theta))\alpha_0\delta_{ij}\theta(\bar{x},t) \tag{3.2}$$

In this formula, the symbols $S_{ij}(\bar{x},t)$, $\sigma_{ij}(\bar{x},t)$, α_0, δ_{ij} stand for the strain, stress, isothermal thermal expansion coefficient and the Cronecker delta respectively. The linear strain displacement relations can be written as:

$$S_{ij}(\bar{x},t) = \frac{1}{2}\Big(\bar{u}_{i,j}(\bar{x},t) + \bar{u}_{j,i}(\bar{x},t)\Big) \tag{3.3}$$

Applying the boundary conditions of the top and bottom surfaces of the plate (where the stress is zero) to the longitudinal- and shear-stress relations lead to two equations that should be solved to zero. These two equations can be rewritten into the Lamb wave equations, mathematically expressed as:

$$\frac{(\kappa^2+s^2)^2}{4k^2sq} = \left[\frac{\tanh(qh)}{\tanh\,(sh)}\right]^{\pm 1} \tag{3.4}$$

Where h is half the thickness, q and s will be discussed later this Section. For further information regarding the derivation of formula 3.4, the reader is advised to read the article of Dodson *et al.* [36]. Aforementioned relation 3.4 is very similar to Lamb wave relations developed by Horace Lamb, the difference being that the tangent hyperbolic is a tangent function in the relations developed by Horace Lamb. The +1 sign is for the symmetric modes and the -1 for the anti-symmetric modes. The relation can also be written in the following form:

$$(\kappa^2 + s^2)^2 \cdot \tanh(sh) - 4k^2sq \cdot \tanh(qh) = 0 \tag{3.5a}$$
$$(\kappa^2 + s^2)^2 \cdot \tanh(qh) - 4k^2sq \cdot \tanh(sh) = 0 \tag{3.5b}$$

Where equation 3.5a stand for the symmetric modes and equation 3.5b for the anti-symmetric modes. Both equations need to be solved for zero to find solutions to the phase velocities for a range of frequency thickness products. Dodson and Inman reasoned that changing material properties with temperature like elastic modulus (E), poison ratio (v), thickness, and density have major impact on the Lamb wave relations. The values used for these constants will be discussed in more detail in Section 3.2. Beside the material properties the height (h) and density (ρ) will also change with temperature, expressed mathematically as:

$$h(\theta) = h_o(1 + \alpha\theta) \tag{3.6}$$

$$\rho(\theta) = \frac{\rho_0}{(1+\alpha\theta)^3} \tag{3.7}$$

Furthermore the variables κ (wave number), and the terms s and q, which are introduced for convenience in formula 3.4, can be written as:

$$\kappa = \frac{w}{v_p},\ \kappa_L = \frac{\omega}{v_L(\theta)},\ \kappa_T = \frac{\omega}{v_T(\theta)} \quad \text{as in formula 2.1.}$$
$$q = \sqrt{\kappa^2 - \kappa_L^2} = \omega\sqrt{\frac{1}{v_p^2} - \frac{1}{v_L^2(\theta)}} \tag{3.8}$$
$$s = \sqrt{\kappa^2 - \kappa_T^2} = \omega\sqrt{\frac{1}{v_p^2} - \frac{1}{v_T^2(\theta)}} \tag{3.9}$$

Where κ is the wave number for frequency of the wave, κ_L and κ_T are the wave number of the longitudinal and transverse wave velocities with v_L and v_T being the longitudinal and transverse velocity.

These two velocities are two terms that have the units of velocity and come back often in Lamb wave theory, they can be calculated by:

$$v_L(\theta) = \sqrt{\frac{\lambda(\theta)+2\mu(\theta)}{\rho(\theta)}}, \quad v_T(\theta) = \sqrt{\frac{\mu(\theta)}{\rho(\theta)}} \tag{3.10}$$

The Lamé constants as function of temperature $\lambda(\theta)$ and $\mu(\theta)$, which are also used in the equation of motion and longitudinal and transverse wave number, can be written as:

$$\lambda(\theta) = \frac{E(\theta)\cdot\nu(\theta)}{(1+\nu(\theta))(1-2\nu(\theta)} \tag{3.11}$$

$$\mu(\theta) = \frac{E(\theta)}{2(1+\nu(\theta)} \tag{3.12}$$

Where E(θ), $\nu(\theta)$ and $\rho(\theta)$are the temperature dependent stiffness, poison ratio and density. Equation 3.4 is the final relation given by Dodson & Inman, but before this can be solved it needs to be realized that the equations for 'q' and 's' become imaginary when the phase velocity is smaller than the v_T or v_L. In those cases both 'q' and 's' can be written as:

$$q = \omega\sqrt{\frac{1}{v_p^2} - \frac{1}{v_L^2(\theta)}} = i\hat{q} = i\omega\sqrt{\frac{1}{v_L^2(\theta)} - \frac{1}{v_p^2}} \tag{3.13a}$$

$$s = \omega\sqrt{\frac{1}{v_p^2} - \frac{1}{v_T^2(\theta)}} = i\hat{s} = i\omega\sqrt{\frac{1}{v_T^2(\theta)} - \frac{1}{v_p^2}} \tag{3.13b}$$

Where 'i' is the imaginary number $\sqrt{-1}$. v_T will be always smaller as v_L which is clear when comparing formula 3.10 where $\lambda(\theta) + 2\mu(\theta) > \mu(\theta)$. However, auxetic materials, which have negative Poisson's ratio, can be the exception to this rule, but this is outside the scope of this thesis. Both v_T and v_L are defined by the material properties making them constant for each material. We want to solve for real solutions and therefore this means the Lamb wave relations of relation 3.5a and b need to be solved for three different regions with the constants of 'q' and 's' as summarized in table 3.1.

Table 3.1: Variables 'q' and 's from formula 3.13a-b for different regions of the phase velocity.

	Region 1	Region 2	Region 3
	$v_p < v_T < v_L$	$v_T < v_p < v_L$	$v_T < v_L < v_P$
q	$q = \omega\sqrt{\frac{1}{v_p^2} - \frac{1}{v_L^2(\theta)}}$	$q = \omega\sqrt{\frac{1}{v_p^2} - \frac{1}{v_L^2(\theta)}}$	$q = i\hat{q} = i\omega\sqrt{\frac{1}{v_L^2(\theta)} - \frac{1}{v_p^2}}$
s	$s = \omega\sqrt{\frac{1}{v_p^2} - \frac{1}{v_T^2(\theta)}}$	$s = i\hat{s} = i\omega\sqrt{\frac{1}{v_T^2(\theta)} - \frac{1}{v_p^2}}$	$s = i\hat{s} = i\omega\sqrt{\frac{1}{v_T^2(\theta)} - \frac{1}{v_p^2}}$

When solving relation 3.4 with the correct relations from Table 3.1 to zero then one can find for every frequency-thickness product the phase velocity at which the wave travels. This thesis focuses on the natural A_0 and S_0 modes. The A_0 mode only has solution in region 1, and the S_0 mode only has solutions in region 2. Therefore only these regions need to be calculated. When combining the correct functions of table 3.1 in relations 3.5a and 3.5b, and also foreseeing that the lamb wave relation will be solved separately for every temperature then the v_T and v_L will become constants, then the following relations are obtained:

Anti-symmetric mode in region 1:

$$\left(2-\left(\frac{v_p}{v_L}\right)^2\right)\tanh\left(\frac{2\pi\cdot fh}{v_p}\sqrt{\left(1-\left(\frac{v_p}{v_L}\right)^2\right)}\right)-4\cdot\sqrt{\left(1-\left(\frac{v_p}{v_L}\right)^2\right)}\cdot \sqrt{\left(1-\left(\frac{v_p}{v_T}\right)^2\right)}\cdot tanh\left(\frac{2\pi\cdot fh}{v_p}\sqrt{\left(1-\left(\frac{v_p}{v_T}\right)^2\right)}\right)=0 \qquad (3.14)$$

Symmetric mode, region 2:

$$\left(2-\left(\frac{v_p}{v_L}\right)^2\right)\tan\left(\frac{2\pi\cdot fh}{v_p}\sqrt{\left(\left(\frac{v_p}{v_T}\right)^2-1\right)}\right)-4\sqrt{\left(1-\left(\frac{v_p}{v_L}\right)^2\right)}\cdot \sqrt{\left(\left(\frac{v_p}{v_T}\right)^2-1\right)}\cdot tanh\left(\frac{2\pi\cdot fh}{v_p}\sqrt{\left(1-\left(\frac{v_p}{v_T}\right)^2\right)}\right)=0 \qquad (3.15)$$

Where fh is the frequency-thickness of the plate and wave (where thickness of the plate t=2h). Because v_p is inside the trigonometric terms it cannot be solved in a closed form solution, and therefore an iterative approach is pursued. A numerical program in Matlab has been written to find all the solutions for the different frequencies and velocities. In region 1 the iteration tries solutions of v_p between zero (lower boundary) and the v_T (upper boundary). The iteration approach tries a value of v_p, which is the average of the upper and lower boundary. Depending on the signs of the result of relation 3.14 the upper or lower boundary is adjusted to this average. This is repeated until the value of relation 3.14 goes below a value of 1.0e-14. Region 2 uses a slightly different iteration method, because solution for region 2 (formula 3.15) contains an asymptotes due to the term that contains the tangent, the asymptote occurs when:

$$\frac{2\pi\cdot fh}{v_p}\sqrt{\left(\left(\frac{v_p}{v_T}\right)^2-1\right)}=\frac{\pi}{2}, \qquad (3.16)$$

Rewriting for phase velocity results in

$$v_p=\sqrt{\frac{16\cdot v_T^2(fh)^2}{16(fh)^2-v_T^2}}. \qquad (3.17)$$

The solution of v_p for which formula 3.15 is zero is always left of the asymptote, this can be seen in Figure 3.1.1 which shows the formula 3.15 for a range of values for v_p. In the Figure around 3550 m/s the solution suddenly jumps up and down, which is the result of the asymptote. Because the zero crossing is left to the asymptote the initial upper boundary is the asymptote value of v_p from formula 3.17. Then the rest of the iteration approach is the same as for region 1.

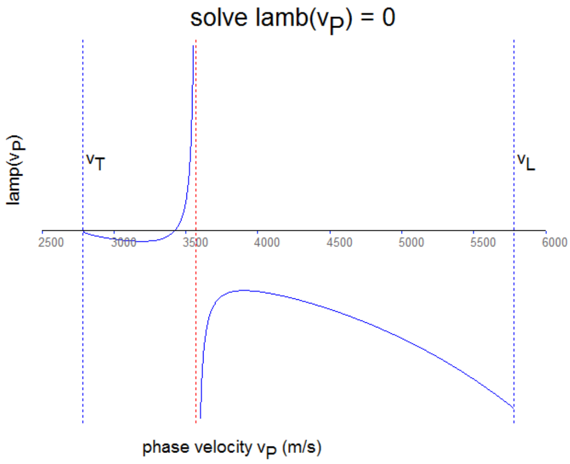

Figure 3.1.1: Symmetric mode solution of formula 3.16 (region 2) for a frequency of 1110 kHz.

Once the phase velocity is known the group velocity can be calculated using the next formula:

$$v_g = \frac{v_p^2}{v_p - fh\frac{d(v_p)}{d(fh)}} = \frac{v_p^2}{v_p - fh\frac{\partial g/\partial(fh)}{\partial g/\partial v_p}} \tag{3.18}$$

Where $g(v_p, fh, \theta)$ comes from formula 3.14 and 3.15. The program calculates solutions of v_p for every temperature separate, therefore g can be written as $g(v_p, fh)$. The derivative $\frac{dv_p}{d(fh)}$ from formula 3.18 can be calculated by rewriting formula 3.19 to be able to get the right hand side of formula 3.18.

$$dg = \frac{\partial g}{\partial v_p} dv_p + \frac{\partial g}{\partial(fh)} d(fh) \tag{3.19}$$

The Matlab code to find the solutions to the Lamb wave relations has been verified with the results obtained by Dodson and Inman. By using the same material properties (6064) the same graphs as Dodson and Inman were obtained, however these graphs will not be shown because Section 3.3 will show the results for aluminium 2024-T3 and some additional new graphs will be shown in Section 3.4.

3.2 Material Constants with Temperature

The theory of Section 3.1 uses three temperature dependent material properties, which are; density, stiffness and Poisson's ratio. This Section will discuss how much these material properties change, over the temperature range of interest, and also how they have been obtained. The material selected for the experiments in this research project is aluminium 2024-T3.

Figures 3.2.1a to 3.2.1c depict the change of stiffness, density and Poisson's ratio with temperature. The density can be calculated by formula 3.7, but values were also found in the Comsol Multiphysics® material database. Values for the changing stiffness and Poisson's ratio (with temperature) have also been obtained from the Comsol Multiphysics® material database. The values of the Poisson's ratio, density and stiffness have been compared to values from ASM database [54] and the change in density with temperature has also been compared to formula 3.7. The values of ASM [54] are not temperature dependent and obtained at ambient temperature (20 ˚C). The change in Stiffness, Poisson's ratio and density with temperature can be seen in Figures 3.2.1a-c.

Description of material properties with temperature is not given for every material. In the material database of Comsol Multiphysics® material properties with temperature have been found for Aluminium 2024-T4. The T4 temper is compared to the T3 an additional natural ageing process with no direct cold working applied. The differences between the two materials are marginal and when storing the T3 temper for several years T4 will be obtained anyhow. Also the stiffness, Poisson's ratio and density are the same for these materials. Comsol Multiphysics® obtained the properties from several locations. The density has been obtained from MIL handbook [55], poison ratio has been obtained at; room temperature value [56], and temperature dependence has been obtained from [57]. The stiffness has been obtained from; room temperature from [56], and temperature dependence from [57].

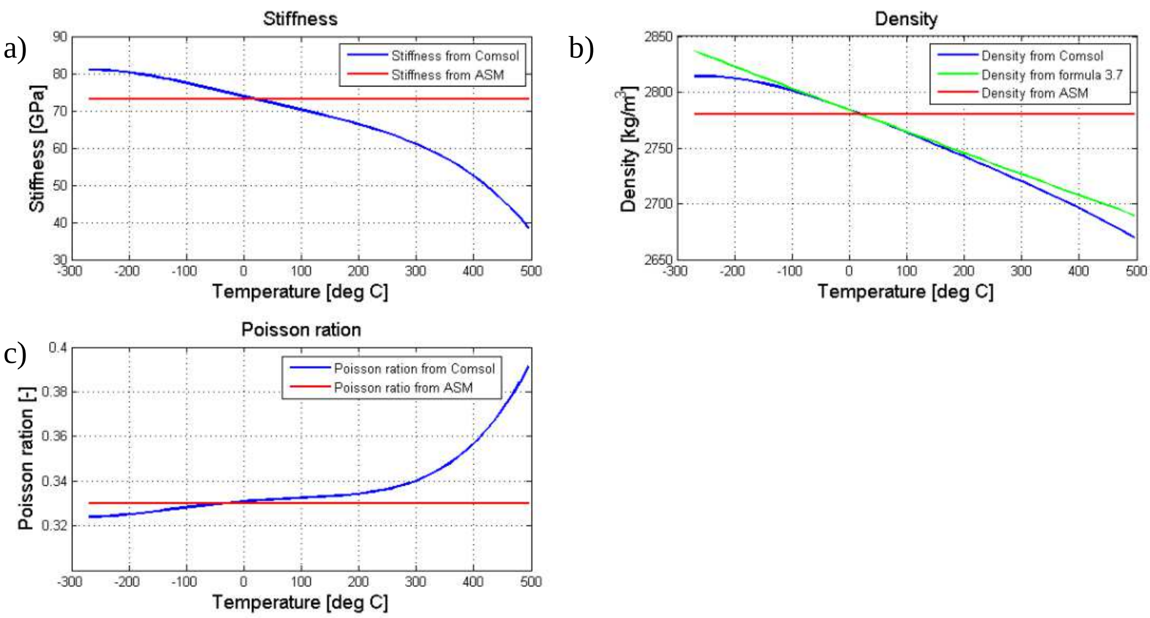

Figure 3.2.1a-c: a) Change of stiffness; b) density; and c) Poisson's ration of Al2024-T4 versus temperature.

Figures 3.2.1a-c show that for the stiffness and the density, the ASM value crosses the values from Comsol Multiphysics® at 20 ˚C, which is an indication that the values match for this temperature. The ASM value for the Poisson's ratio doesn't cross the data from Comsol Multiphysics® 20 ˚C, but the changes with temperature are relatively small over the given temperature range (the change is in the 10^-3). Because this change is so small over the normal operating temperature range of aircrafts the Poisson's ratio can be assumed constant.

When looking at absolute changes with temperature of the other properties, the first thing that is quite clear is that the stiffness changes quite significantly with temperature. This is observed from 75.7 [GPa] at -50 ˚C to 71.33 [GPa] at 70˚C, which is 4.37 [GPa] change in stiffness (roughly 6 percent change to the highest stiffness). The change in density is much less compared to the stiffness. The density becomes roughly 24 [kg/m^3] lighter over the given temperature range, which is less than 1 percent change of the highest density. The Figure shows also that the Comsol Multiphysics® values for the change in density match the ones of the formula 3.7 very well for this range. When looking to a broader spectrum of the temperature range for the density in Figure 3.2.1-b it is clear that below -150 ˚C and above 200 ˚C the material properties from Comsol Multiphysics® seem to diverge significantly from formula 3.7. Therefore, for those temperatures it is better to use the values used by Comsol Multiphysics®, because formula 3.7 might be too simplified. The Comsol Multiphysics® material database indicates that the stiffness and Poisson's properties of Aluminium 2024-T3 have an uncertainty margin of 5% at 0 K and 10% at 773 K. Therefore the results of this program should only be used within the rang specified for these materials, once going outside the range the result will make no sense and will probably not represent reality anymore. A great deal can be related to the Poisson's ration which will reach (according to the polynomial) the value of 0.5 very fast. When the Poisson's ratio will go near this value then the v_L will increase very rapidly and so the results of the lamb wave relation will not make sense anymore.

3.3 Results for Thermoelastic Dispersion relations for Aluminium 2024

This Section discusses the analytical results of the dispersion curves with temperature for aluminium 2024-T3. The temperature range is from -50 ˚C to 70˚C because this is a normal operating temperature range for an aircraft [58, p. 18].

Figure 3.3.1 shows the dispersion curves for both the phase and group velocity under influence of a range of temperatures (-50 ˚C to 70 ˚C in steps of 15 ˚C). In the graph the lines for the S_0 wave are highlighted because these types of waves are used for measuring wave velocities and localization in the remaining Sections of this report.

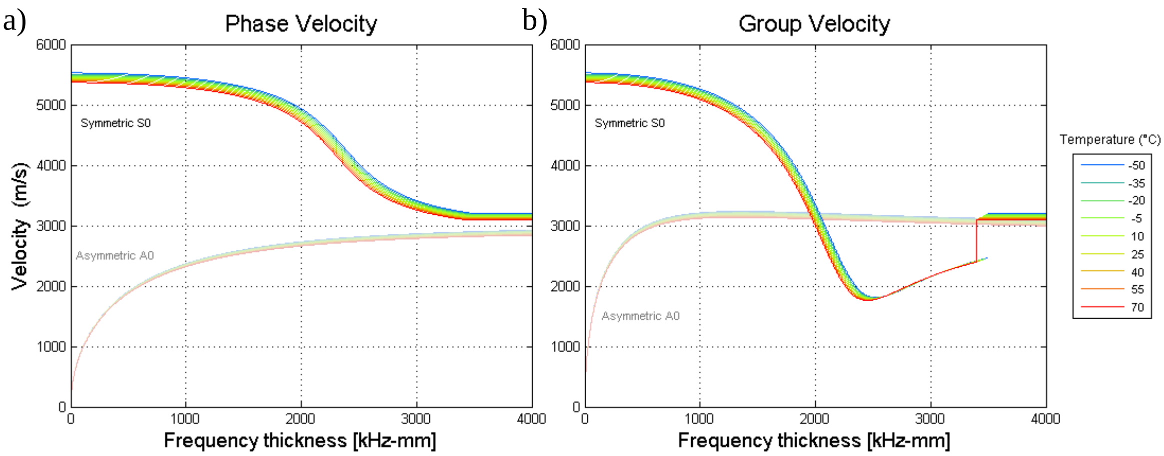

Figure 3.3.1: Dispersion curves for several temperatures for A_0 and S_0 modes; a) phase velocity; b) and group velocity.

Figure 3.3.1 shows the dispersion curves for different temperatures. In the left graph the phase velocity is calculated and the right graph contains the group velocities for the A_0 and S_0 modes. It can be seen that around 3500 [kHz-mm] the phase velocity of the A_0 mode suddenly changes to a straight line. This is most probably due to the approach used by the Matlab® program. This numerical approach to calculate the phase velocity searches for a solution of formula 3.16 close to zero. It assumes the formula is zero when the value is within a range from -10e-14 to 10e-14. This can lead to a sudden change of the slope which results in a jump of $d(v_p)/d(fh)$. Formula 3.14 is affected by this jump and result in this effect of the group velocity around 3500 [kHz-mm]. Because of this rounding error the other graphs derived from this result will show incorrect results when surpassing this point, which is around 3500 [kHz-mm]. The sudden jump in the results around 3500 kHz-mm is not an area of interest for AE because peak frequencies are much lower and therefore very thick plates are necessary to get into this region.

In Figure 3.3.1, it seems that the lines for different temperatures are very close to each other. In order to still be able to separate the results, the derivative of the group velocity with temperature (with respect to zero degree Celsius) have thus been calculated, according to formula 3.20.

$$\frac{\delta v_g}{\delta \theta} = \frac{v_g(\theta) - v_g(0)}{\theta} \tag{3.20}$$

Figure 3.3.2 shows these results. It can be seen that the lines for all temperature lay very close to each other for this temperature range, indicating that the change in velocity is almost linear with temperature. In addition, this graph also shows the temperature invariant points for the S_0 modes as described by Dodson *et al.*, the two temperature invariant points which can be identified by the zero crossing, in this case close to 2640 [kHz-mm] and 3120 [kHz-mm]. These are different values to those found by Dodson et al [36] for aluminium 6064. So material properties seem to influence this behaviour. Figure 3.3.2 also shows that the temperature invariant points seem not to lie on top of each other exactly, suggesting it is not one single point.

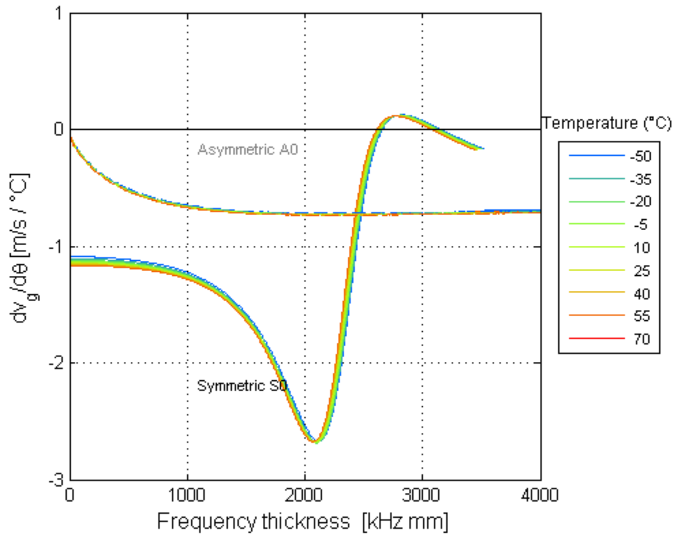

Figure 3.3.2: Normalized change in group velocity with temperature for both A_0 and S_0 modes.

Invariant points do not exist for AE signals because they have much lower frequencies and so are not expected to be in this range, except for very thick plates. The temperature invariant points might be more useful for the active approach. Furthermore, Figure 3.3.2 shows that the A_0 wave changes much less with temperature than the S_0. From Figure 3.3.1 it can be seen that A_0 wave is faster than the S_0 wave for the area where the temperature invariant points occur. Figure 3.3.2 has also been obtained while keeping the density or stiffness constant. This means that the individual effect of the material properties can be investigated because the Poisson's ratio does not change significantly over normal operating temperatures. The results can be found in Figures 3.3.3a and 3.3.3b indicating that the largest effects over normal aircraft operating temperature range is due to the changing stiffness. Figure 3.3.3b for the change of density with temperature has two points where order of the lines inverts, these points occur at 2498 and 3260 kHz-mm and do not coincide with the temperature invariant points.

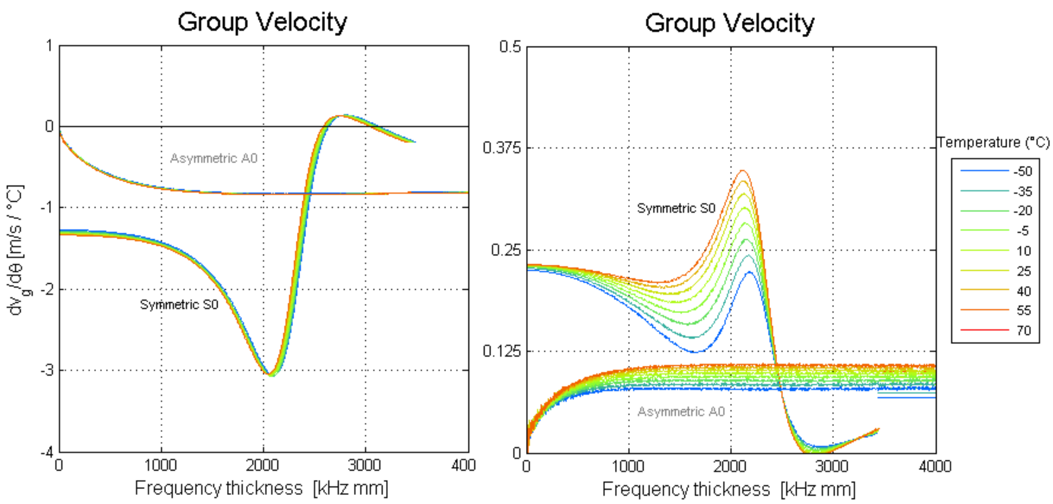

Figure 3.3.3: Normalized change in group velocity with temperature for both A_0 and S_0 modes, due to individual effects of; a) stiffness with temperature; b) density with temperature.

3.4 Invariant points

The temperature invariant points (the zero crossings of the change in wave velocity vs. fh in Figure 3.3.2) discussed previously for the S_0 wave are interesting areas for active SHM approaches, therefore it is worthwhile investigating further. Dodson *et al.* [36] did not give any further discussion on these points. This Section will focus on how these invariant points behave for the entire temperature range for which the material constants are defined.

To investigate the effect of temperature lets first plot the derivative of the wave velocity of the S_0 wave for the full range for which the material constants are given. This is from -270 ˚C to 500 ˚C. Figure 3.4.1 shows this range and from the Figure it can be seen that the zero crossings for different temperatures aren't happening for the same frequency, especially for the higher temperatures. This means that the temperature invariant points are not invariant for this entire temperature range, but change very slightly for normal operation temperatures. This indicates that the second derivative is not zero. The gap in results for the lines at higher temperatures is due to sudden change of the phase velocity resulting in a jump in the group velocity, which has been described in Section 3.3 (about Figure 3.3.1). For higher temperatures this point seems to shift to lower frequency-thickness combinations.

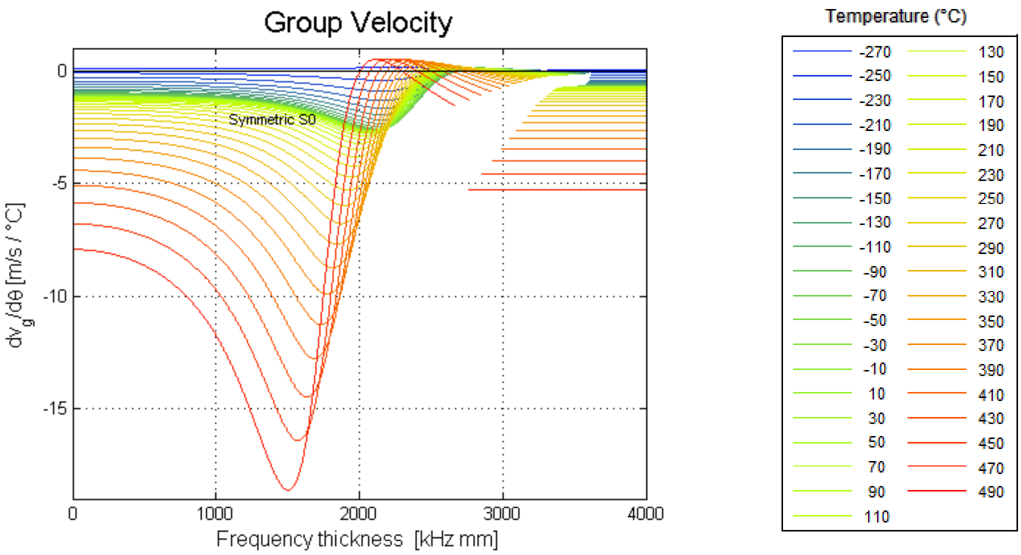

Figure 3.4.1: Normalized change in group velocity with temperature S_0 mode.

That temperature invariant points don't change much with temperature for normal operating temperatures as can be seen in Figure 3.4.2 where the wave velocity is plotted versus the temperature. Where the lines are horizontal the change in wave velocity for that temperature is zero. The graph shows the lines are not completely horizontal for all the temperatures.

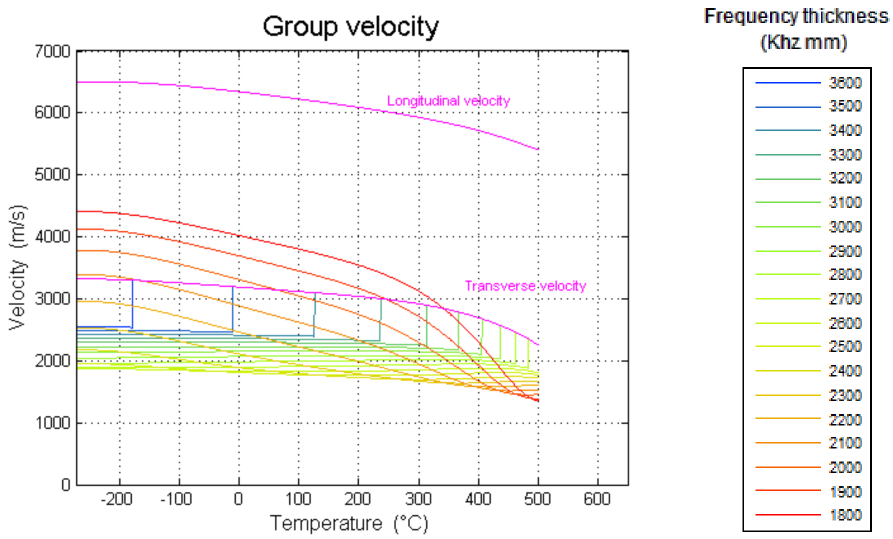

Figure 3.4.2: Wave velocity versus temperature of S_0 waves for several frequencies.

As can be seen in Figure 3.4.1 each frequency has two zero crossings (invariant points). Figure 3.4.3 shows these invariant points for each temperature; in this way it indicates how these invariant points shift for different temperatures. The left Figure shows the frequency-thickness of all the invariant points while the right Figure shows the corresponding velocity at the invariant points. Figure 3.4.4 combines Figure 3.4.2 and 3.4.3 into one Figure.

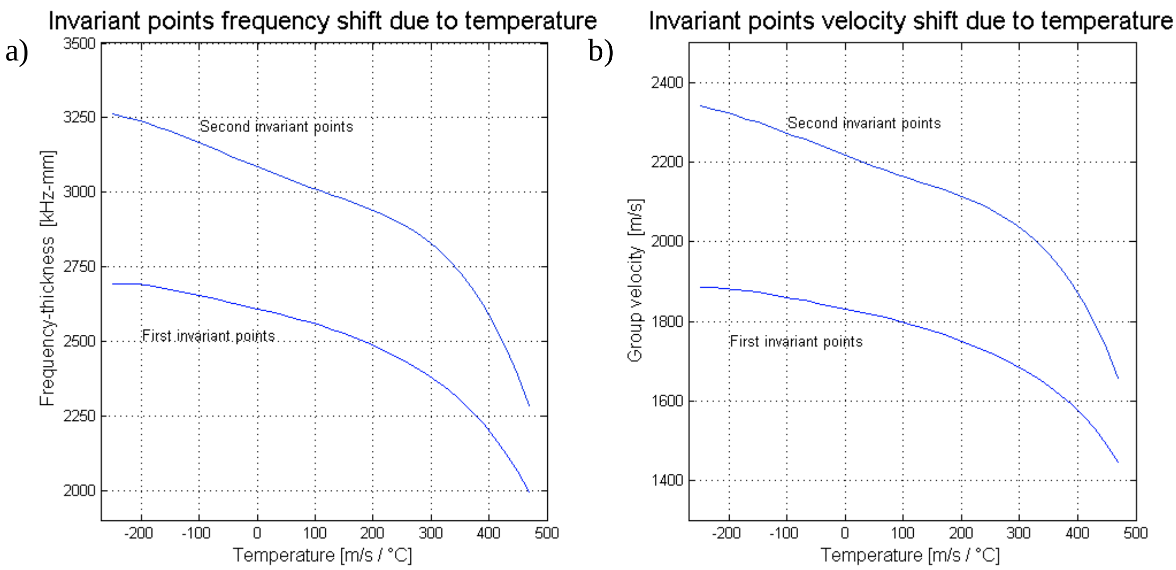

Figure 3.4.3: Shift of invariant points with temperature; a) frequency-thicknesses shift with temperature; b)velocity shift with temperature.

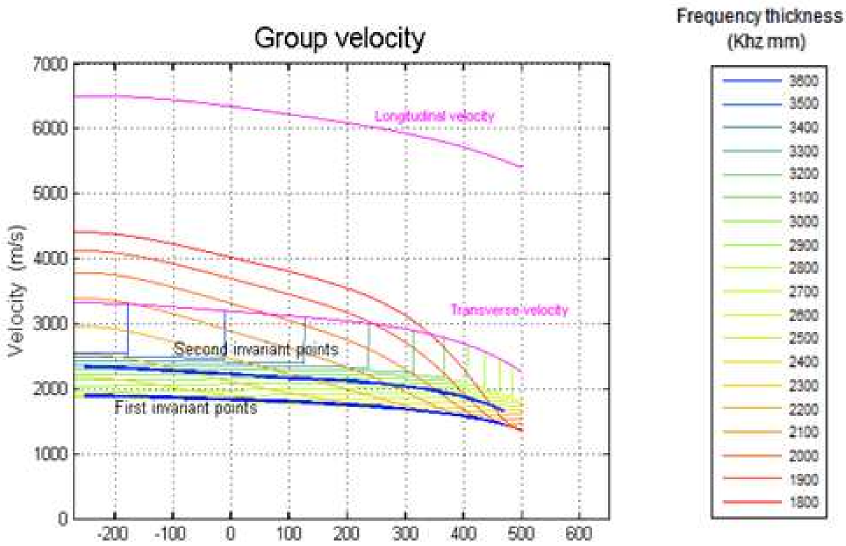

Figure 3.4.4: Wave velocity versus temperatures for several frequencies with an extra indication of the temperature invariant points by the two dark blue line.

Investigating why the temperature invariant points exist is a complex question and will not be answered in this Section, however it will be discussed what the problems are to do so. The invariant points exist only for the group velocity; therefore we start with restating equation 3.18 for the group velocity.

$$v_g = \frac{v_p^2}{v_p - fh\frac{d(v_p)}{d(fh)}} \tag{3.18}$$

Taking the derivative of equation 3.18 with temperature leads to equation 3.21:

$$\frac{dv_g}{d\theta} = \frac{2v_p\frac{dv_p}{d\theta}\cdot\left(v_p - fh\frac{dv_p}{d(fh)}\right) - v_p^2\cdot\left(\frac{dv_p}{d\theta} - fh\frac{d\left(\frac{dv_p}{d(fh)}\right)}{d\theta}\right)}{\left(v_p - fh\frac{dv_p}{d(fh)}\right)^2} \tag{3.21}$$

The left hand side of formula 3.21 equals to zero for the invariant points. For those formula's to be zero at specific frequencies the numerator needs to be zero or the denominator needs to go to infinite, which leads to the following two mathematical conditions:

$$2v_p\frac{dv_p}{d\theta}\cdot\left(v_p - fh\frac{dv_p}{d(fh)}\right) - v_p^2\cdot\left(\frac{dv_p}{d\theta} - fh\frac{d\left(\frac{dv_p}{d(fh)}\right)}{d\theta}\right) = 0 \tag{3.22}$$

$$\left(v_p - fh\frac{dv_p}{d(fh)}\right)^2 = +\infty \tag{3.23}$$

Formula 3.23 shall not go to infinity at the invariant points because v_p & fh are finite as discussed in Figure 3.3.1. Furthermore $\frac{dv_p}{d(fh)}$ is also finite as can be seen in Figure 3.4.5, where the black dotted lines indicate the frequency thickness of the invariant points. Therefore formula 3.22 must be zero at the invariant points.

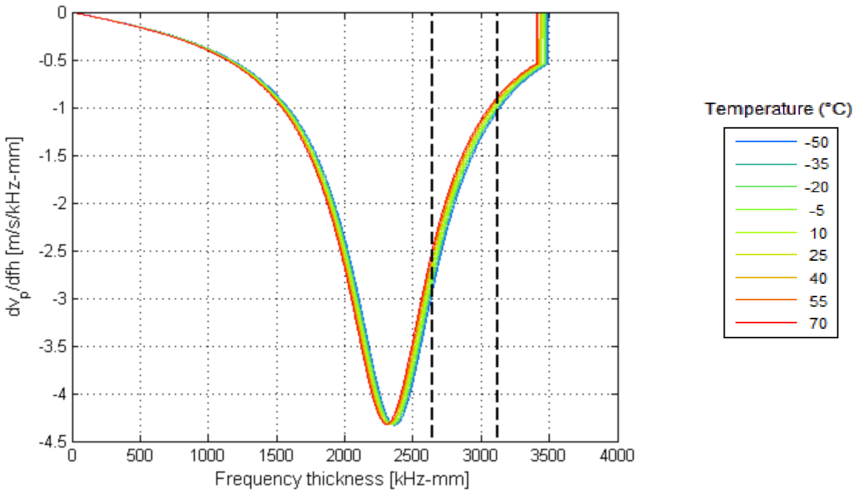

Figure 3.4.5: Normalized derivative of phase velocity with frequency thickness for S_0 wave mode, the black dotted lines indicate the frequency thickness of the two invariant points.

Plotting all the separate terms of formula 3.21 will not provide more information except that it shows that the two terms will be compensating each other resulting in the invariant points. For every temperature the wave group velocity goes to a minimum and increases again with increasing fh, as can be seen in Figure 3.3.1. This increasing behaviour of the group velocity combined with the decreasing behaviour of the group velocity with the temperature can result in the first invariant point where they exactly compensate each other. For the second invariant points it seems the slope op the increasing group velocity is decreasing resulting in the second invariant point. The group velocity is calculated from the phase velocity through formula 3.18. First a physical explanation for the phase velocity should given before the change in group velocity can be explained. The phase velocity is obtained iteratively and therefore this physical explanation does not exist for the trends obtained in figure 3.3.1. Therefore it is difficult to give a physical explanation for the temperature invariant points.

In conclusion of this Chapter, the invariant points shift very little over the normal operating temperature of an aircraft. Therefore it might be interesting to use these points for excluding the impact of temperature in active SHM approaches. Analysis of AE signals is typically performed in lower range of, so these points might not be very interesting for AE approach. The use of these so called temperature invariant points is further complicated because the velocity of these waves are below the velocity of the anti-symmetric wave and also higher modes occur which have higher velocities. The waves with higher velocities reach the ends of the structures faster resulting in reflections, which might impact the S_0 wave. It has also been shown in this Section how much the temperature invariant points shift due temperature, indicating that the change in wave velocity is zero at those points. However, the derivative of the change in wave velocity with temperature is not and shifts the temperature invariant points slightly. It could be useful to investigate further if and to what extent the S_0 wave can be clearly distinguished from the other faster waves in this frequency region. However, this will be a recommendation for further research. The variation of wave group velocity with temperature is greatly influenced by the material properties. Dodson & Inman reasoned that the stiffness, Poisson's ratio and density. The change in Poisson's ratio is so small that this is actually constant.

Chapter 4: Experimental test setup and description of FE models

As explained in the introduction in this report the effect of temperature and load on AE signals were investigated with the FE method and verified through experiments. This chapter discusses the details of the experimental test setup and the FE models. Section 4.1 discusses the test methodology, which is divided into two stages that cover four test variables in both stages. The four test variables are the type of signal, the temperature, the applied load and the angle between the sensor path and the loading direction. The first stage investigates the change in wave group velocity under varying EOC. The second stage investigates how the effect of the change in wave group velocity under varying EOC will affect the capability to localize the damage. Section 4.2 presents the experimental test setup while Section 4.3 discusses the details of the FE models. The results of both experiments and FE models are presented in Chapter 5. However, some measurements that are related to the accuracy and precision of the measurements equipment are highlighted in this chapter.

4.1 Test Methodology

The work was performed in two stages that were the same for the experiments and the FE models. In stage one, the wave group velocities of guided Lamb waves were measured for a range of nine temperature steps from -40 ˚C to 70 ˚C. At each temperature level, six different static loads were applied that ranged from 0 MPa to 250 MPa in increments of 50 MPa. For the effect of temperature results will also be compared to the analytical solution obtained from the model discussed in Chapter 3. In stage two, the localization under influence of EOC is investigated. To do this a representative AE signal, simulating a fracture phenomenon, was emitted from a randomly selected point in the plate. The same temperature and loading conditions were applied as in stage one to investigate its effects on the localization capability.

To measure the effect of load and temperature on AE wave propagation a simple metal plate structure was selected as the test specimen. An aluminium 2024-T3 plate was chosen as this is a very common aluminium type in the aircraft industry. Limited by the size of the fatigue bench, the effective size of the plate was 650 mm in width, 600 mm long and 2.1 mm thick, as shown in Figure 4.1.1. The specimen was in reality larger because on the top and bottom side, an extra 70 mm was reserved for clamping. The rolling direction of the material was along the same direction of the applied load. More details about the design of the test specimen can be found in Appendix A. The numbers of holes in Figure 4.1.1 were drilled to bolt the clamps of the fatigue bench to the plate.

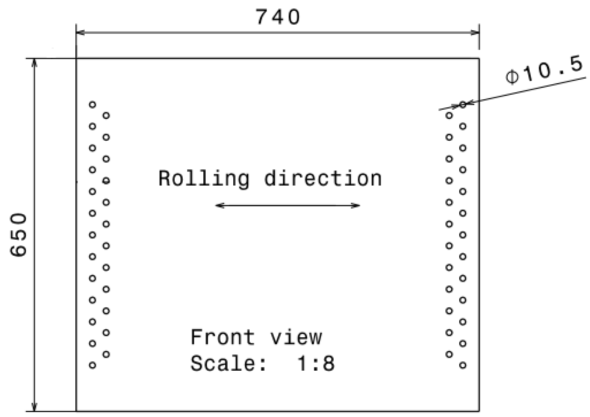

Figure 4.1.1: Graphical illustration of test specimen.

4.1.1 Test variables

There were four test variables in this study that were the same during the two stages in this thesis. The four test variables were;

- The type of signal used for actuations
- The temperature
- The applied uni-directional static load
- The angle with respect to the load

To be able to measure repetitively and accurate wave velocities with a passive SHM system, a signal was sent from the signal generator. From the signal generator one output goes to the actuator and a second output goes to the AE system to trigger the threshold. With this approach the signal was actuated at the same time as the trigger start the recording of the AE system. The first test variable was the type of signal that was sent from the signal generator. In stage one where wave velocities will be measured, a Hanning windowed signal had been selected because the small bandwidth of the signal minimizes dispersion of the wave. Two frequencies of 150 kHz and 300 kHz were investigated experimentally but the FE model is only run for the 150 kHz signal. The 300 kHz Hanning window is not calculated because of the increased computational load due to decreasing time step and element size as will be explained in Section 4.3. For these two frequencies the results of the dispersion curves in chapter three describes no significant difference and therefore similar results should be obtained anyhow. Hanning windows can be mathematically described by formula 4.1. Where f_{act} is the actuating frequency, t is the time $\in \left[0, \frac{n_c}{f_{act}}\right]$ and n_c is the number of cycles of the modulated sine wave. This mathematical description can be transformed into a data file that is used as input for both the signal generator and the FE model as discussed before.

$$H(t) = \frac{1}{2}\left[1 - \cos\left(\frac{2\pi f_{act} t}{n_c}\right)\right] \cdot \sin\left(2\pi f_{act} t\right) \qquad (4.1)$$

In stage 2 the representative AE signal was obtained experimentally in order to obtain a representative AE signal of the pencil break and thus avoid lack of consistency from one pencil break test to another. A pencil lead break test was executed multiple times at 15 cm distance to a sensor. In the measured transient recording the part of the signal related to S_0 plus A_0 is selected as the representative signal. The resulting representative signal with its corresponding Fourier transform can be found in Figure 4.1.2a and 4.1.2b. The signal has a peak frequency of 156.25 kHz and a centroid frequency at 207.65 kHz.

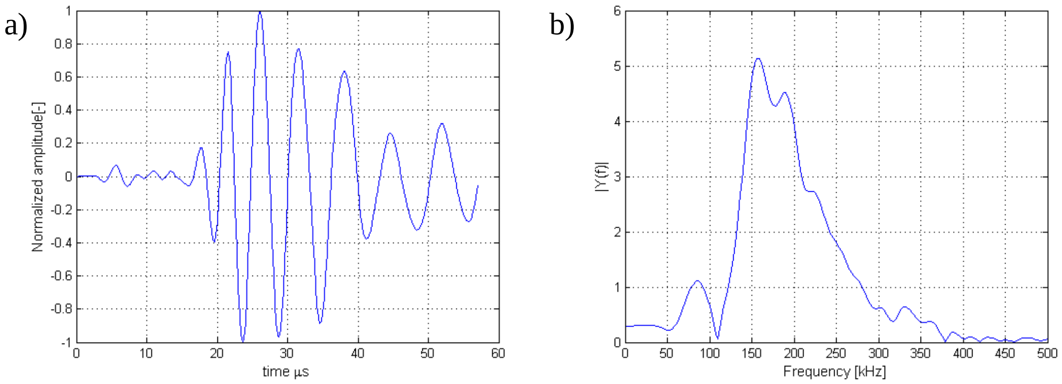

Figure 4.1.2: The representative AE signal; a) normalized waveform; b) corresponding FFT.

The second and third test variables are the Temperature and Load, which were applied together in combinations of the two. The testing range for the temperature and load were chosen such that it represents the expected temperature ranges during operational life of a civil aircraft, which was -50 ˚C to 70 ˚C, in steps of 15 degrees. The load range was focused on static tensile forces only because the plate buckles quite fast under compression and dynamic loads are outside the scope of this study. Furthermore, the load was kept below the yield stress to ensure no plasticity occurred. The yield strength of Aluminium 2024-T3 is 324 MPa [54]. The load is applied in steps of 50 MPa until 250 MPa. In this way the stress levels inside the plate did not go beyond the yield stress of 324 MPa even if some overloading from the fatigue bench occurred. The contour of the von-Mises stresses is depicted in Figure 4.1.3 for an applied load of 250 MPa. The FE model will be discussed in more detail in Section 4.3.2 however, the Figure shows the internal stress distribution at 250 MPa. Table 4.1 shows the combinations of load and temperature for which experiments (blue and yellow cells) and FE models (yellow cell's only) are executed. Initially, multiple FE programs at higher stress levels were planned, however due to time limitations this could not be achieved.

Table 4.1: Test-Matrix, yellow cell's executed in FE simulations, all cells executed during the experiments.

		Temperature ˚C								
		-50	-35	-20	-5	10	25	40	55	70
Stress MPa	0									
	50									
	100									
	150									
	200									
	250									

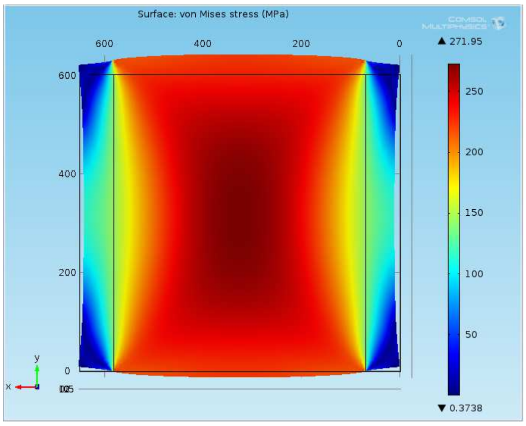

Figure 4.1.3: Stationary plot of stress levels with applied load of 250 MPa along the top & bottom sides of the plate.

The last test variable is the angle with respect to the load. As described in the literature study in Section 2.4.2, the effect of load makes the group velocity of the wave angle dependent. Therefore, several paths from source to sensor that have different angles to the load direction were required as to measure this angle dependent effect. To measure the wave velocities in stage one as accurate as possible the actuating sensor has been put in the corner resulting in the longest paths to the other sensors. As a side effect the different distances between the sensors results in different attenuation for each path. The array for stage one can be found in Figure 4.1.4a where sensor 1 is the actuating sensor and sensor 2 through 6 are the passive sensors. Additionally, Figure 4.1.4a also shows the angle with respect to the load for each sensor couple. In stage two, the main focus is on the localization of AE signals with four sensors. A fifth sensor was used as the emitting source. The sensor emitted an AE signal that was obtained with a pencil lead break test; more details about this will be discussed in Section 4.2. The location of sensor 1 to 6 stays the same in both stage one and two. The seventh sensor is added after stage one was completed, and sensor 3 and 4 were still attached to the plate but were not used. The array in stage two can be seen in Figure 4.1.4b. The sensors add mass to the plate and thus change the inertia of the combined structure. However, the effect of this is assumed to be small on the propagation velocities of the waves and is therefore neglected. The exact locations of the sensors are summarized in table 4.2.

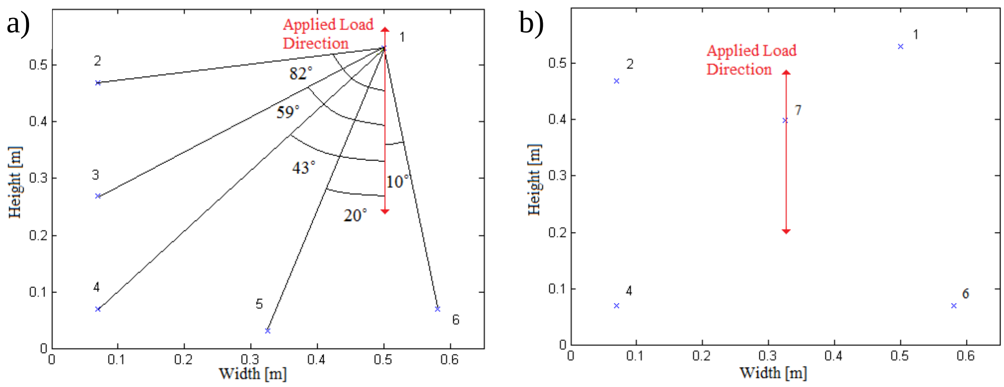

Figure 4.1.4: Sensors locations; a) array to measure wave velocities in stage one; b) array to measure AE signals in stage two.

Table 4.2: Locations of sensors for both arrays.

Sensor #	x-location [m]	y-location [m]
1	0.500	0.530
2	0.070	0.470
3	0.070	0.270
4	0.570	0.070
5	0.325	0.030
6	0.070	0.570
7	0.325	0.400

4.2 Experimental test setup

This sub-section will describe the experimental test setup. The test setup consists of a Vallen AMSY-6 Acoustic Emission system with eight channels in order to experimentally obtain the signal changes due to temperature and load [59]. Furthermore, seven VS150-M piezoelectric transducers were attached to the front side of the plate and four thermocouples were attached at the backside of the plate to monitor the temperature. Additionally, a 500 [kN] MTS fatigue bench was employed to apply the load and a signal generator and amplifier were used to actuate signals at one of the piezoelectric transducers. To control the temperature, a climate chamber was constructed from isolation material (Ursa XPS [60]), and built around the fatigue bench. Its design can be found in Appendix B. Figure 4.2.1 illustrates the experimental setup. These parts of the test setup will be separately discussed in this sub-section.

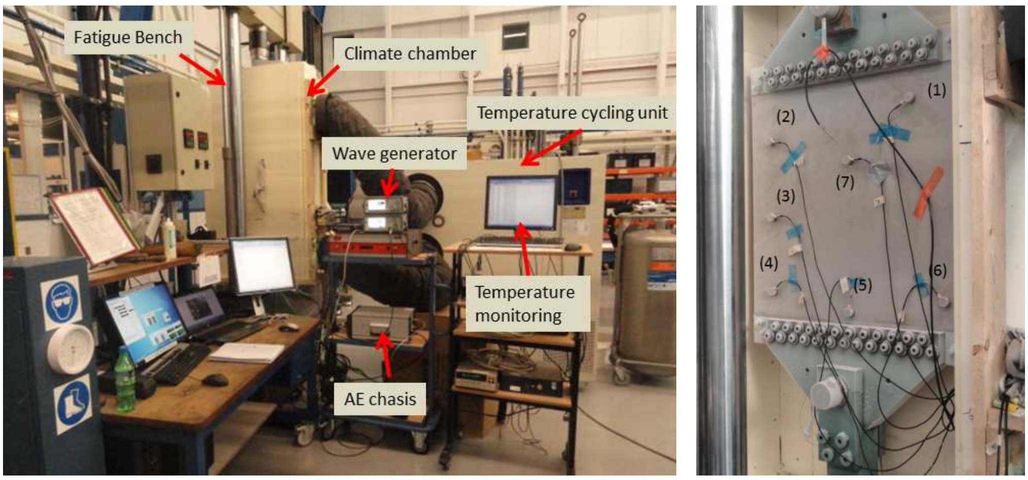

Figure 4.2.1: The experimental setup and the layout of the sensors on the test panel.

4.2.1 Vallen AMSY-6 Acoustic Emission system

The AMSY-6 system is a multi channel (in this case 8 channel) AE system, which records transient signals and computes the signal characteristics. Moreover, the software of the systems calculates the emitting sources locations by using dedicated algorithms. In this study, the Geiger's planar location algorithm was used [61] for planar localization. Preamplifiers were used to amplify the analogue signal so as to reduce transmission losses;

the software compensates this amplification to obtain the original signal as good as possible. The sampling rate was set at 5 MHz, which was clocked with a 40 [MHz] internal clock, thus the clock error was maximum 25 nano seconds.

4.2.2 Piezoelectric sensors

The selection of the piezoelectric transducers is greatly influenced by the operating temperature, which is between -50 ˚C to 70 ˚C. This temperature range reduces the available options quite significantly. The selection list of sensors was narrowed down to sensors form Vallen systems only. The frequency spectrum of the sensor and the material of the wear plate to connect the sensors to a structure are important characteristics that were taken into account in the selection process. The frequency spectrum for the AE signals is about 40 to 450 kHz and the wear plate needed to be non-metallic to avoid electric interference with the aluminium test specimen. Considering the above requirements, the VS150-M type sensor was chosen. This sensor has a ceramic wear plate, its operational temperature range is from -50 ˚C to 100 ˚C and the frequency spectrum is from 50 to 450 kHz as Figure 4.2.2 illustrates. More characteristics and properties of this sensors can been found in Appendix C. The manufacturer stated that the active element has a radius of 6.35 mm and a thickness of 6.35 mm.

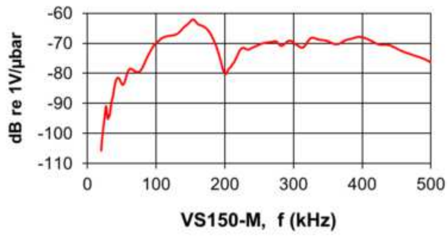

Figure 4.2.2: Sensitivity curve of sensor VS150-M

During a discussion with a representative from Vallen Systeme GmbH it was discussed that the piezoelectric constants do not change much over the temperature range of interest[2]. However, there was no reference to back up this statement. Nevertheless, the properties of the piezoelectric transducers are assumed to be constant with temperature.

Epotek 734 (from Dow Corney) was used to attach the sensors to the plate. The operating range of the coupling adhesive without significant properties degradation is 20-150 ˚C according to its specifications [4]. It was known that Epotek 353ND from [30] does not degrade in the temperature range from 20-150 ˚C. The glue used in these experiments is similar to Epotek 353ND, the properties remain stable according to the manufacturer from -50 ˚C to 70 ˚C. However, the bonding of two of the sensors degraded so much that they fell off during the experiments, but this can also be due to the reasonable swift changes of the temperature during the experiments in combination with loading and unloading the plate. Nevertheless, degradation of the adhesive layer mainly affects the amplitude and not so much the wave velocities.

[2] The representative from Vallen was Thomas Thenikl, the discussion took place at May 2nd 2014.

4.2.3 Thermocouples (K-type)

Thermocouples were used to measure the temperature at the four sensor locations (sensor 1, 2, 4, and 6) shown in Figure 4.2.1. The thermocouples were located on the backside of the plate to which the sensors were glued. In this study, thermocouples type K were selected because of their good sensitivity and accuracy at the temperature range of interest. These sensors were there to check the temperature distribution over the plate during the experiments, since the place was contained inside an environmental chamber. During the experiments the temperature variation over the sensors gave a maximum standard deviation of 1.3 ˚C. For the negative temperatures it was more difficult to get the precise temperature as stated table 4.1. Therefore the temperature steps during the experiments were; 70, 55, 40, 25, 12, -3.5, -17, -32.5, -41 ˚C. The environmental chamber was unable to reach the final desired value of -50˚C even when providing the temperature cycling unit with liquid nitrogen.

4.2.4 Hsu Nielson test (ASTM E976)

Pencil lead break test, known as Hsu-Nielson test [7], were taken in order to obtain a representative signal and check the connection between the structure and the sensors. As in the Figure 4.2.3 a pencil lead break test was used to break a 3mm long lead pencil with thickness 0.5mm under an angle of 30 degrees. The Teflon shoe can help to support in obtaining similar pencil lead break signal.

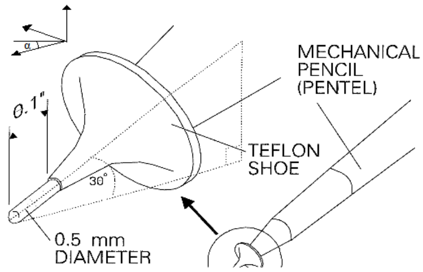

Figure 4.2.3: Pencil break test specifications

4.2.5 Signal Generator and Amplifier

To actuate the Hanning window and the representative AE signal a signal generator with an external amplifier was used. The signal generator is Agilent 33522B and has an output of 20 V_{pp} and a sample rate of $250 \cdot 10^6$ samples per second. The amplifier is of the type Agilent 33502A which amplifies the signal to 42 V_{pp}. The signal was sent every second to allow for multiple measurements while giving time for the previous signal to vanish before the next signal was excited.

4.2.6 Threshold

The AE system starts recording when the AE signal crosses a fixed threshold. However, it is not trivial to select the correct threshold. When a low threshold is selected the recording can be triggered by background noise, resulting in wrong identification of damage in the signal. On the other hand when a high threshold has been selected it can results in a delay in measured TDOA as shown in Figure 4.2.4. This results in a wrong measurement of group velocity, which on its turn impacts the localization. When the threshold has been set too high it can miss the S_0 wave completely and then be triggered by the stronger A_0 wave mode.

Therefore selecting a correct threshold value is very important in obtaining correct TDOA measurements.

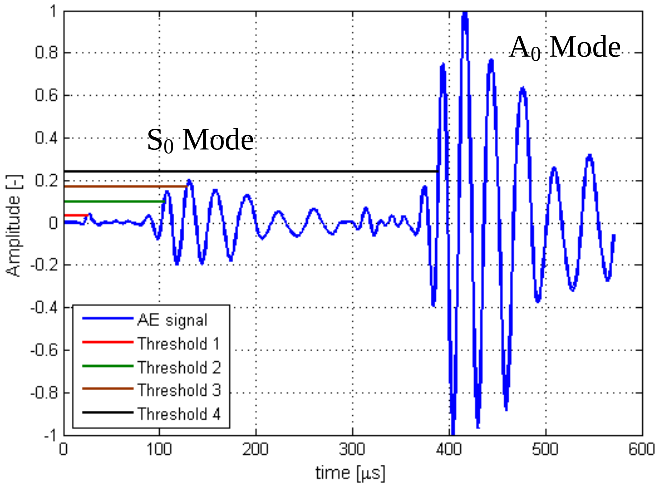

Threshold #	Thres-hold value	Trigger time [µs]
1	0.03	25
2	0.1	105
3	0.17	128
4	0.24	389

Figure 4.2.4: Impact of threshold level on change in TDOA.

The Vallen Amsy AE system was used to investigate the effect of different threshold levels on the change in TDOA. An array similar to Figure 4.1.3a with sensors 1, 2, 4, 6 and an extra sensor at a location of (x=0.325, y=0.58) were used to check the change in TDOA due to different thresholds. Firstly the TDOA was measured with a threshold of 36 dB and then for other thresholds the difference in TDOA was calculated with the reference at 36 dB. The results are presented in Figure 4.2.5.

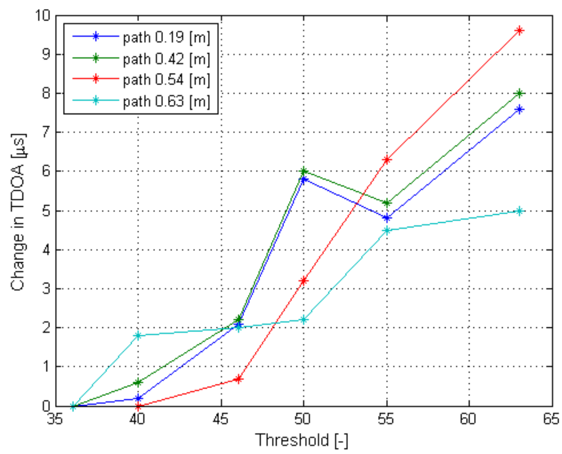

Figure 4.2.5: Change in TDOA with threshold.

Figure 4.2.5 shows that there is an increase in TDOA when the threshold is raised, this follows that waveform takes time to rise in amplitude and a higher threshold result a later part of the waveform to cross the threshold. The change in TDOA over 30 dB range (from 36 to 66 dB) is in the range of 5 to 9 [µs]. This change is more significant than changes in TDOA due to temperature or load, which combined effects, are in the range of minus 3 to plus 4 [µs] (as measured during the experiments, results from chapter 5). During the experiments a trigger signal from the signal generator starts the recording of the AE signal and therefore a manual correction is applied to correct for the part of the signal that happens before the threshold is crossed. This manual correction process looks at every channel at the transient recording and reads for a time interval from where the signal starts to where the signal reaches the threshold. This change in TDOA can be different for each sensor due to the different distances or due to temperature and load. When correcting the results with this approach results were obtained that made more sense. After obtaining the entire correction factor an average correction factor per sensor path was calculated. These correction factors can be found in table 4.3 and the corresponding sensor paths are shown in Figure 4.1.3.

Table 4.3: Average correction factors applied.

Sensor path	1-6	1-5	1-4	1-3	1-2
Angle	9,87	19,29	43,07	58,84	82,06
Average correction factor [µs]	-1,09	-0,86	-1,88	-1,29	-2,12

Background noise measurements indicated that the noise levels were close to 38 dB. Possible noise sources were noise from the hydraulic lines. It was observed that even with maximum amplification of 42 volts it was sometimes difficult to measure a signal with all the sensors. Therefore, a threshold of 41.1 dB and 30 dB were selected for stage 1 and stage 2 respectively. The reason for this is that the AE signal had a relatively short strong peak and it was expected that this would lead to faster attenuation. As a comparison the Vallen Amsy system also has an internal pulse, which is a 100-volt signal.

Table 4.4: Summary of threshold per stage.

Stage #	Focus	Threshold [dB]
1	Wave velocities with EOC	41.1
2	Localization of AE signals	30

4.2.7 Comparing sensor response with Laser Vibrometer

The response of the Vallen VS150-M sensor was compared with the response of the plate by a laser vibrometer of the type Polytec RSV150. A 5 cycle 150 kHz Hanning window was excited. Figure 4.2.6a shows the test setup and Figure 4.2.6b presents the response of the laser and the piezoelectric sensor. Exact comparison of both responses is not possible because the distance from source to measurement location is 30 cm for the laser vibrometer and 36 cm for the piezoelectric sensor. This 6 cm difference can cause differences, which can be related to the effect that waves travel different paths and perhaps at different velocities resulting in wave packages separating from each other. The graph shows the part of the measured response, which has the biggest amplitude. The two responses are alike which indicates that the connection of the sensor to the structure is good enough to transfer the wave properly.

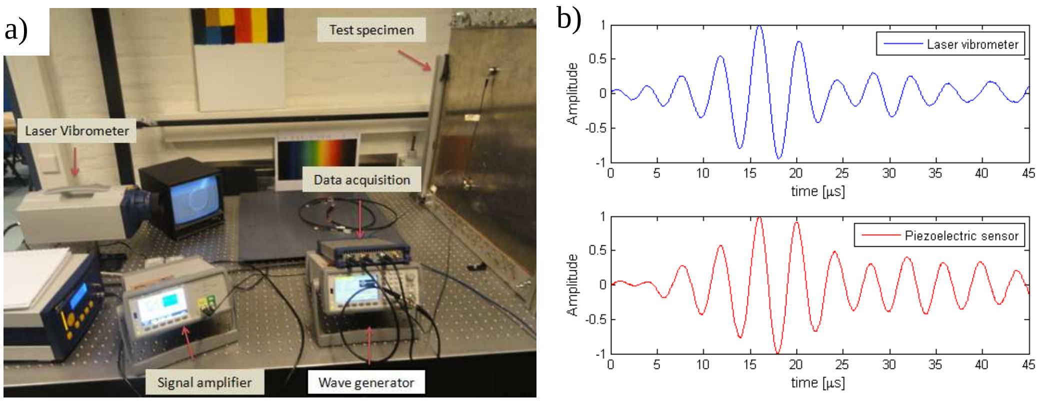

Figure 4.2.6: a) test setup; b) comparing normalized response of piezoelectric sensor (VS150-M) with laser vibrometer.

4.3 FEM modelling with Abaqus/CAE®

To verify the experimental results the FE model should accurately describe the experimental test setup discussed in the previous Section. A finite element approach was used in the Abaqus/CAE® modelling environment. Initially Comsol Muliphysics® has been used, however due hardware limitations and reduced computational speed compared to Abaqus/CAE® it was decided to switch to Abaqus/CAE®. This Section discusses the FE models, and in specific how it matches with the experimental test setup. Two types of geometries were constructed. A small model (quarter of a plate) with one sensor path was used to investigate the effect of temperature on wave speeds while in order to study the effect of load or combined temperature and load on wave speeds, a model that matches the experimental test specimen was developed. The models do not include damping because the focus is on the changing wave speeds and not on the changing amplitude. The results of these FE models are presented in Chapter 5. Because the model is rather large it was run in batch mode on the cluster, Appendix E explains how to run on the cluster.

4.3.1 Modelling Geometry and boundary conditions

The first thing to model is the geometry. To simplify the model a quarter of a plate is modelled with two sensors at 150 mm distance apart. In this way the velocity of the wave can be measured under changing conditions of temperature and load. A larger model has also been developed which is a duplication of the test specimen and so has multiple angles to measure the effect of load. These two models are called model 1 and model 2 respectively.

<u>Model 1</u>

A plate of 200 mm length, 75 mm width and 2.1 mm thickness was modelled. A quarter of a sensor was modelled as the actuating sensor and was placed at one corner. On the same edge at 150 mm distance between the cores another half a sensor was placed. For the sensors only the active elements were modelled which have a radius of 6.35 mm and a height of 6.35 mm. The assembly can be seen in Figure 4.3.1a.

a) 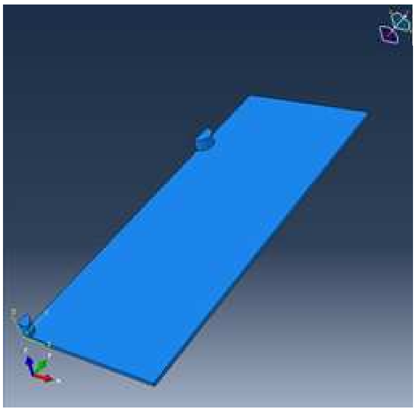 b) 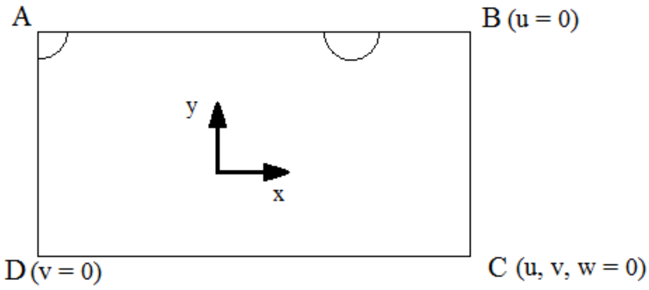

Figure 4.3.1: a) Assembly of parts in model 1, Abaqus/CAE® render; b) indication of boundary conditions.

Several boundary conditions are required to be able to apply load and actuate a signal in the corner sensor. Furthermore, Abaqus/CAE® works with steps to calculate the application of loads and boundary conditions, each boundary condition needs to be assigned to at least one step. This model is time dependent and runs in two separate steps. First in a static general step the load was applied, in this way the ramp up of the load did not create a pulse signal in the second step, which was a time dependent step.

To apply load on the side surfaces of the model the plate needs to be fixed in three directions. A fixed displacement boundary conditions were applied on edge elements as can be seen in Figure 4.3.1b. On the edge through the thickness at corner C displacement was restricted in both x-, y- and z- directions. Furthermore, the edge through the thickness at corner B has been restricted in x-direction and the edge through the thickness at corner D was restricted in y-direction. Additionally, symmetry plane boundary conditions were introduced at the surfaces through thickness at edges AB and AD. These boundary conditions were introduced in the first step and propagated into the second step.

To be able to measure or apply a voltage difference both sensors need to be grounded. This was done by placing a zero voltage boundary condition on the surface of the sensors that is connected to the plate. When applying a voltage to the actuator, first another zero voltage boundary conditions needed to be applied to the top surface during the static general step where the load was applied, otherwise still a voltage shock would occur due to the deformation of the piezoelectric sensor with the applied load. The zero voltage boundary conditions was not propagated to the time dependent step but exchanged for a voltage signal of the Hanning window that was to be actuated.

Model 2

This FE model simulates the test specimen that was used in the experiments. The model simulates the effective size of the plate, which was the plate minus the area between the clamps. The size was therefore 650 mm width, 600 mm height and thickness 2.1 mm. The same sensors as in model 1 have been modelled. An assembly of the sensors and the plate can be found in Figure 4.3.2a.

b)

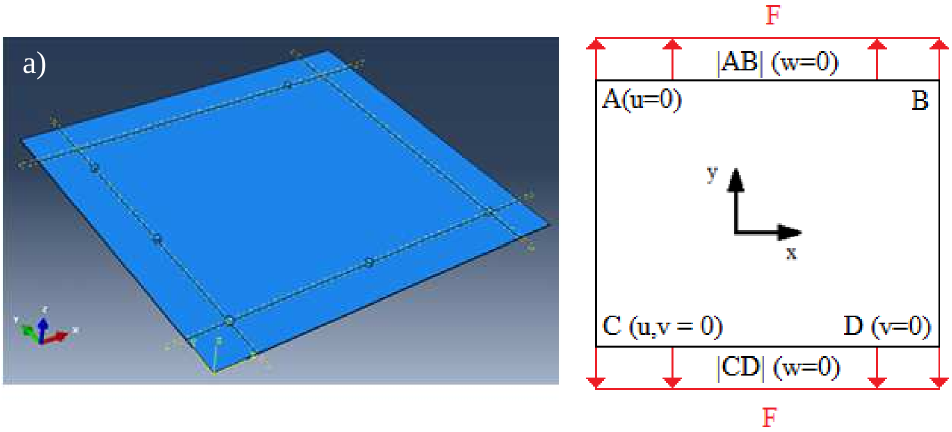

Figure 4.3.2: Assembly of parts in model 2, Abaqus/CAE® render; b) indication of boundary conditions.

To apply loads the model needed to be constrained in x, y, and z direction. Therefore boundary conditions (modelled as fixed displacement boundary conditions) were introduced that were similar to the experiments. As shown in the former Section about the experimental test setup the plate was clamped at two ends of the plate. Therefore the boundary conditions needed to represent the edge where the clamps edges meet the plate. After modelling several different sets of boundary conditions on the plate and apply the stress the following set leadt to the best results in terms of stress. The tension load was applied to a sub-section of the entire plate, Section AB and Section CD, as Figure 4.3.2b highlights. There were several edges that had boundary conditions, the first is applied to the edge that goes through the thickness at location C. This edge had two boundary conditions that deny any displacement in x- and y-direction. Secondly, the edge that goes through the thickness on location D had one boundary condition that restrained any displacement in y-direction. Thirdly the edge through the thickness at location A prohibited any displacement in x-direction. Finally the two edges of AB and CD on the topside of the panel were restrained in displacement in the z-direction (due to the clamping). When also restraining the two edges in the z-direction on the bottom of the plate then the model calculates significant extra stress around these edges of the plate. These boundary conditions were introduced in the first step and propagated into the second step.

To be able to measure or apply a voltage difference both sensors need to be grounded. This was done by placing one zero voltage boundary condition on the surface of the sensors that was connected to the plate. Just as in model 1 an extra zero voltage boundary conditions needed to be applied to the top surface during the static general step where the load is applied. This zero voltage boundary conditions also was not propagated to the time dependent step but exchanged for a voltage signal of the Hanning window that was to be actuated.

4.3.2 Modelling material properties

The two structural elements, the plate and the piezoelectric elements both have their own material properties. The plate was set as aluminium 2024-T3. The material properties for this material have been obtained from Comsol Multiphysics® library. The material properties were also used in the analytical solution for the effect of temperature in chapter 3 and therefore they have also been used in the Abaqus/CAE® model. Table 4.5 summarizes the material properties for four temperatures. The models were run several times for each temperature to obtain the results for the correct EOC

Table 4.5: Material properties of Aluminium 2024-T3 given for four temperatures.

Temp ˚C	Temp [˚K]	Density	Stiffness [Gpa]	Poison ratio [-]
70	343	2770,06	71,3	0,33
25	298	2779,21	73,0	0,33
-5	268	2785,05	74,1	0,33
-41	232	2791,70	75.4	0,33

Modelling piezoelectric sensors requires knowledge of the properties of the active element of the sensors used. Appendix C provides the piezoelectric properties provided by the manufacturer, the values are summarised in the coupling matrix in formula 4.2. To fully model the piezoelectric behaviour, additional constants were required for the compliance matrix; these values were obtained from data sheets [62] from comparable materials (type BM500). The additional elastic compliance constants used were: S_{12} = -5.0· 10^{-12}[C/N], S_{13} = -6.0· 10^{-12}[C/N], and S_{55} = 45· 10^{-12}[C/N]. From these properties the elasticity matrix as in formula 4.3 has been calculated which values were used in the Abaqus/CAE® model. Furthermore, the electric permittivity in the model used 1.638E-8 [F/m], which follows from the relative permittivity given by the manufacturer through relative permittivity $= \varepsilon_{33}^{T}/\varepsilon_0$

$$d_{ij} = 10^{-12} \cdot \begin{bmatrix} 0 & 0 & 0 & 0 & 600 & 0 \\ 0 & 0 & 0 & 600 & 0 & 0 \\ -195 & -195 & 460 & 0 & 0 & 0 \end{bmatrix} \tag{4.2}$$

$$E = 10^{10} \cdot \begin{bmatrix} 9.3153 & 4.5534 & 4.3796 & 0 & 0 & 0 \\ 4.5534 & 9.3153 & 4.3796 & 0 & 0 & 0 \\ 4.3796 & 4.3796 & 8.0292 & 0 & 0 & 0 \\ 0 & 0 & 0 & 2.2222 & 0 & 0 \\ 0 & 0 & 0 & 0 & 2.2222 & 0 \\ 0 & 0 & 0 & 0 & 0 & 2.2222 \end{bmatrix} \tag{4.3}$$

4.3.3 Mesh elements size, Time step and Threshold

To let the FE method properly calculate the physics of the model, the right elements need to be used. This Section describes the mesh and time step used.

An independent rectangular mesh was employed to facilitate the meshing procedure of the plate and the circular sensors. The 8-node C3D8R element with reduced integration and hourglass control was selected for the plate, while the 8-node C3D8E was selected for the meshing of the sensors. The model was constructed in Abaqus/CAE® modelling environment in order to verify experimental results. This model needs to be stable in both spatial and time domain. The minimum element size is derived from the smallest wavelength. For a good spatial resolution Moser et al. [63] suggested to use a minimum of 20 nodes per wavelength, but Chen et al. [64] also stated that 10 nodes per wavelength should be sufficient as expressed in equation 2.26:

$$L_e = \frac{v_p}{10 f_{max}} = \frac{\lambda_{min}}{10} \tag{2.26}$$

The characteristic length of the element was very small compared to the wavelength and therefore large (non-linear) deformations are not expected. The time stability was investigated by Chen et al. [64], where they used a minimum of 20 points per cycle at the highest frequency of the simulated Lamb wave and it expressed mathematically as 2.25:

$$\Delta t = \frac{1}{20 f_{max}} \tag{2.25}$$

The maximum of 150 kHz signal of the Hanning window, used for verifying the wave velocities, was the most stringent condition for the element size and time step, which resulted in a maximum of 1 mm characteristic length and a time step of 1.0e-7 [s]. The resulting mesh of model 1 and 2 can be found in Figure 4.3.3 and Figure 4.3.4 respectively.

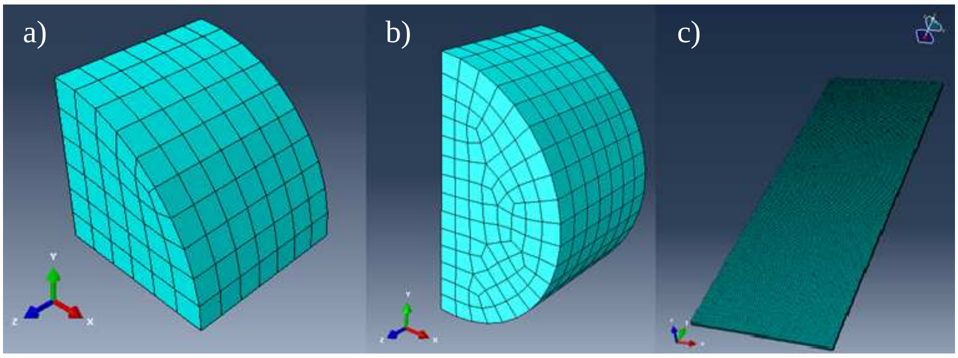

Figure 4.3.3: Part meshes of model 1; a) mesh of quarter sensor; b) mesh of half a sensor; c) mesh of the plate.

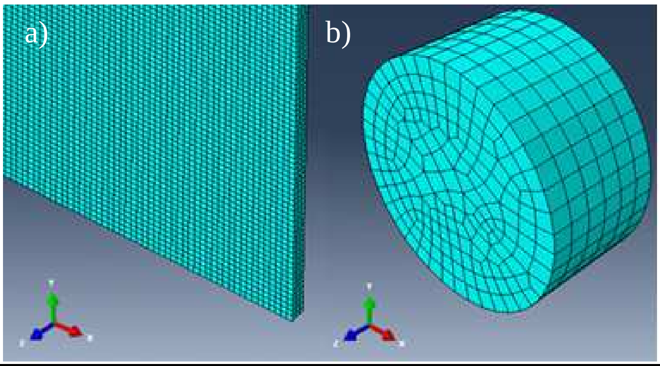

Figure 4.3.4: part meshes of model 2; a) mesh of part of the plate; b) mesh of one full sensor.

4.3.4 Actuator Minimum Size

Viktorov [65] described a sinusoidal relation between the actuator optimum diameter and actuator frequency as follows:

$$2R = \frac{v_p}{f_{act}}\left(n + \frac{1}{2}\right) = \lambda\left(n + \frac{1}{2}\right) \qquad n = 0, 1, 2, 3\ldots \qquad (4.4)$$

Where R is the diameter, f_{act} is the actuated frequency and n is the mode number. The better the left hand side matches the right hand side according relation 4.4 the better the wave can be measured by the transducer. Only natural waves were used, therefore n=0. In Figure 4.3.4 the wavelengths of the natural modes for the highest temperature (in this case 70 ˚C) gives the smallest wavelength. The diameter of the sensors used was type VS150-M) which is 12.7 mm. As can be seen in Figure 4.3.5 the optimum frequency-thickness given by equation 4.4 105 [kHz-mm] for the A_0 wave and 420 [kHz-mm] for the S_0 wave. Dividing by the thickness gives an optimum frequency of 52.5 kHz for the A_0 and 210 kHz for the S_0 wave. The optimum frequency of the S_0 wave is reasonable close to the 150 kHz of the Hanning window Also the peak frequency and frequency centroid, which were 156 kHZ and 207 kHz respectively are close to the optimum frequency. This will only affect the amplitude and perhaps the waveform recorded. However, this should not affect the wave velocity. Furthermore, for lower temperatures, the wavelength will increase and get closer to the optimum frequency.

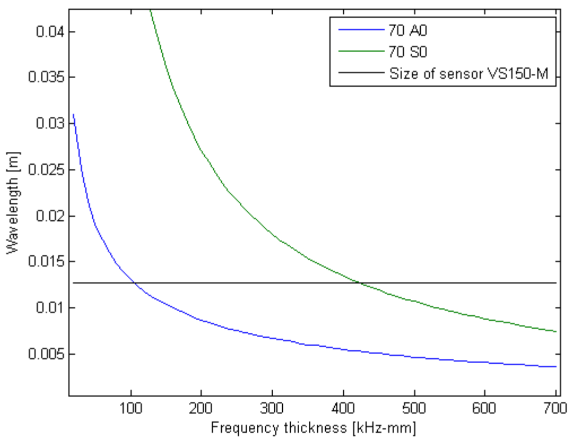

Figure 4.3.5: Wavelength versus frequency-thickness for 70 ˚C.

4.3.5 Threshold

In Section 4.2 the threshold approach with its limitations has already been discussed and the effect it has on the change of TDOA. Figure 4.3.6 shows FEM result of an actuated signal (5-cycle Hanning window, 150 kHz). The dashed blue line shows the envelope seen by a threshold of the actuated signal when changing its value from zero to one on the y-axis, while the continuous green line shows the same envelope but for a measured signal in sensor two. For convenience the dotted red line indicates the real transient recorded signal at sensor 2. For this graph the negative part is flipped to the other side resulting in 5 wavelets of increasing amplitude and the sixth wavelet having the same amplitude as the fifth (result of the symmetry of this type of signal). Most importantly the Figure shows how and why the TDOA will change when changing the threshold over the signal. Also it is seen that the actuated signal is quite well recovered in sensor 2, differences can be due to scaling and post-processing of the data. During data analysis of the signals from the FEM model the second wavelet has been selected for calculating the travel time. Figure 4.3.6 clearly indicates that a correction factor of -4.3 [µs] is required to obtain the correct travel time when selecting the average amplitude of the second wavelet as the point to compare the travel time.

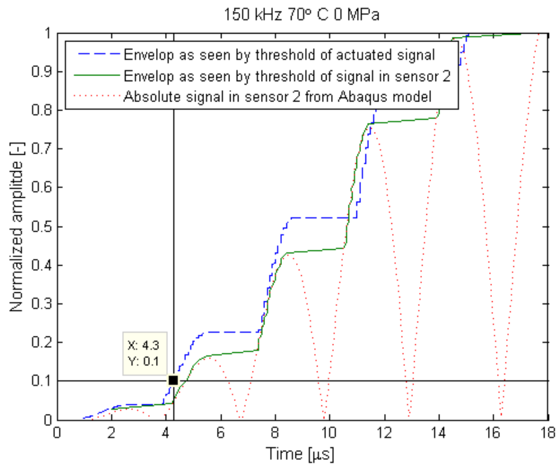

Figure 4.3.6: Visualization how the threshold in AE approach sees a signal, results obtained from FEM program, received signal in sensor 2, envelop of this signal and envelop of the actuated signal for comparison.

4.3.6 Validating FE models

The FE models have been validated by comparing the wave group velocity at room temperature (25 ˚C) to the analytical solution from the dispersion curves. The dispersion curves at room temperature have already been proven in the literature for room temperature. When the FE model matches for this temperature it is assumed to be correct. For FE model 1 the wave group velocity at 25 ˚C is 5244.8 m/s which is within 3.6% from the analytical solution (5442.1 m/s) for a 150 kHz signal. FE model 2 has a wave group velocity of 5395.1 m/s and is within 0.9% error from the analytical solution. The second FE model has closer match because the result is an average of 5 sensor paths. Both velocities match very well and therefore both models are verified with the currently used time step and element size.

Chapter 5: Results Wave Velocities and AE Localization with EOC

The experimental part of this research, as presented in Chapter 4, was divided into two stages. The first stage dealt with the changes in wave velocities as a function of temperature and load, and the second stage was focused on the location analysis using representative AE signals. This chapter is also divided into these two stages. The first Section provides the analytical, FEM and experimental results for the effect of temperature and load on the wave group velocity. The second Section provides the experimental results of AE signal localization with temperature and load. For more details of the Figures of this Chapter the reader is advised to look at larger scaled Figures in Appendix F.

5.1 Stage one, Wave velocities with Temperature and Load

This Section consists of three sub-Sections discussing the results obtained from the methodology outlined in Section 4.1. The first sub section discusses the results for the change in wave group velocities due to temperature alteration. FEM, experimental and analytical results are compared to each other. Section two shows the experimentally obtained results for the change in wave group velocities due to the effect of load. Finally, the combined effect of temperature and load on the changes in wave group velocities is discussed for the experimentally obtained results. This Section focuses on the first arrivals of the signals only, which corresponds to the S_0 wave mode.

5.1.1 Temperature effect

Figures 5.1.1a and 5.1.1b depicts the influence of temperature on the wave group velocities as measured in the range of -40 ˚C to 70 ˚C for analytical, FEM and experimental results of 150 and 300 kHz signal. Accordingly, Figures 5.1.2a and 5.1.2b depicts the influence of the temperature on the change of the wave group velocity with reference to the wave velocity measured at 70 ˚C also for a 150 and 300 kHz signal. Enlarged versions of these Figures can be found in Appendix F. The analytical curves were derived from the results presented in chapter 3 based on Dodson’s and Inman’s methodology [36]. The experimental obtained results present the average velocity of the 5 sensor paths, as is the sensor array depicts in Figure 4.1.3. By taking the average the impact of outliers is reduced, such as small changes in the material due to the rolling direction during manufacturing. The FEM results were obtained from the two FE models as outlined in Section 4.3, where for model 1 (quarter plate) each data point was obtained by running a separate FE model with the correct EOC conditions and corresponding material properties. The results of FE model 2 (which geometry matches the one in the experiments) have been averaged for the 5 sensor paths in the same way as the experiments, the experimental results have been averaged in the same way.

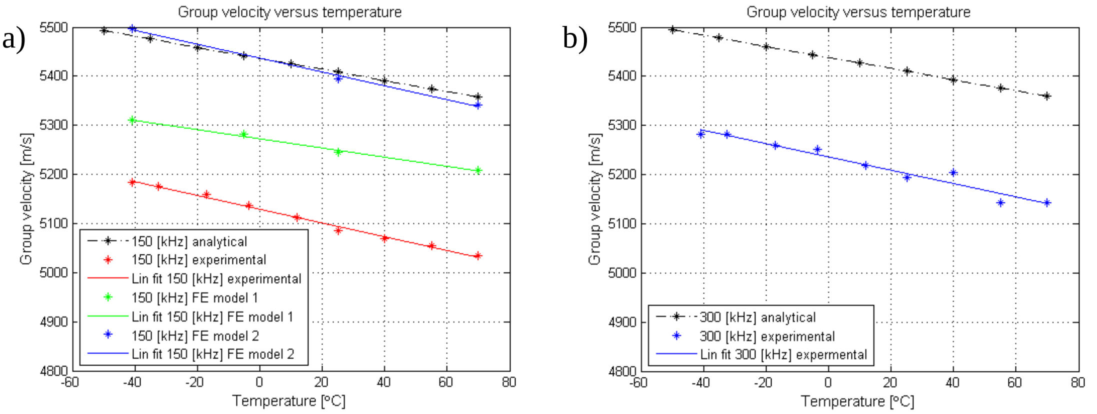

Figure 5.1.1 Wave group velocity versus temperature; a) analytical, experimental and FEM results for 150 kHz signal; b) analytical and experimental results for 300 kHz signal.

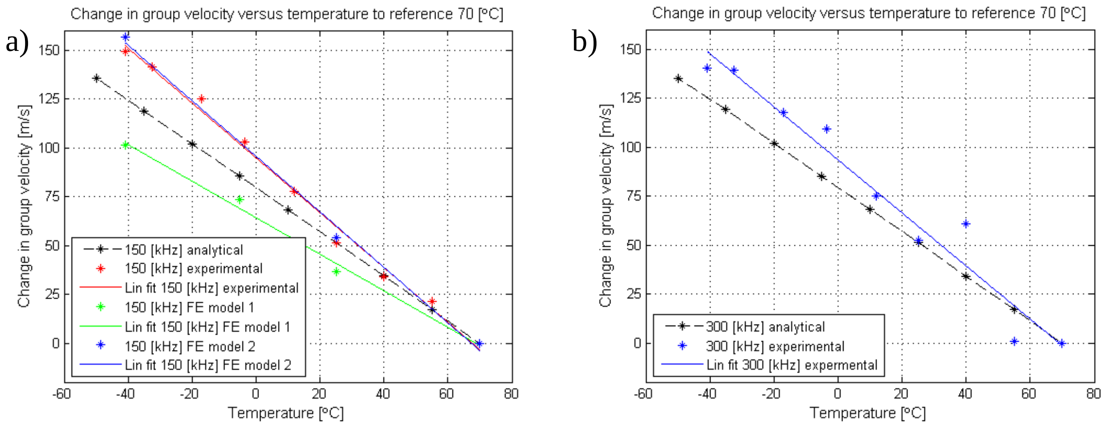

Figure 5.1.2: Change in group velocity versus temperature with reference to 70 ˚C; a) analytical, experimental and FEM results for 150 kHz signal; b) analytical and experimental results for 300 kHz signal.

The experimental, FEM and analytical results match each other very well for both the 150 and 300 kHz signal. The systematic error of the maximum absolute group velocity difference between 150 kHz experimental and 150 kHz analytical results of approximately 300 m/s is only within an error of 6% from the analytical solution. This 6% difference can be attributed to the appropriate selection of an AE threshold during the experimental phase or material differences due rolling of the aluminium during manufacturing. A low AE threshold translates into too much noise in the acquired signals, which can wrongfully influence triggering, while a high AE threshold translates into incorrect group velocity measurements because a later part of the waveform is used for triggering (as discussed in Section 4.3). The difference between the FEM and analytical results is within a maximum of 3% error and lies between the results of the experimental and analytical results. Furthermore, it is important to note that for the experimentally obtained values of 150 and 300 kHz, and the FEM results follow the same slope/trend as the analytical dispersion curves, see Figures 5.1.1 and 5.1.2. These results therefore verify Dodson's and Inman's analytical model [36]. Dodson and Inman also observed that wave speed changes due to temperature are frequency dependent. However, in the case of AE where the emitted signals are in the range of 0.1-0.45 MHz this effect is negligible. The analytical results of the 150 and 300 kHz differ 15 m/s, which is the same for each temperature step. Furthermore, also the experiments show the same behaviour where the experimental results of the Hanning window at 150 and 300 kHz signals have very small differences, shown in Figure 5.1.1a and 5.1.1b.

The results from the two FE models differ slightly. Model 1 (quarter plate) has a slightly systematic error of 150 m/s for the group velocity, also the slope of the curve is slightly below that of the experiments and the analytical results. Model 2 (full plate) can be called a perfect fit, the absolute wave group velocity matches within an error of 20 m/s, which is less than 0.005% error. The change in wave group velocity is slightly higher than the analytical results however it matches perfectly with the experimental results. These perfect results can be partly due to luck in choosing the correct threshold value for analysing the FEM results. But it is also related to selecting a part of the signal such that all signals have the same amplitude for the waveform. Small changes in both of these could lead to larger differences. The systematic error between of 150 m/s error that is visible between the FE model 1 and model 2 can be attributed to averaging the results of the 5 paths in model 2. Each sensor path gives a slightly different velocity which can be related to the boundary conditions. Averaging the 5 paths reduces the outliers, therefore results of model 2 are concluded to be better.

5.1.2 Load effect

Figures 5.1.4a and 5.1.4b illustrate the influence of the load on the wave group velocities taking into account the different sensor paths at a specific applied load case (0 through 250 MPa). The five different paths are sensors 1-2, 1-3, 1-4, 1-5 and 1-6 as shown in Figure 5.1.3. Each point in Figures 5.1.4a and 5.1.4b, consists of the change in group velocity, due to a 150 or 300 kHz Hanning window emitted from sensor one at different loads. In order to exclude the effect of temperature and only show the effect of loads, a reference to a zero load case condition at each temperature was taken. All the changes in group velocities were obtained at nine different temperatures values (from -40 to 70^{0}C). The depicted points in Figure 5.1.4a and 5.1.4b represent the average change in group velocity for all the 9 different temperatures. Figure 5.1.4a also indicates one data point of the FE model. It represents the average change in wave group velocity for three temperature (-41, 25 and 70 ^{0}C) at zero degree between sensor path and loading direction.

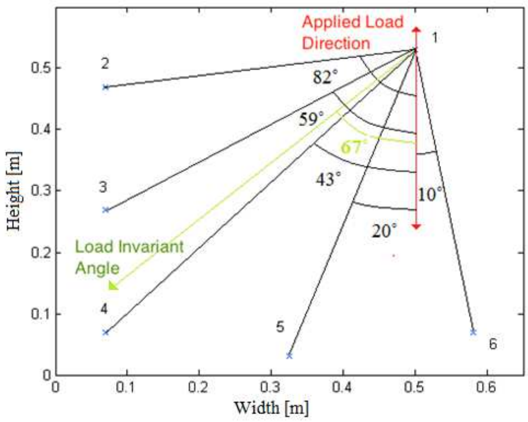

Figure 5.1.3: Schematic indicating angles of each pair with respect to applied load.

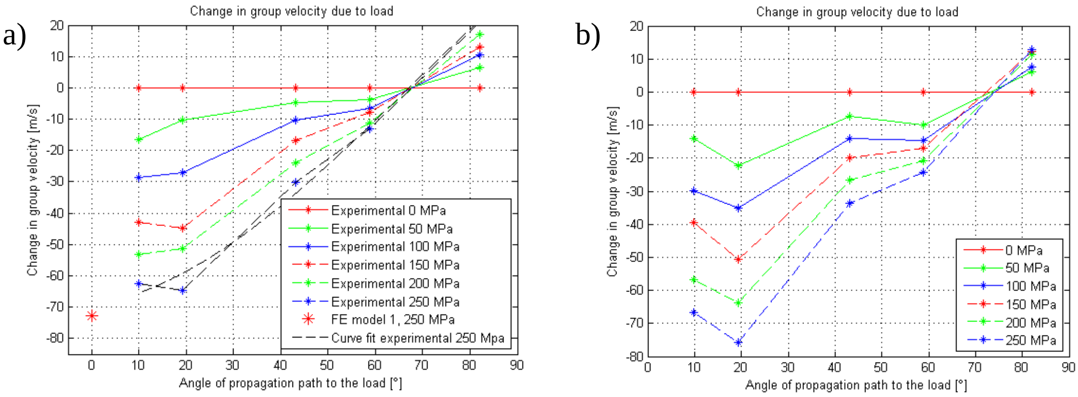

Figure 5.1.4: Experimental results of the influence of load on change of wave group velocities. a) Change in group velocity for 150 kHz signal; b) Change in group velocity for 300 kHz signal.

Figure 5.1.4a and 5.1.4b shows the change in group velocity varies linearly with load and has a sin(2α) trend, also described by Gandhi *et. al* [37], where α indicate the angle between sensor path and loading direction. Figure 5.1.4a and 5.1.4b also show a load invariant point where the wave velocity is independent of load. In Figure 5.1.4a this point occurs at 67 degree while in Figure 5.1.4b it occurs at 73 degree. However, the results in Figure 5.1.4 are slightly shifted in the vertical direction, which affects the location of this point. This shift can be attributed to an incorrect threshold correction factor as discussed in chapter 4.2. The 67-degree invariant point is in a good agreement with the analytical solution presented in Gandhi *et.al* [37] where a 63-degree load invariant angle is analytically obtained for Al-6061-T6, which is different from the 2024-T3 panel used in these experiments. The results of the FE model 1 (quarter plate, for zero degree angle) also match the experimental results, especially when looking at the curve fit.

5.1.3 Load and temperature effect

Combining the result of the previous two sections can illustrate the combined effect of temperature and load. A reference to a zero load case condition at 70 ˚C was taken to calculate the change in group velocity for the combined effect of load and temperature. Figure 5.1.5a depicts the change in group velocity for the 70 ˚C case, which is the same result as in the previous Section, indicating the effect of load on the wave group velocity. The zero load case matches the reference zero load case condition at 70 ˚C because by definition they are the same. Figure 5.1.5b illustrates the change in group velocity for the -41 ˚C case. The same zero load 70 ˚C condition has been taken as a reference velocity. This Figure shows that the curves for the effect of load shift upward by a constant value compared to the reference. This constant value equals the effect of the change in group velocity by the effect of temperature that was discussed in Section 5.1.1. For convenience the effect of temperature (from Figure 5.1.2), which is a constant change in group velocity is plotted for each corresponding temperature, which is the black dotted line in Figures 5.1.5 and 5.1.6. The black dotted line in Figure 5.1.5b matches the zero load case quite well indicating that for every angle the effect of temperature seems to be constant shift on top of the effect of load. These results indicate that the effect of temperature and load can be superimposed on each other. This observation was also analytically described by Dodson [35].

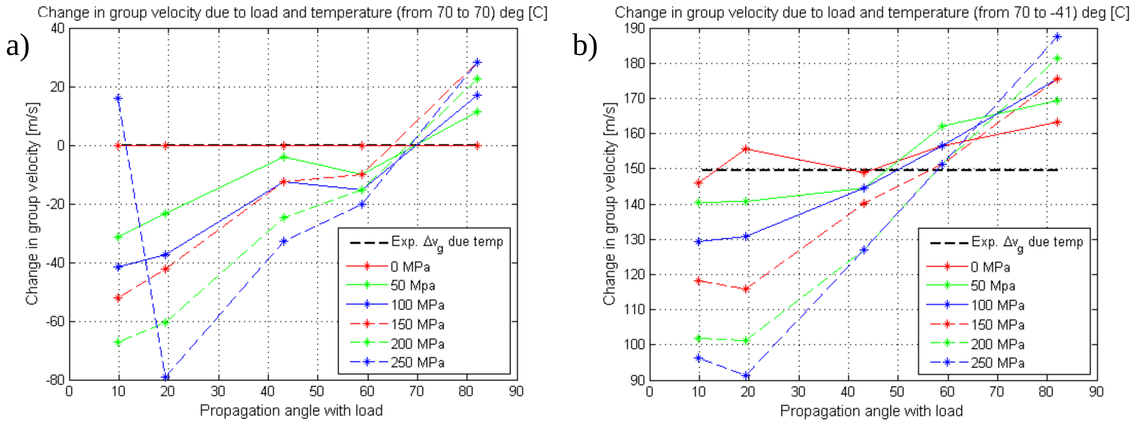

Figure 5.1.5: The influence of load and temperature on change of wave group velocities, with reference to zero load case at 70 ˚C. a) Change in group velocity at 70 ˚C; b) Change in group velocity at -41 ˚C.

The results depicted in Figures 5.1.5a and 5.1.5b also matches the expected trends from the literature very well, with few exceptions. Figure 5.1.6 shows two of those results that do not match the expected trend from the literature. In Figure 5.1.6a for a temperature of 12 ˚C every angle for which data is obtained seems to be slightly shifted in the vertical direction resulting in a very different trend than expected. Figure 5.1.6b shows that this shift of data points is not the same shift for each data point for each angle, indicating the individual data points can have their own shift. These shifts in the results can be attributed once again to an appropriate selection of a threshold correction factor.

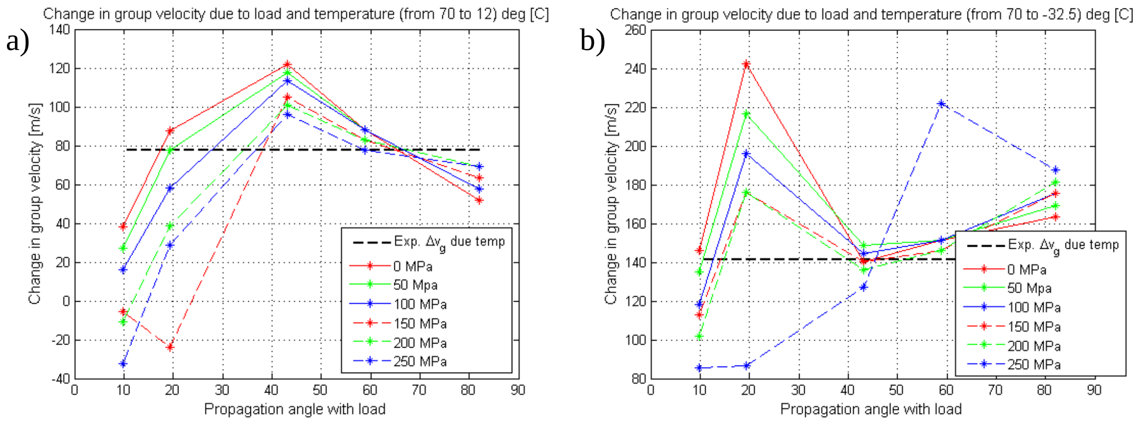

Figure 5.1.6: The influence of load and temperature on change of wave group velocities, with reference to zero load case at 70 ˚C; a) Change in group velocity at 12 ˚C; b) Change in group velocity at -32.5 ˚C.

5.2 Localization sensitivity of AE signals with temperature and load

The second stage of this study was to determine the effects of the input velocity on the ability of a location algorithm of an AE system to localize the representative AE signal (an averaged lead pencil break signal) under the influence of temperature and load. The localization module of the AE system requires a known velocity in order to locate the source of damage, as stated previously. The primary challenge of this study is that the wave speed is no longer a constant. This is due to the effect that temperature has on the material and thus on the wave speed. In addition, it is also known from section 5.1 that loads create an anisotropic behaviour on the material, which has a consequence on the wave velocity as well. As such, due to the effect of loads the wave speed varies per sensor path affecting the ability to correctly localize the damage. For this purpose a randomly selected point has been selected as the source location, which has been described in Section 4.2. Tables 5.1-5.3 highlight the results of the wave group velocities. This includes three different temperatures (-40, 25 and 70 ˚C) and three applied load levels for a Hanning window signal at 150 kHz as obtained during the experiments that have been described in section 5.1. These velocities shown in Tables 5.1-5.3 were used as inputs to the AE localization module to check the location under the given EOC. The selection of a random point as an emitting source, serves to understand the effect of the load path on the localization process when the angles with respect to the load direction between the source and the sensors are unknown. To facilitate this, three different velocities were used per pair; a minimum, average and maximum velocity as presented in Tables 5.1-5.3. These three velocities were derived from the results presented in Figures 5.1.2 and 5.1.4. The maximum and minimum velocities are obtained at a 0 and 90 degree angle. Whereas the average in Tables 5.1-5.3 is constituted of the maximum and minimum velocity for each temperature-load condition.

Table 5.1: Input wave group velocities at -41 ˚C.

Stress (MPa) @ -41 ^{0}C	Wave Group Velocity (m/s)		
	Minimum	Average	Maximum
0	-	5115,416	-
150	5072,906	5100,454	5128,001
250	5063,480	5099,298	5135,116

Table 5.2: Input wave group velocities at 25 ˚C.

Stress (MPa) @ 25 ^{0}C	Wave Group Velocity (m/s)		
	Minimum	Average	Maximum
0	-	5018,865	-
150	4976,355	5003,903	5031,450
250	4966,929	5002,747	5038,565

Table 5.3: Input wave group velocities at 70 ˚C.

Stress (MPa) @ 70 ^{0}C	Wave Group Velocity (m/s)		
	Minimum	Average	Maximum
0	-	4952,022	-
150	4909,512	4937,06	4964,607
250	4900,086	4965,904	4971,722

Figure 5.2.1a illustrates the sensors' and source's location as well as the position of the AE signal and the Hanning window as calculated from the localization module of the AE system. Furthermore, it shows the Parzen probability density function, which clusters and shows the intensity of the number of locations. Figure 5.2.1b narrows down the area to better display the calculated locations by the algorithm. The original location of the source is where the two black lines cross each other. The calculated locations were within 1 cm to the actual location of the AE source for 12 out of 21 signals, regardless of the velocity used from Tables 5.1-5.3 as input parameter. The other nine calculated locations were within an error of 32 [cm],

which is very large. The graphs indicate that two locations are even located outside the perimeter of the plate. These nine calculated location errors can be attributed to a too high threshold. This can be seen in Table 5.4 where the nine locations with a large error (indicated in bold) have TDOA values that are much larger than expected. This is an indication that the channel is triggered with the much stronger but slower A_0 wave. These results could not be improved due to the limited time available for the experiments. However, a comparison can be made with the results obtained under the same conditions with the internal pulse from the Vallen AE system. The pulse is 100 [V] signal which is much higher than the 42 [V] from the signal generator. Therefore this pulse did not have any problems with the threshold as can be seen in the location plots in Figures 5.2.2a- 5.2.2b. These Figures plot the results for internal pulse signals under the same conditions as in Figures 5.2.1a and 5.2.1b. Figures 5.2.2a and 5.2.2b indicate that for all conditions specified in Tables 5.1-5.3 the location is within 0.5 [cm] from the actual location. Concluding, despite the many effects temperature and loads have on wave speed, as described in section 5.1, the results of both the internal pulse and the AE signal indicate that these effects have little influence on the ability of an AE system to localize the source of the damage that is close to the centre of the array. However, these results can be interpreted wrongly because the TDOA used by the Vallen AE system for localization are recorded during the experiments. But they are not corrected for the part of the wave that comes before the first threshold crossing, as has been done for the TDOA measurements in Chapter 5. Therefore, the error calculated based on TDOA of these experiments can be biased by the error introduced due to the threshold selection.

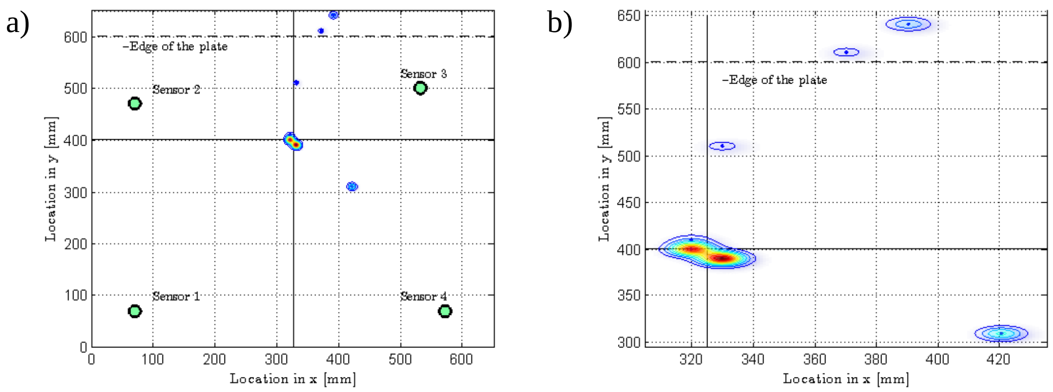

Figure 5.2.1: Locations of AE signals for multiple EOC calculated by Vallen AE system, displayed with Parzen probability density; a) sensor and calculated locations for entire plate, b) calculated locations for narrowed region.

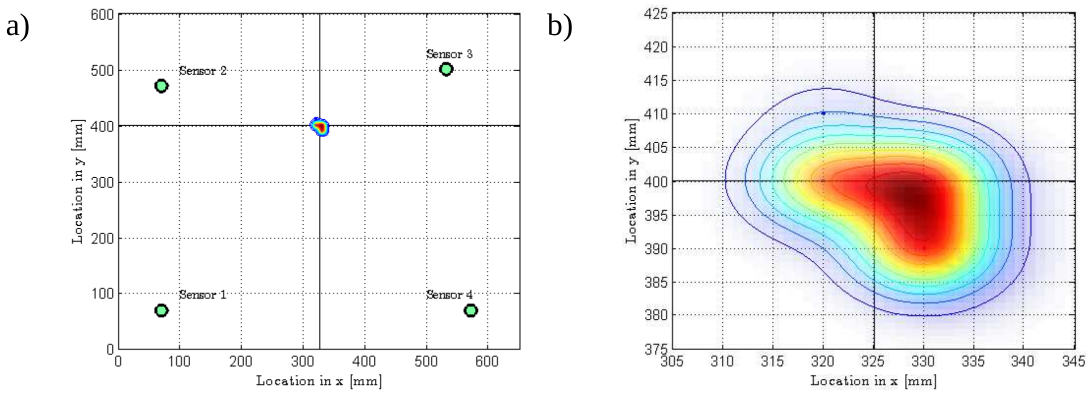

Figure 5.2.2: Locations of Vallen internal pulse signals for multiple EOC calculated by Vallen AE system, displayed with Parzen probability density; a) sensor and calculated locations for entire plate; b) calculated locations for narrowed region.

Table 5.4: EOC combinations with TDOA and locations of AE signal under these conditions, TDOA in bold are indicating TDOA from the A_0 wave.

Temp ˚C	Load MPa	V_g from table 6.1-6.3	TDOA per sensor path [µs]			AE signal	
			12	13	14	x-loc. [m]	y-loc .[m]
-40	0	average	10,2	37	38,3	0,33	0,39
	150	min	11,7	36,6	38,3	0,33	0,39
		average				0,33	0,39
		max				0,33	0,39
	250	min	11,6	36,9	38,1	0,33	0,39
		average				0,33	0,39
		max				0,33	0,39
25	0	min	**29,9**	41,2	45,6	0,37	0,39
	150	average	17,4	40,9	**96,8**	0,29	0,57
		max				0,29	0,58
		average				0,29	0,58
	250	min	17,3	41,2	**95,8**	0,29	0,57
		average				0,29	0,57
		max				0,29	0,58
70	0	min	20	39,2	n.a.	0,33	0,51
	150	average	**30,7**	37,8	n.a.	0,42	0,31
		max				0,42	0,31
		min				0,42	0,31
	250	average	**42,7**	**94,1**	**94,7**	0,39	0,64
		max				0,39	0,64
		average				0,37	0,61

Transient recordings have been obtained for all EOC described in Tables 5.1-5.3. Signal characteristics have been determined from those transient recordings. The results of the peak amplitude, peak frequency, frequency centroid, rise time and the threshold measured during the experiments can be found in Table 5.5. The table indicates that the signal characteristics are consistent under the EOC for all cases at 70 ˚C. For this temperature also the least location error has been obtained, which can be related to a low threshold that was selected. For all cases at 25 ˚C and especially at 70 ˚C the signal characteristics seem to fluctuate more, where peak frequencies and rise time seem to decrease while frequency centroids seem to increase. This fluctuation of frequencies can be partially attributed to noise introduced related to reflections mixing up with the A_0 wave. However, further investigations should be performed to conclude more about these signal characteristics under EOC.

Table 5.5: Signal characteristics of AE signals for multiple EOC.

Temperature [˚C]	Load [Mpa]	Sensor #	A_peak [mv]	Rise time [micro sec]	f_peak [kHz]	f_centroid [kHz]	Threshold [dB]
70	0	3	0,68	43,20	112,30	211,89	30,1
		2	0,68	43,20	112,30	211,89	30,1
		1	0,68	43,20	112,30	211,89	30,1
		4	0,68	43,20	112,30	211,89	30,1
	150	3	0,68	43,20	112,30	211,89	33,2
		2	0,68	43,20	112,30	211,89	33,2
		1	0,68	43,20	112,30	211,89	33,2
		4	n.a.	n.a.	n.a.	n.a.	n.a
	250	3	0,68	43,20	112,30	211,89	33,2
		2	0,68	43,20	112,30	211,89	38,1
		1	0,68	43,20	112,30	211,89	38,1
		4	0,68	43,20	112,30	211,89	38,1
25	0	3	0,41	41,10	70,80	369,70	44,1
		2	0,40	63,20	65,92	523,98	44,1
		1	0,14	20,00	68,36	306,56	44,1
		4	0,10	3,60	65,92	203,91	44,1
	150	3	0,33	45,20	70,80	148,59	44,1
		2	0,20	55,00	68,36	322,81	44,1
		1	0,13	19,80	68,36	317,31	44,1
		4	0,13	19,80	68,36	317,31	44,1
	250	3	0,45	29,80	73,24	292,70	44,1
		2	0,87	60,00	73,24	253,47	44,1
		1	0,13	23,60	70,80	193,24	44,1
		4	0,17	40,40	70,80	238,18	44,1
-40	0	3	0,67	30,20	78,13	399,33	38,1
		2	0,16	62,40	73,24	373,56	38,1
		1	0,18	22,60	75,68	297,79	38,1
		4	0,26	61,60	75,68	285,08	38,1
	150	3	0,61	30,60	78,13	335,19	38,1
		2	0,13	59,00	73,24	243,28	38,1
		1	0,24	23,98	75,68	356,22	38,1
		4	0,29	26,80	75,68	298,13	38,1
	250	3	0,61	30,60	78,13	303,78	38,1
		2	0,12	59,00	73,24	271,20	38,1
		1	0,25	23,40	75,68	345,73	38,1
		4	0,21	24,20	183,11	262,11	38,1

Chapter 6 Modelling location accuracy

In chapter 5 the effect of temperature and load on localization of AE sources was solely experimentally investigated. The results showed that despite the effects of temperature and load on wave speed it seems to have little influence on the ability of an AE system to localize the source in the centre of the array, using a single constant velocity. However, this single constant velocity can introduce more significant errors in the localization of AE sources that are not centred in the array. This chapter discusses the accuracy of a localization algorithm under changing EOC for many source locations, both inside and outside the array of sensors. The algorithm was developed in the Matlab® environment. The method and results will be described in this chapter, this includes the effects of temperature and load on localization for multiple locations. The approach of the algorithm is developed in two steps which are shown in a schematic in Figure 6.1. Firstly, the effects of temperature and load on wave velocity were modelled in a Matlab® environment resulting in TOA for a given temperature, loading, and location of sensor and source. The TOA is calculated by taking the shortest distance from the source to the sensor and dividing it by the velocity that corresponds to EOC, this is mathematically written by formula 6.1.

$$TOA_i = \frac{\sqrt{(x_s - x_L)^2 + (y_s - y_L)^2}}{v_g(T,F,\alpha)} \tag{6.1}$$

Where, (x_s,y_s) is the sensor location, (x_L,y_L) is the source location and $v_g(T,F,\alpha)$ is the group velocity affected by Temperature, Load and the angle between the sensor path and the loading direction. The AE system is based on TDOA measurements and therefore to calculate the TOA between source and all the sensors the shortest TOA is subtracted, as given by formula 6.2.

$$TDOA_i = TOA_i - TOA_1 \tag{6.2}$$

Where the $TDOA_i$, TOA_i and TOA_1 are the TDOA for all the individual sensor path's, TOA is the corresponding TOA for each sensor path and the TOA_1 is the first threshold crossing or in this case the shortest TOA.

In the second step of this algorithm, these TDOA that incorporate the effect of temperature and load were then inserted into a location algorithm (Geiger's method, which is the same method as was used in the Vallen AE system during the experiments). This program also requires an a priori determined wave group velocity. In this way the error between the original location and the calculated location can be calculated for many original locations. The localization of the source can be executed multiple times for different values of the wave group velocities to investigate which group velocity result in which kind of localization errors.

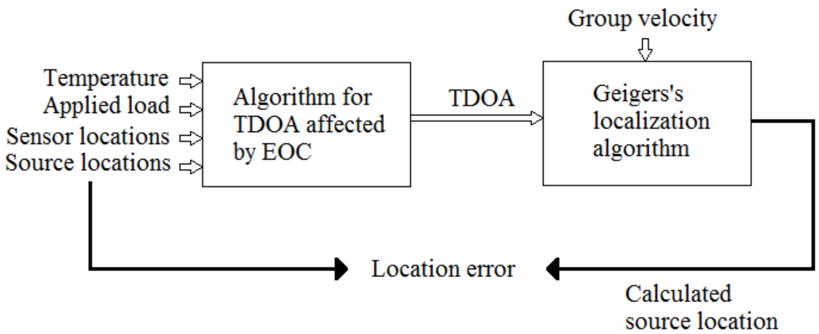

Figure 6.1: High level overview of programs information loop to calculate localization accuracy.

6.1 Wave velocity functions

To be able to calculate the TDOA that takes the effect of temperature and load into account, a wave velocity function is necessary. This relation is obtained from the experimental phase by curve fitting the results for the case of 150 kHz signals. For the temperature a linear fit (first degree polynomial) for the absolute velocity was sufficient. For the effect of temperature a sinusoidal dependent fit for the change in wave velocity of the 250 MPa case was required to describe this effect. In this way the angle dependent effect of load can be super imposed on the absolute velocity function for the effect of temperature, which mathematically is:

$$v_g = (-1.403 \cdot T + 5129) + 70.63 \cdot \sin{(0.02076 \cdot \alpha - 1.394)} \cdot \left(\frac{F}{250}\right) \quad (6.3)$$

Where T is the temperature in ˚C, α the angle between the applied load and the sensor path and F is the applied load in MPa. The curve fits can be found in Figure 6.1.1a and 6.1.1b.

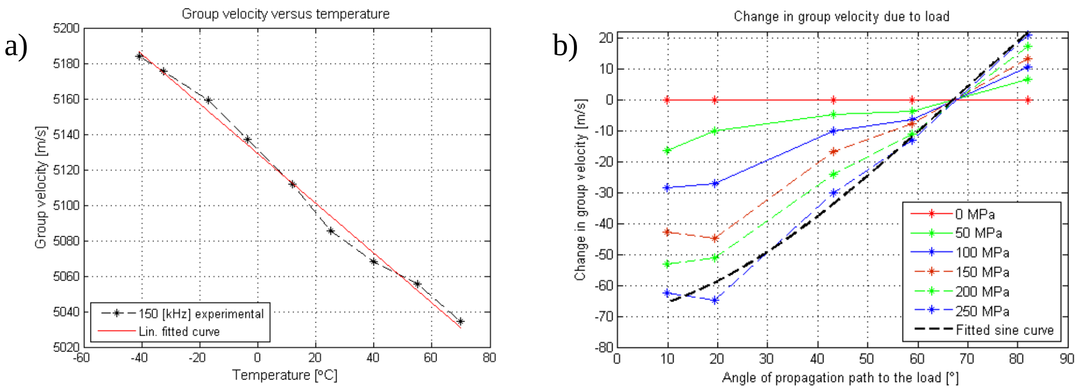

Figure 6.1.1: Experimental results for 150 kHz with curve fit for; a) effect of temperature; and b) effect of applied load.

Table 6.1 compares the TDOA for the experiments of AE signals of Section 5.2 with the calculated TDOA using formula 6.3. The results are given for all the load and temperature combinations for which experiments were done, as described in Section 5.2. Comparing the experimental results with the calculated TDOA it can be seen that the values do not fully match. It seems that one sensor path is always faster while another sensor path was consistently slower. Also, for sensor path 1-3 the TDOA seem to decrease with load during the experiments, while it is increasing when using formula 6.3. Furthermore, sensor path 1-3 and 1-4 have similar distances and angles and lead to the same TDOA by formula 6.1 but not for the experiments. All these differences may be attributed to three sources, firstly a bias in the experiments as they are not corrected for the part of the signal that comes before the threshold, secondly it may be related to the selection of a correct threshold value that has been described in Section 4.3 or thirdly, it may related to different propagation properties of AE signals compared to the Hanning windowed signals. AE signals are different from Hanning windowed signals, which is why different changes in wave velocities are possible. Further investigation should check the change of EOC on different AE signals to obtain a better insight in this. For now this investigation will continue using formula 6.3 to calculate the location from the TDOA under different EOC.

Table 6.1: Comparing TDOA of experiments versus Matlab model.

		TDOA [μs]					
		Sensor path AE experiment			Sensor path Matlab model		
Temp	Load	1-2	1-3	1-4	1-2	1-3	1-4
-40	0	10,2	37	38,3	8,95	38,38	38,38
	150	11,7	36,6	38,3	8,79	38,66	38,66
	250	11,6	36,9	38,1	8,68	38,85	38,85
25	0	**29,9**	41,2	45,6	9,11	39,07	39,07
	150	17,4	40,9	**96,8**	8,95	39,37	39,37
	250	17,3	41,2	**95,8**	8,84	39,56	36,56
70	0	20	39,2	n.a.	9,23	39,56	39,56
	150	**30,7**	37,8	n.a.	9,06	39,86	39,86
	250	**42,7**	**94,1**	**94,7**	8,94	40,07	40,07

6.2 Planar Localization Sensitivity

Once the TDOA were obtained from the previous Section they can be inserted in the localization program. This Section discusses the Geiger's localization method and will present the results of the model.

Geiger's method is an iterative algorithm for solving nonlinear problems that uses a derivative approach to update trial solutions of the location. It is the best known and most widely used source location method in seismology [66]. Location analysis uses the TDOA information in combination with an arrival time function to calculate the distance to the source. Formula 6.4 shows an arrival time function $f_i(x)$, which is expanded by a first degree Taylor polynomial around x_0, this is mathematically written as:

$$f_i(\bar{x}) = f_i\big(\bar{x}_L + \overline{\delta x}\big) = f_i(x_L) + \frac{\partial f_i}{\partial x_L}\,\delta x + \frac{\partial f_i}{\partial y_L}\,\delta y + \frac{\partial f_i}{\partial t_L}\,\delta t \qquad (6.4)$$

Where $\bar{x} = (x + y + z)^T$ represents the epicentre of the source, $\bar{x}_L = (x_L + y_L + t_L)^T$, it represents the guess or trial location of the source. $\overline{\delta x} = (\delta x_L + \delta y_L + \delta t_L)^T$ is a correction on the location where 'i' is the number of sensors. In the same way, $f_i(\bar{x})$ is the observed TDOA, $f_i(x_L)$ is the calculated TDOA and $\frac{\partial f_i}{\partial x_L}\,\delta x + \frac{\partial f_i}{\partial y_L}\,\delta y + \frac{\partial f_i}{\partial t_L}\,\delta t$ is a correction as function of the partial derivatives of the epicentre parameters. Rewriting formula 6.4 into channel residual, where $f_i(\bar{x})$-$f_i(x_L) = \bar{y}_i$ is equal to the correction factor existing from the partial derivatives, this can be written in matrix form:

$$A = \begin{bmatrix} \frac{\partial f_1}{\partial x} & \frac{\partial f_1}{\partial y} & \frac{\partial f_1}{\partial t} \\ \vdots & \vdots & \vdots \\ \frac{\partial f_i}{\partial x} & \frac{\partial f_i}{\partial y} & \frac{\partial f_i}{\partial t} \end{bmatrix} \quad \overline{\delta x} = \begin{bmatrix} \delta x \\ \delta y \\ \delta t \end{bmatrix} \quad \bar{\gamma} = \begin{bmatrix} \gamma_1 \\ \vdots \\ \gamma_i \end{bmatrix} \qquad \mathrm{A}\cdot \overline{\delta x} = \bar{\gamma} \qquad (6.5)$$

To which the least squares solution of a (over) determined system is mathematically expressed as:

$$\bar{x} = (A^T A)^{-1} A^T \bar{\gamma} \qquad (6.6)$$

The arrival time functions, which were introduced in formula 6.4 is in this case TDOA function. This arrival time function has been derived from formula 2.7 and is rewritten for this application as:

$$f_i(\bar{x}) = \frac{\sqrt{(x_i - x_L)^2 + (y_i - y_L)^2} + \sqrt{(x_1 - x_L)^2 + (y_1 - y_L)^2}}{v_{gr}} \qquad (6.7)$$

Where (x_i, y_i) are the locations of the sensors and (x_L, y_L) is the calculated location of the sensors.

The partial derivative in matrix A can be derived from formula 6.7 and they can be mathematically written as:

$$\frac{\partial f_i}{\partial x_L} = \frac{(x_1 - x_L)}{v_g\left(\sqrt{(x_1 - x_L)^2 + (y_1 - y_L)^2}\right)} - \frac{(x_{i1} - x_L)}{v_g\left(\sqrt{(x_i - x_L)^2 + (y_i - y_L)^2}\right)} \qquad (6.8)$$

$$\frac{\partial f_i}{\partial y_L} = \frac{(y_1 - y_L)}{v_g\left(\sqrt{(x_1 - x_L)^2 + (y_1 - y_L)^2}\right)} - \frac{(y_{i1} - y_L)}{v_g\left(\sqrt{(x_i - x_L)^2 + (y_i - y_L)^2}\right)} \qquad (6.9)$$

$$\frac{\partial f_i}{\partial t} = 0 \qquad (6.10)$$

The guess or trial solution $\bar{x}_L$ can be any location, however selecting a location as close as possible to the real location improves the speed and stability of the program. Therefore the centre of the array has been chosen as the initial guess location. According to Vallen Systems they also faced problems finding correct results when using a first hit sensor as the initial guess location. At the sensor a singularity occurs making it difficult to find the correct location. Several stopping criterions can be selected, in this program the stopping criterion is a self correction vector, where $\delta d = \sqrt{\delta x^2 + \delta y^2}$ and the stopping criterion is when $\delta d < \varepsilon$, where $\varepsilon = 0.1$.

Figure 6.2.1a indicates the sensor positions and all the original source locations for which the location will be calculated by the Geigers method. The range is -0.2$\leq x \leq$ 0.85 and $-0.2 \leq y \leq 0.8$ with a stepsize of 0.01 m between all the sources. In this way location errors outside the sensor array can also be calculated. The dotted line indicates the edge of the plate that was used during the experiments while the markers indicate the sensor positions. The error of the location analysis can be calculated by taking the difference between the observed location and the calculated location, mathematically this can be written as:

$$error(T,F) = \sqrt{(x_0(T,F) - x_c(T,F))^2 + (y_0(T,F) - y_c(T,F))^2} \qquad (6.11)$$

Where error(T,F) is the error for specific temperature and loading conditions, $(x_0(T,F), y_0(T,F))$ are the observed location whereas $(x_c(T,F), y_c(T,F))$ is the calculated location for conditions of temperature and load. Calculating formula 6.11 for zero load at 25 ˚C and using the correct wave velocity for the Geiger method will result in an error that is due to the accuracy of the Geiger's method. These results are plotted in Figure 6.2.1b and 6.2.2 for the same sensor array (sensor 1, 2, 4 & 6, as described in table 4.2) as used in the experiments of Section 5.2 for AE source localization. Figure 6.2.1b shows the contour of the calculated errors, whereas Figure 6.2.2 shows the 3-D plot of the same results. The two Figures indicate that the localization algorithm is very good within the enclosed area of the array. However it starts having significant location errors outside the perimeter of the plate, especially near the corners where the error can be up to 45 [cm]. Figure 6.2.1b also shows the instability of the currently used Geiger method. For example, near location (0.8, 0.4) no solutions were found because matrix A became singular. The fluctuating result in bottom left corner and top right corner of Figure 6.2.1b may be related to the initial guess position.

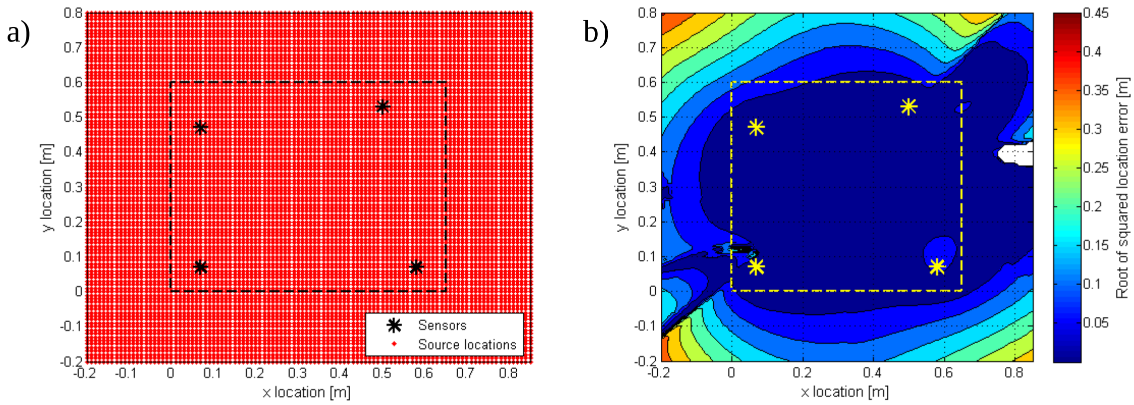

Figure 6.2.1: a) Sensor and original source location, dashed line indicate edges of plate during experiments; b) error plot of errors between original location and calculated location, for zero load, 25 ˚C and v_g= 5093 m/s.

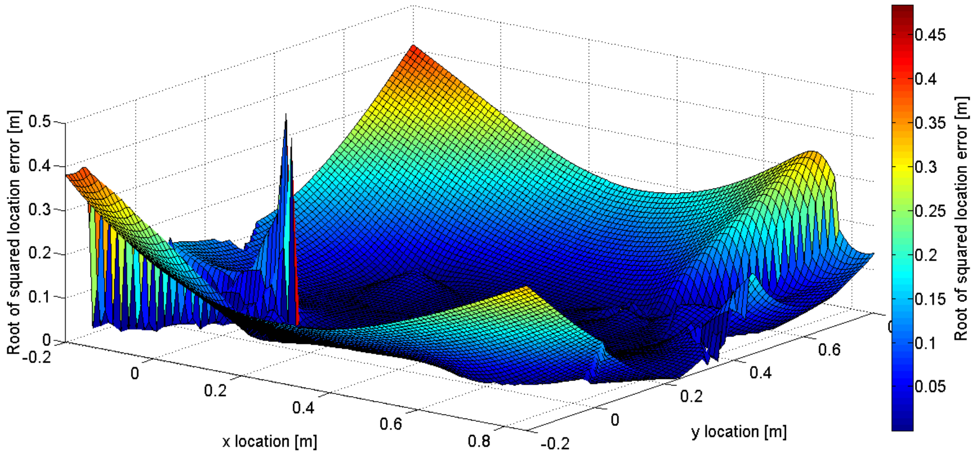

Figure 6.2.2: 3-D location error plot of errors between original location and calculated location. Error for zero load, 25 ˚C and v_g= 5093 m/s.

To calculate the effect of changing wave velocities on the capability to localize damage comparative errors should be calculated. These errors are the difference between the normal case (25 ˚C, 0 MPa) and other conditions, this is mathematically written as:

$$error(\Delta T, \Delta F) = \sqrt{(error(T,F)^2 - (error(25,0))^2} \quad (6.12)$$

For all of the locations indicated in Figure 6.2.1a this comparative error has been calculated for three conditions. These three conditions are; firstly, 25 ˚C with 250 MPa (so only effect of changing load); secondly, -41 ˚C with 250 MPa (maximum negative temperature with maximum applied load); and thirdly, 70 ˚C with 250 MPa (maximum positive temperature with maximum applied load). Where ‘maximum’ means the maximum temperature or load considered in this study. For each of these EOC combinations a different velocity profile describes the changing wave velocity to an angle with respect to the load. These velocity profiles can be found in Figure 6.2.3, an extra condition for 25 ˚C with no applied load is added because this is the case to which the errors are compared to.

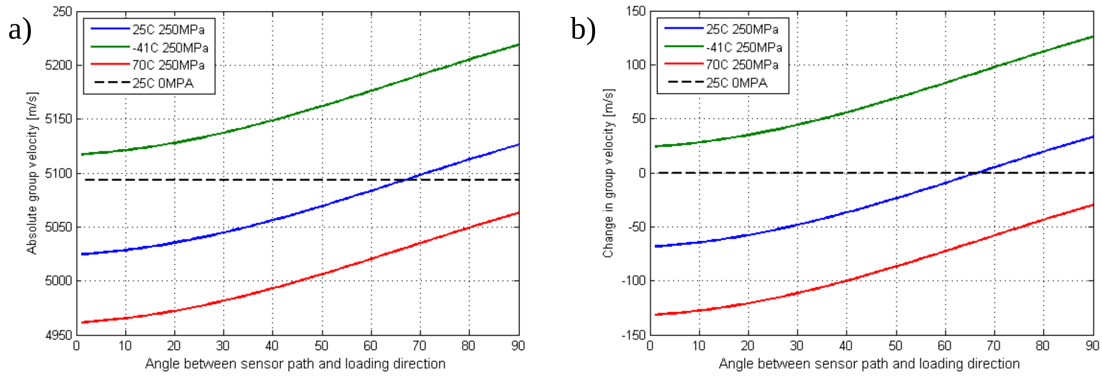

Figure 6.2.3: Velocity profiles for four temperature load combinations; a) absolute group velocity profiles; b) Change in group velocity to reference wave velocity for the condition of 25 ˚C with 0 MPa.

6.2.1 Comparative error between 25 ˚C, 0 MPa to 25 ˚C, 250 MPa

Figures 6.2.4a-b depict the comparative error between 25 ˚C with 250 MPa load and 25 ˚C with 0 MPa load. Both high resolution and low resolution contours are plotted, the resolution is 0.0005 m and 0.005 m between isocontours, respectively. These Figures indicates the location error due to changing wave velocity by applying 250 MPa static load. The comparative errors due to applied load, which are in the range of 0-2 [cm], are much smaller than the general location algorithm errors of Geiger's method in Figure 6.2.1b. More importantly, they indicate (especially the low resolution contour) that lighter areas appear at the middle of top and bottom of the graph. This indicates that larger errors happen at those locations, which can be explained with the velocity profile in Figure 6.2.3. Where the largest velocity difference between the blue line and dotted line (which compares the same conditions as in Figure 6.2.4) is at small angles between the sensor path and loading direction, this corresponds with the lighter locations in Figure 6.2.4.

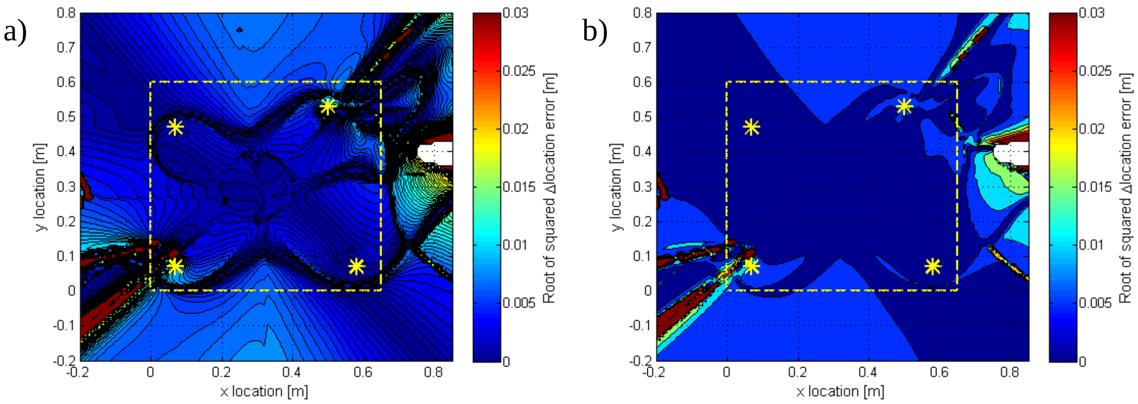

Figure 6.2.4: Comparative error for 25 ˚C with 250 MPa load; a) high resolution contour; b) low resolution contour.

6.2.2 Comparative error between 25 ˚C, 0 MPa to 70 ˚C, 250 MPa

Figures 6.2.5a-b depict the low and high resolution contour of the comparative error between 70 ˚C with 250 MPa applied load and 25 ˚C with 0 MPa. The same resolution as in Figure 6.2.4a-b is maintained. These Figures indicate the location error due to changing wave velocity by applying 250 MPa static load and an increase in temperature of 35 ˚C. These Figures show the same results as in Figures 6.2.4a-b but with slight elevated errors. This can be explained according to Figure 6.2.3 where the velocity curve for 70 ˚C with 250 MPa has shifted to lower velocities creating a larger change in velocities with the 25 ˚C with 250 MPa. Furthermore, the red areas at the bottom left and top right indicate larger errors. These effects can be attributed to a singularity related to the mathematics of the sensor positions and initial conditions of this problem, this is also visible in Figure 6.2.1b.

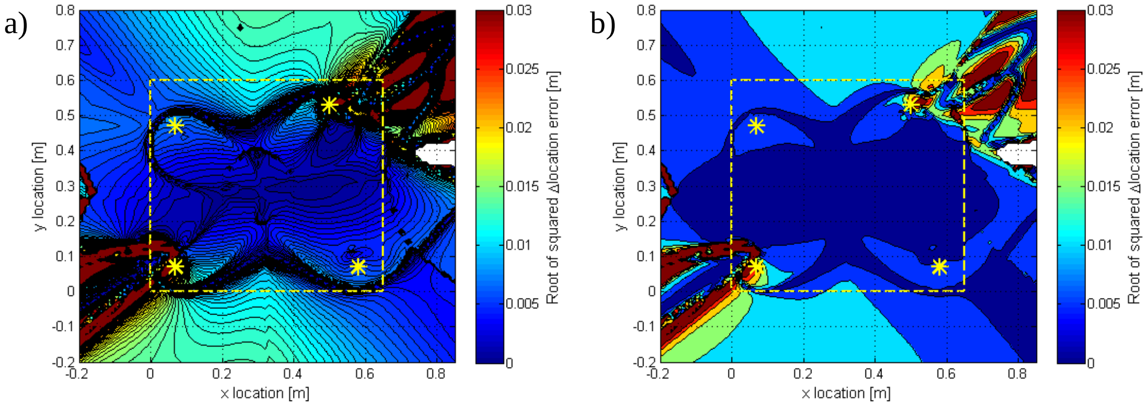

Figure 6.2.5: Comparative error for 70 ˚C with 250 MPa load; a) high resolution contour; b) low resolution contour.

6.2.3 Comparative error between 25 ˚C, 0 MPa to -41 ˚C, 250 MPa

Figures 6.2.6a and 6.2.6b depict the low and high resolution contour of the comparative error between -41 ˚C with 250 MPa applied load and 25 ˚C with 0 MPa. The same resolution as in Figure 6.2.4a-b is maintained. These Figures indicate the location error due to changing wave velocity by applying 250 MPa static load and a decrease in temperature of 66 ˚C. These Figures show a very different result compared to the previous Figures. The highest comparative errors can be found to the middle left and right edge of the Figure. Once again these results can be explained with Figure 6.2.3. The decrease in temperature results in an increase in group velocity that shift the change in group velocity curve upward. This results in a velocity profile that has the largest difference in group velocity at the 90 degree angle between sensor path and loading direction, this corresponds with the lighter locations in Figure 6.2.6.

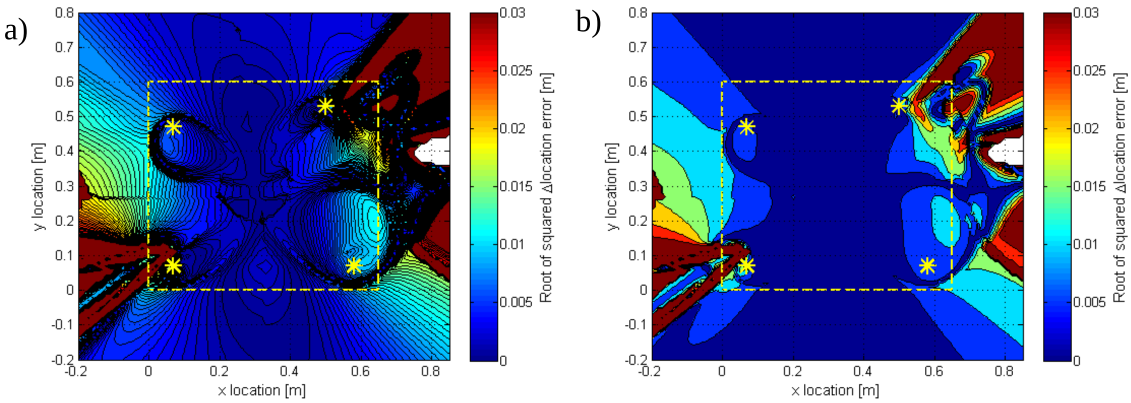

Figure 6.2.6: Comparative error for -41˚C with 250 MPa load; a) high resolution contour; b) low resolution contour.

At the end of Section 5.2 it was concluded that despite the many effects of temperature and loads on wave speed, the results indicate that these effects have little influence on the ability of an AE system to localize the source of the damage. This conclusion is also supported in this Chapter. Furthermore, it was also shown that this conclusion is applicable to the entire area enclosed by the current sensor positions. Where the errors due to the effects of temperature and load within the enclosed area of the sensor do not go beyond 1 [cm] of the actual location. Moreover, the combination of temperature and load affects for which areas in or outside the array area Geiger’s method have a reduced localization capability, and as such, are more affected by the changing wave velocity. This effect is related to angle dependent effects of the load in combination with a change in temperature. When load is applied and the temperature is increased then the largest change in wave velocities occur for small angles between the sensor path and the loading direction. For locations where most sensors have small angles between the path of the calculated source location to the sensors and the loading direction will see a reduced location capability. On the other hand when the temperature is decreased the wave velocity increases, which then results in the largest change of wave velocity near 90 degree between the sensor path and the loading direction. Other combination of temperature and load can lead to results that are in between the two cases just discussed. This is because these two cases are the most extreme cases expected to occur in an operational environment.

The location algorithm can be further improved by finding the optimal initial conditions and a better stopping criterion. This can help to reduce possible errors and making it possible to better calculate source locations. Also better location algorithms can be developed, but in the case they use a single velocity for localization, then the effects described in this chapter will occur.

The results in this Chapter show the effects of temperature and load in one sensor array regarding the capability to localize damage with and AE approach. When the distance between the sensors is increased the localization error introduced due to temperature or load will increase as well. It may be possible to generalize the conclusions of this chapter to the case of the active approach. The velocity function of formula 6.1 that takes effects of temperature and load into account is obtained with experimental results that use a Hanning windowed signal, which is also used in the active approach. Therefore, similar location errors with EOC can be expected in the active approach. However, the arrival time function 6.5 will be different for the active approach, resulting in different derivatives which may affect the accuracy.

Chapter 7 Discussion, Conclusions and Recommendations

The aerospace industry addresses an increasing demand for lower operational and maintenance cost by pointing to SHM strategies that can assess the structural integrity in service. Aircraft structures operate under variable EOC. However, these EOC are one of the main obstacles for deploying SHM methods for in service real time monitoring. Furthermore, passive approaches such as AE show promising results for localizing damage in complex structures. But investigation of the effects of EOC is very limited. Therefore the goal of this thesis was to understand: *how and to what extent load and temperature affect AE signals and damage localization in a simple metal plate structure and to assess this technique for real time monitoring of aircraft structures in an operational service environment.*

In order to address the aforementioned question, this study consisted of a literature study and two stages. In stage 1 the change in wave velocity with varying EOC was investigated whereas in stage 2 the effect of the change in wave velocity on the ability to localize damage was investigated. A literature study was performed on the theories that investigated the effect of temperature and load on wave velocities. Focus was given on Dodson and Inman theory on the effect of homogenous temperature change on the dispersion curves. That theory had a temperature dependent stress strain constitutive equation and took into account alteration of material properties with temperature. However, the proposed model wasn't verified through experiments. Michaels *et al.*, developed a model for the effect of load, but they experimentally investigated the signal change coefficients for the A_0 wave only. They pointed out that load makes material's elastic behaviour directionally dependent and therefore change of the wave velocity was angle dependent also. The combined effect of temperature and load was not investigated in depth. Dodson combined an analytical theory that superimposed the effects of temperature and load, however this was not investigated experimentally either.

In the first stage of this study, changes in wave velocity due to temperature and load were investigated. Firstly, the mathematical analytical model from Dodson & Inman was re-produced. This model indicated that changes with temperature were most significantly affected due to changes of the density and stiffness of the structure with temperature. Additionally, the model showed that changes in wave speeds for S_0 wave mode contains temperature invariant points. Further investigation into these invariant points showed that the change in wave group velocity with temperature was zero however, the second derivative was not and shifted these points slightly over frequency thickness with temperature.

In order to evaluate the analytical model, an aluminium 2024-T4 was selected to be tested. Furthermore the results of the analytical model were also compared to FE results. Experimental results were obtained for Hanning windowed signals with peak frequency of 150 kHz and 300 kHz for a temperature range of -41 ˚C in nine steps to 70 ˚C. Additionally, Abaqus/CAE® FEM results were obtained for a Hanning window of 150 kHz. Results showed an increase in temperature resulted in a decrease of the wave group velocity and vice versa. However, near the temperature invariant points this behaviour tends to inverse but changes in wave group velocity are relatively small in this frequency thickness range. The maximum difference of the absolute wave speed between experimental results and analytical solution was 6%. This 6% difference can be attributed to the appropriate selection of an AE threshold during the experimental phase. The difference between the FE and analytical results was within an error of 3 and 1% for FE model 1 and 2, respectively. Furthermore, the values lies between the experimental and analytical results. The frequency dependent effect of temperature on the group velocity for AE signals, which were in the range of 0.1-0.45 MHz, was negligible. The experimental, FE and analytical results matched each other well, accounting the effect of temperature. Therefore these experimentally and FEM results verified the analytical theory of Dodson and Inman, extending results for both positive and negative temperatures.

Additional experiments investigated the effect of load and combined load and temperature on the changes in wave group velocity for a 150 and 300 kHz Hanning window. At each temperature level, six different static loads were applied that ranged from 0 MPa to 250 MPa in increments of 50 MPa. Results showed that the change in group velocity varies linearly with the load and contains a sinusoidal behaviour with the angle between the sensor path and loading direction. Which meant that the wave group velocity decreased for small angles, increased for large angles and varied with a sinusoidal behaviour for the other angles between the propagation path and the loading direction. Furthermore, a load invariant point at 67 degree was measured. The 67-degree invariant point was in a good agreement with the analytical solution presented by Gandhi *et.al* [37] where a 63-degree load invariant point was analytically obtained for Al-6061-T6 plate. The results of the combined effect of temperature and load indicated that they were superimposed on each other. The experimental results also presented problems with threshold selection during the experiments. A low AE threshold could translate into too much noise in the acquired signals, which can result in wrongfully triggering, while a high AE threshold could translate into incorrect group velocity measurements because a later part of the waveform would be used for triggering. The threshold also did not compensate for the part of the signal that came before the trigger, which could elongate the TDOA measurements.

The second stage of this study investigated how the effect of the change in wave group velocity under varying EOC will affect the capability to localize the damage. For this purpose a representative AE signal was obtained through pencil lead breaks and excited on one random location within the area of the array. It was found that for AE signals under varying EOC the localization accuracy was within 1cm for 12 out 21 cases (57%) and 100% of the cases studied for which the source was an internal pulse. The low percentage of correct locations with AE signal can be attributed to the strength of the signal. The actuated AE signal was 42 V_{pp} while the internal pulse was $100V_{pp}$.

The accuracy of the location capability under EOC from the experiments was also supported with results from a Matlab® model. The model calculated the effect of temperature and load on the TDOA by using a relation developed from curve fits obtained with the experimental results for changes in wave group velocities. Then, a location algorithm (Geiger's Method) was used to calculate errors between original and calculated location for different conditions. In this way the location capability under influence of temperature and load was assessed for many locations. It showed that errors due to the effects of temperature and load within the enclosed area of the sensor didn't exceed a circle with 1.5 cm radius of the actual location for an array size of 65 by 60 cm. Furthermore, the combination of temperature and load affects which angles between the sensor paths and the loading direction have the largest change in group velocity. This will result that some areas will have a larger reduction in localization accuracy due to EOC. This effect was related to the angle dependent effect of the load; for locations where the angles between the sensor paths of most sensors to the loading direction corresponded to the largest change in wave group velocity due to both temperature and load would result in larger differences between the actual and calculated location.

The experimental and numerical results of stage two were obtained for the effects of temperature and load in one sensor array. The small reduction in localization capability with varying EOC can perhaps be more significantly affected in larger arrays. It may be possible to generalize these results to the active SHM approach. The velocity function takes effects of temperature and loads into account, which was verified with experimental results that used a Hanning windowed signal. Therefore similar location errors with EOC can be expected in the active approach.

This study demonstrated that even though changes in group velocity due to EOC can be in the order of 260 m/s these effects had very little consequence on the ability of an AE system to localize the damage, thus providing an accurate location of the source. Therefore, the AE SHM technique performed well under EOC making it a suitable technology for real time monitoring of aircraft structures in an operational service environment. However, this also indicated the importance of an threshold independent trigger mechanism for AE signal detection. Real AE signals are expected to be less strong than the signal used during this thesis and in this study already many difficulties were faced with the threshold trigger mechanism.

The main conclusions of the thesis can be summarized as follows:

- Verified Dodson & Inman analytical theory both experimentally and by FE method, where impact of stiffness and density have largest influence on changes in wave group velocity for normal operating temperature range.

- Experimental results indicated angle dependent velocity profile with load, and loading invariant angle at 67 degrees verifying analytical results from Ghandi *et al.* Furthermore, experimental results indicated that changes in wave group velocity due to temperature and load were superimposed. However further FE modelling should still be provided.

- Experimental and FEM results indicated that the changes in wave group velocities of AE signals did not affect localization capability significantly. However, the angle dependent velocity profile affected which areas have a reduced localization capability under varying EOC.

The investigation in this thesis that combined the effect of temperature and load on the AE approach for SHM purposes, revealed changes in wave velocity due to temperature and load inducing small changes in localization capability for a plate of 65 by 60 cm. The effect of temperature and load can become more significant in larger arrays. Therefore, this rises recommendations for further research:

- Investigate a threshold independent trigger mechanism. The amplitudes of real AE signals are lower than the AE signals used in this research and many difficulties already were faced in obtaining the correct TDOA.
- Further FE modelling should verify the experimental results for the effect of load on the change in wave group velocity and the combined effect of temperature and load on the wave group velocity.

- During experimental tests with representative AE signals it is advised to use a signal generator that can amplify signals to 100 [V_{pp}] signals.

- The location algorithm can be further improved by finding the optimum initial conditions and a improving the stopping criterion of the iterative method.

- Investigate the effect of temperature and load in composite plates or more complex structures.

- Use of large distances between sensors to obtain more accurately the change in TDOA.

Bibliography

[1] W. Stazewski, C. Boller and G. Tomlinson, health monitoring of aerospace structures, ISBN: 0470843403: Wiley, 2004.

[2] A. Raghavan and C. E. Cesnik, “Review of Guided-wave Structural Health Monitoring,” *The Shock and Vibrations Digest,* pp. 91-114, 2007a.

[3] H. Sohn, “Effects of environmental and operational variability on structural health monitoring,” *Philosophical transaction of the royal society,* pp. 539-560, 2007.

[4] B. Lee, G. Manson and W. Staszewski, “Environmental effects on lamb wave responses from piezoceramic sensors,” *Material Science Forum,* 2003.

[5] D. Gagar, M. Martinez, M. Yanishevski, B. Rocha, J. McFeat, P. Foote and P. Irving, Detecting and Locating Fatigue Cracks in a Complex Wing-box Structures Using the Acoustic Emission Technique: a Verification Study, Stanford, CA: DEStech Publication, Inc., 2013.

[6] W. Ostachowicz, P. Kudela, M. Krawczuk and A. Zak, “Guided Waves in Structures for SHM, The Time-Domain Spectral Element Method,” Wiley, 2012, pp. 233-235.

[7] ASTM International, *ASTM E976 Standard Guide fro Determining the Reproducibility of Acoustic EmissionSensor Response,* ASTM International.

[8] Dassault Systems, “Abaqus/CAE,” [Online]. Available: http://www.3ds.com/products-services/simulia/portfolio/abaqus/abaqus-portfolio/abaquscae/. [Accessed 27 4 2014].

[9] D. O. Gagar, “PhD dissertation: Validation and Verification of the Acoustic Emission Technique for Structural Health Monitoring,” Cranfield Univerity, Cranfield, 2012.

[10] J. Homan, “Aircraft Structural Integrity & Maintenance,” Delft University of Technology, Delft, 2008.

[11] H. Kinnision, Aviation Management Maintenance, McGraw-Hill, 2004.

[12] M. Boon, D. Zarouchas, M. Martinez, D. Gagar, R. Benedictus and P. Foote, “Temperature and Load effects on Acoustic Emission Signals For Structural health Monitoring Apllications,” in *EWSH-2014,* Nantes, 2014.

[13] SAE international, “Guidelines for Implementation of Structural Health Monitoring on Fixed Wing Aircraft.,” SAE international, 19 09 2013. [Online]. Available: http://standards.sae.org/arp6461/. [Accessed 17 02 2014].

[14] A. Croxford, P. Wilcox, B. Drinkwater and G. Konstantinidis, “Strategies for guided-wave structural health monitoring,” *The royal Society,* pp. 2961-2981, 2007.

[15] D. Baranzanchy, “Numerical Simulation and Experimental Verification of Lamb waves for Structural Health Monitoring Applications,” Delft, 2013.

[16] A. Rajagopal, “Structural Health Monitoring using Lamb Waves, bachelor thesis,” Indian Institute of Technology, Bombai, 2008.

[17] S. S. Kessler, S. M. Spearring and J. A. Mauro, “In-Sity Damage Detection of Comoposites Strutures using Lamb Wave Methods,” in *EWSHM,* , 2002.

[18] D. Egle, “Wave Propagation,” in *Non Destructive Testing,* 2nd edition ed., 1987.

[19] ISO, “ISO, International Organization for Standardization,” 2001. [Online]. Available: http://www.iso.org/iso/home.html. [Accessed 23 10 2013].

[20] C. Grosse and M. Ohtsu, Acoustic emission testing ISBN: 978-3-540-69895-1, Springer, 2007.

[21] C. Scala and S. Couslnad, “Acoustic emission during fatigue crack propagation in the aluminium alloys 2024 and 2124,” *Materials Science and Engineering, vol 61,* pp. 211-218, 1983.

[22] C. Scruby, G. Baldwin and K. Stacey, “Characterisation of fatigue crack extension by quantitative acoustic emission,” *International Journal of Fracture, vol 28,* pp. 201-222, 1985.

[23] D. Gagar, P. Irving, P. Foote and J. Mcfeat, “Investigation of AE Geneation from Fatigue Cracks for Structural Health Monitoring in 2014 Alimunium Alloy,” in *6tn European workshop on structural health monitoring*.

[24] D. Zarouchas, “Experimental and numerical of wind turbine blade sub components,” Vrije Universiteit Brussel, 2012.

[25] M. L. Thompson, “On the Material Properties and Constitutive Equations of, PhD dissertation,” Drexel university, 2002.

[26] M. Martinez, *Finite Element Model of Structures with Piezoelectric Elements,* Ontario: Ottowa-Carleton Institute for Mechanical and Aerospace Engineering, 2006.

[27] V. Giurgiutiu, “Structural Healt Monitoring with Piezoelectric Waver Active Sensors, PhD dissertation,” Elsevier, 2008.

[28] A. Erturk and D. J. Inman, “Piezoelectric Energy Harvesting,” in *Piezoelectric Energy Harvesting,* Wiley, 2011, p. Appendix A.

[29] Physical Properties of Chrystals: Their Representations by Tensors and Matrices, Oxford: Oxford University Press, 1957.

[30] A. Raghavan and C. E. Cesnik, “Studies on effects of elevated temperature for guided-wave structural health monitoring,” *Sensors and Smart Structures Technologies for Civil, Mechanical, and Aerospace Systems,* 2007b.

[31] H. Lamb, “On waves in An Elastic Plate,” *Royal Soiety of London,* pp. 93(651): 804-824, 1917.

[32] J. Sharma, D. Singh and R. Kumar, “Generalized thermoelastic waves in homogenous isotrpic plates,” *The Journal of the Acoustical Society of America,* pp. 108: 848-851, 2000.

[33] G. Konstantinidis, B. Drinkwater and P. Wilcox, “The temperature stability of guided wave structural health monitoring systems,” *Smart Materials and Structures,* pp. 15: 967-976, 2006.

[34] N. Gandhi and J. E. Michaels, “Efficient Pertubation Analysis of Lamb wave dispersion curves,” *AIP,* 2010.

[35] J. C. Dodson, Guided Wave Structural Health Monitoring with Environmental Considerations, Blacksbirg, Virginia: , 2012.

[36] J. Dodson and D. Inman, “Thermal sensitivity of Lamb waves for structural health monitoring applications,” *Ultrasonics,* pp. 677-685, 2013.

[37] N. Gandhi, J. E. Michaels and S. J. Lee, “Acoustoelastic Lamb wave propagation in biaxially stressed plate,” *Journal Acoustical Society America,* pp. 1284-1293, 2012.

[38] N. Gandhi, J. E. Michaels and S. J. Lee, “Acoustoelastic Lamb Wave Propagation in a Homogenous, Isotropic Aluminium Plate,” in *Review of Prgress in Quantitative Nondestructuve Evaluation*, 2011.

[39] J. E. Michaels, S. J. Lee and T. E. Michaels, “Impact of applied loads on guided wave structural health monitoring,” 2011.

[40] N. Gandhi and J. E. Michaels, “Efficient pertubation analysis of lamb wave dispersion curves,” in *AIP*, 2010.

[41] S. J. Lee, N. Gandhi, J. E. Michaels and T. E. Michaels, “Comparison of the effects of applied loads and temperature variations on guided wave propagation,” 2011.

[42] F. Song, G. Huang and G. Hu, “Couples piezo-elastodynamic modeling of guided wave excitation and propagation in plates with applied pre stresses,” *Journal of Intelligent material Systems and Structures*, pp. 598-611, 2012.

[43] F. Shi, J. E. Michaels and S. J. Lee, “In situ estimatioin of applied biaxial loads with lamb waves,” *Journal of acoustical Society of America*, pp. 677-687, 2012.

[44] M. Lowe, P. Crawley, J.-Y. Kao and O. Diligent, “The low frequency reflection characteristics of the fundamental antisymmetric Lamb wave a0 from a rectangular notch in a plate,” *Journal of the Acoustical Society Americe*, pp. 112: 2612-2622, 2002.

[45] A. J. Croxford, P. D. Wilcox, G. Konstantinidis and B. W. Drinkwater, “Strategies for Overcoming the Effect of Temperature on Guided Wave Structural Health Monitoring,” *Health Monitoring of Structural and Biological Systems*, 2007.

[46] J. B. Harley and J. F. Moura, “Scale Transform Signal Processing for Optimal Ultrasonic Temperature Compensation,” *IEEE*, 2012.

[47] P. Wilcox, A. Croxford, J. Michaels, Y. Lu and B. Drinkwater, “A comparison of temperature compensation methods for guided wave structural health monitoring,” *Review of quantitiative Nondestructive Evaluation*, pp. 27: 1435-1460, 2008.

[48] A. J. Croxford, J. Moll, P. D. Wilcox and J. E. Michaels, “Efficient temperature compensation strategies for guided wave structural health monitoring,” *Ultrasonics*, pp. 50: 517-528, 2010.

[49] J. Moll, R. Schulte, B. Hartmann, C.-P. Fritzen and O. Nelles, “Multi-site damage localization in anisotrpoic plate-like structures using an active guided wave structural health monitoring system,” *Smart Materials and Structures*, 2010.

[50] S. Ziola, “Source location in this plates using cross correlation,” Monterey, California, 1992.

[51] J. L. Spiesberger, “Hyperbolic location errors dye to insufficient numbers of receivers,” *Journal of Acoustical Society America*, vol. vol 109, no. 6, 2001.

[52] R. Ernst and J. Dual, “Acoustic emission localization in beams based on time reversed dispersion,” *Ultrasonics, Elsevier*, vol. 2014, p. 12, 2014.

[53] J. Ignaczak and M. ostoja-Strazewski, “Thermoelasticity with Finite Wave Speeds,” New York, Oxford University Press, 2009.

[54] Matweb, “Aerospace Specification Metals Inc.,” [Online]. Available: www.asm.matweb.com/search?specificMaterial.asp?bassnum=MA2024T4. [Accessed 25 02 2014].

[55] MIL Handbook-5H, Military handbook, Department of Defense, United States, 1998.

[56] ASM Handbook, ASM Handbook, 1992.

[57] M. Lalpoor, D. Eskin and L. Katgerman, Metallurgical and Materials Transactions A, v40A, p3304, Springer, 2009.

[58] T. Beumler, “Flying glare, PhD dissertation,” in *A contribution to aircraft certification issues on strength properties in non-damaged and fatigue damaged glare structures*, Delft, Delft University of Technology, 2004.

[59] V. Syteme, “Vallen Syteme,” [Online]. Available: http://www.vallen.de/. [Accessed 21 05 2014].

[60] Ursa Uralite, “Ursa Uralite,” [Online]. Available: http://www.ursa.be/nl-nl/Documents/documents/xps-n-w-e.pdf. [Accessed 21 05 2014].

[61] M. Ge, “Analysis of source location algorithms, part 1: overview and non-iterative methods,” *J. Acoustic Emission,* no. 21, p. 15, 2003.

[62] sensortech, *Piezoelectric Material constants for Compliance Matrix,* http://www.sensortech.ca/site/content/2006-01.pdf.

[63] F. Moser, L. Jacobs and J. Qu, “Modeling elastic wave propagation in waveguides with the finite element method,” *NDT&E Int,* pp. 32: 225-234, 1666.

[64] L. Chen, Y. Dong, Q. Meng and W. Liang, “FEm simulation for Lamb Wave evaluate the defects of plates,” *Microwave and Millimeter Wave Circuits and System Technology (MMWCST),* 2012.

[65] I. Viktorov, Rayleigh and Lamb waves, New York: Plennum Press, 1967.

[66] M. Ge, “Analysis of source Location Algorithms, part II: iterative methods,” *Journal of Acoustic Emission,* vol. 2003, pp. 29-51, 2003.

[67] J. Nye, “Physical Properties of crystals,” in *Physical Properties of crystals,* Oxford, Clarendon press, 1957, pp. 110-115.

[68] T. Clarcke, F. Simonetti and P. Cawley, “Guided wave health monitoring of complex structures by sparse array systems: Influence of temperature changes on performance,” *Journal of Sound and Vibration,* pp. 2306-2322, 2010.

[69] NDT resource center, “NDT resource center,” [Online]. Available: http://www.ndt-ed.org/EducationResources/CommunityCollege/Other%20Methods/AE/AE_Theory-Sources.htm. [Accessed 23 10 2013].

[70] F. L. d. Scalea and S. Salamone, “Temperature effects in ultrasonic Lamb wave structural health monitoring systems,” *Journal of Acoustical Society America,* pp. 161-174, 2008.

[71] F. Murnaghan, “Finite deformations of an elastic solid,” *American Journal of Mathematics,* pp. 59: 235-260, 1937.

[72] A. Gower, M. Destrade and R. Ogden, “Counter-intuitive results in acouste-elasticity,” *Wave Motion,* 2013.

[73] R. Pullin, J. Hensman, K. Holford and K. Worden, “A Principal Component Analysis of Acoustic Emission Signal from a Landing Gear Component,” *Key Engineering Materials* , vol. 347, pp. 139-144, 2007.

[74] R. Martin, J. Michaels and T. Michaels, “Ultrasonic characterization of thermal gradients in a homogenous plate,” *American Institute of Physics,* 2008.

[75] D. Husson, “A pertubation theory for acoustoelastic effect of surface waves,” *Journal of applied physics,* pp. 57: 1562-1568, 1985.

[76] Wikipedia, “Wikipedia,” Wikipedia, 03 11 2013. [Online]. Available: http://en.wikipedia.org/wiki/Aircraft_maintenance_checks. [Accessed 06 01 2014].

[77] J. Sinke, “lecture slide AE4760 Aircraft Structural Integrity & Maintenance,” Delft University of Technology, Delft, 2014.

[78] F. Ciampa and M. Meo, “A new algorithm for acoustic emission localilzation and flexural group velocity determination in anisotropic structures,” *Elsevier: Composits,* pp. 1777-1786, 2010.

[79] NDT.ed, “ndt-ed,” 2013. [Online]. Available: www.ndt-ed.net. [Accessed 2013].

[80] J. Ignaczak and M. ostoja-Starzewski, Thermoelasticity with Finite Wave Speeds, New York: Oxford University Press, 2009.

Appendix A: Design & Properties of Aluminium Plate

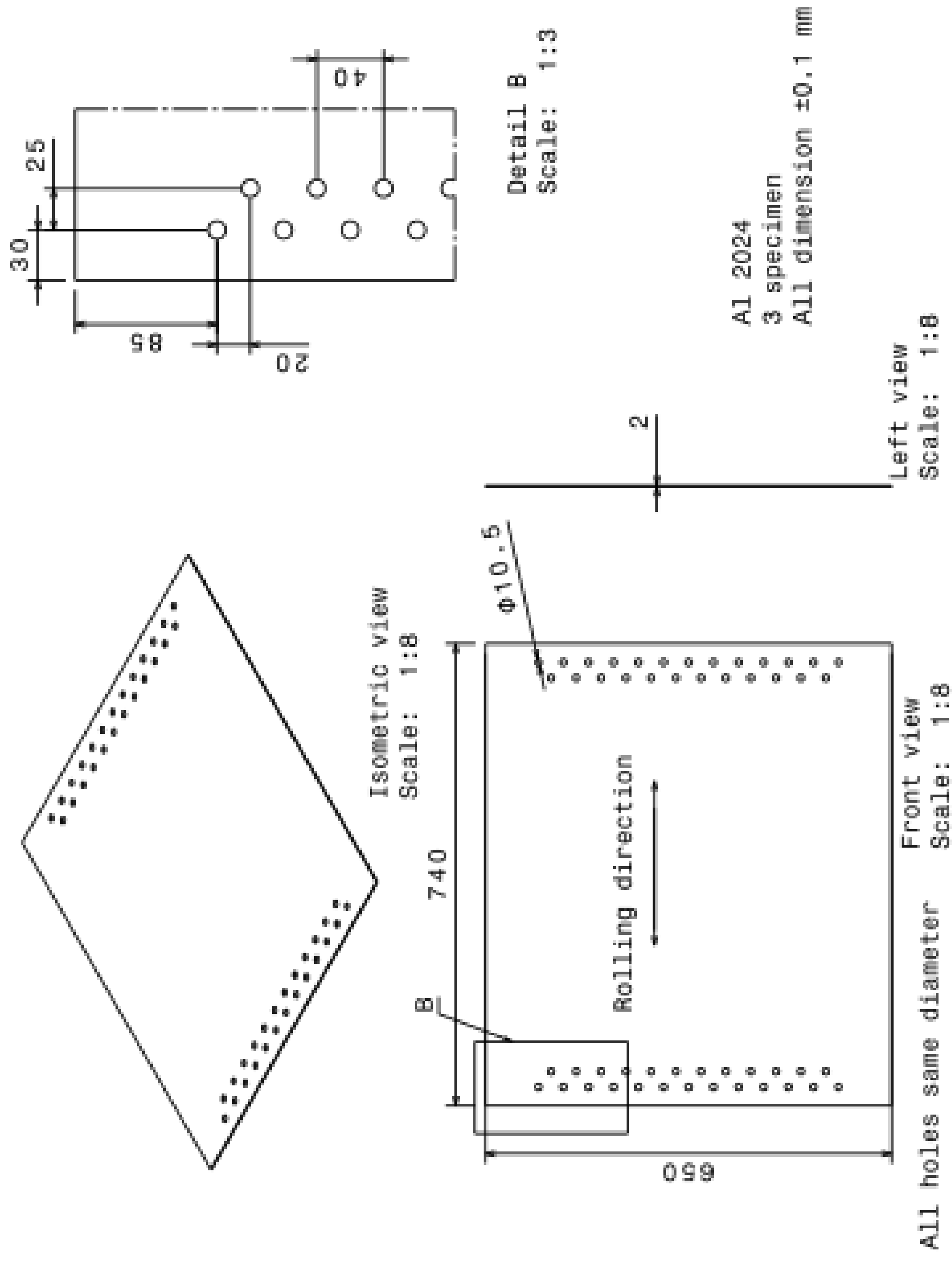

Figure B.1: Overview of test specimen, sizes are expressed in mm.

Properties of Aluminium 2024

Stiffness (Comsol Multiphysics®):

$8.1033434 \cdot 10^{10} + 2.123766 \cdot 10^{6}T - 1.972676 \cdot 10^{5} + 443.523T^{3} - 0.3697696T^{4}$ [K]

Poison ratio (Comsol Multiphysics®):

$0.3238668 + 3.754548 \cdot 10^{-6}T + 2.213647 \cdot 10^{-7}T^{2} - 6.5650233 \cdot 10^{-10}T^{3} + 4.21277 \cdot 10^{-13}T^{4} + 3.170505 \cdot 10^{-16}T^{5}$ [-]

Density (Comsol Multiphysics®):

$2813.898 + 0.02810998T - 7.443022 \cdot 10^{-4}T^{2} + 1.039896 \cdot 10^{-6}T^{3} - 3.5689519 \cdot 10^{-10}T^{4}$ [kg/m^3]

Density at room temperature (ASM [54]):

2780 [kg/m^3]

Coefficient of thermal expansion:

$2.322 \cdot 10^{-5}$ [-]

Appendix B: Design of Environmental Chamber

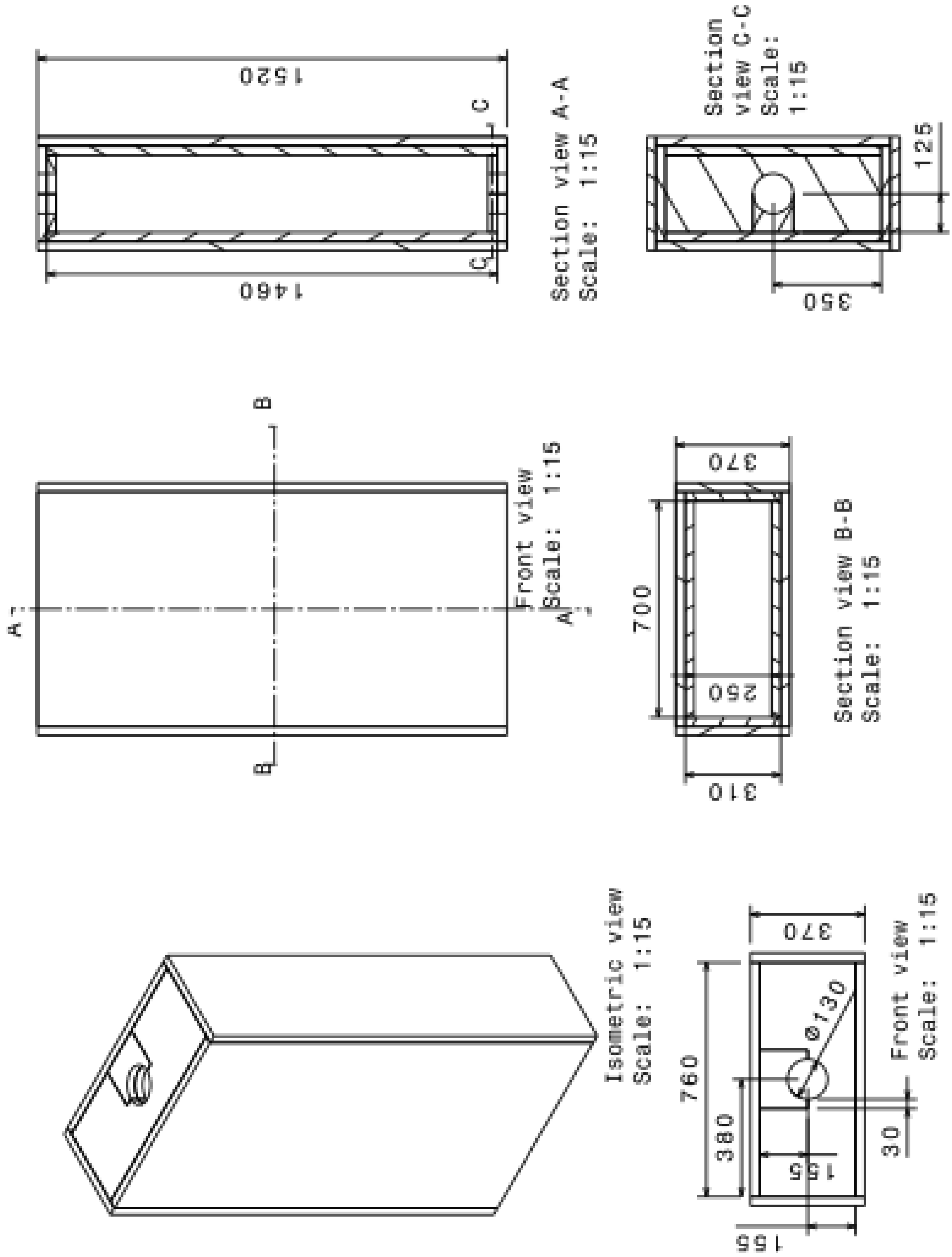

Figure C.1: Overview of environmental chamber, sizes are expressed in mm.

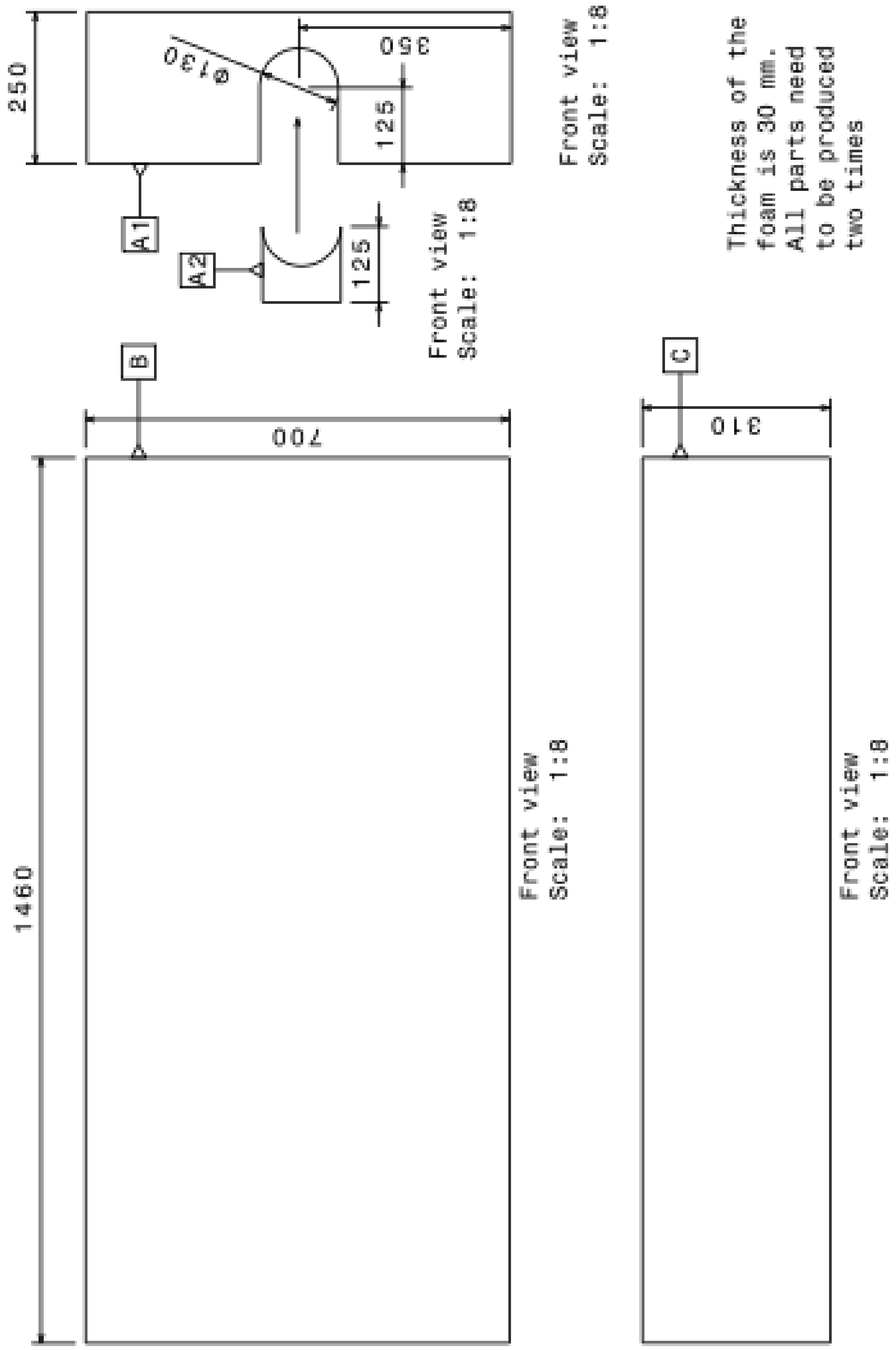

Figure C.2: Inner layer of environmental chamber, sizes are expressed in mm.

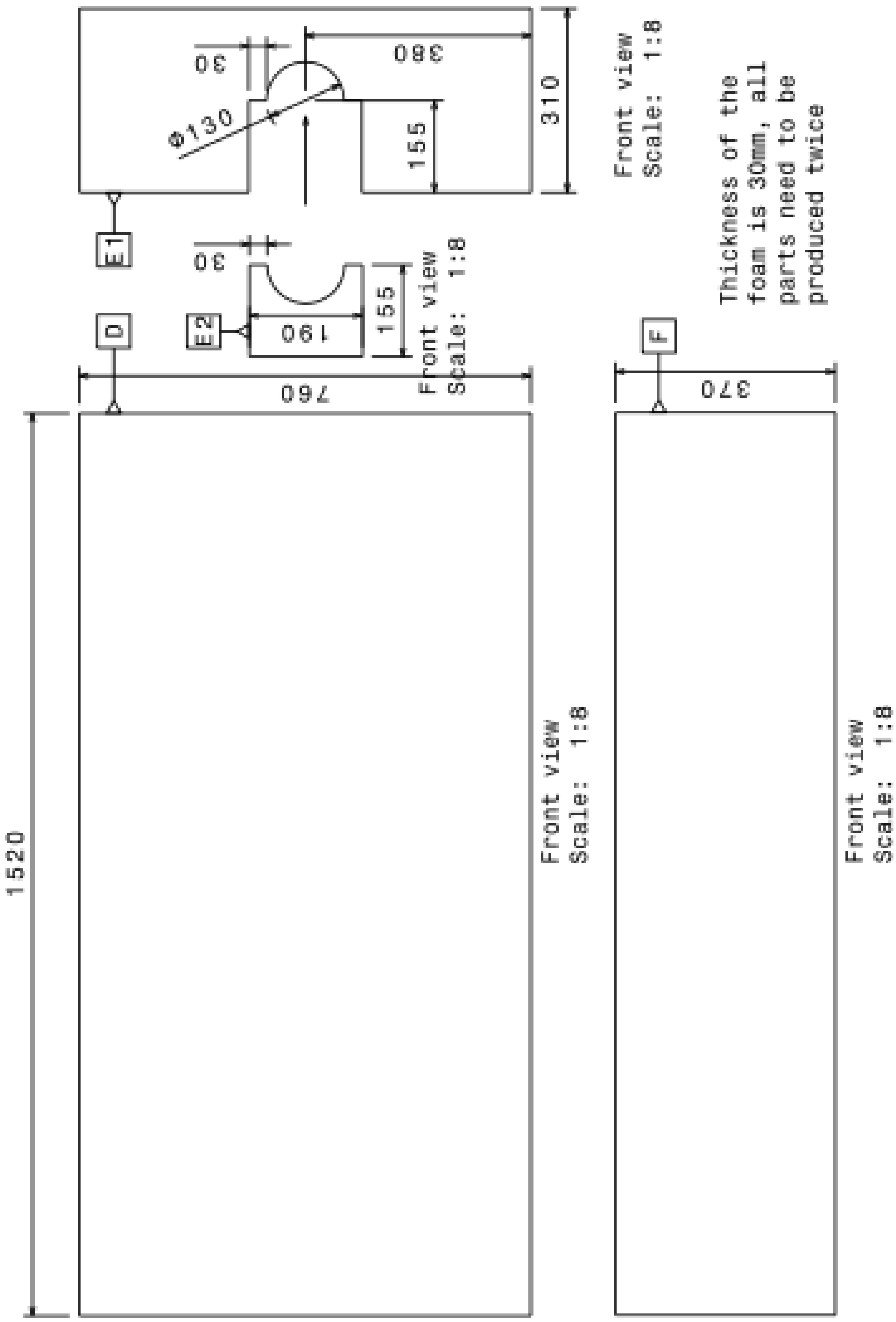

Figure C.3: Outer layer of environmental chamber, sizes are expressed in mm.

Appendix C: Data sheet piezoelectric transducers VS150-M (Vallen systems)

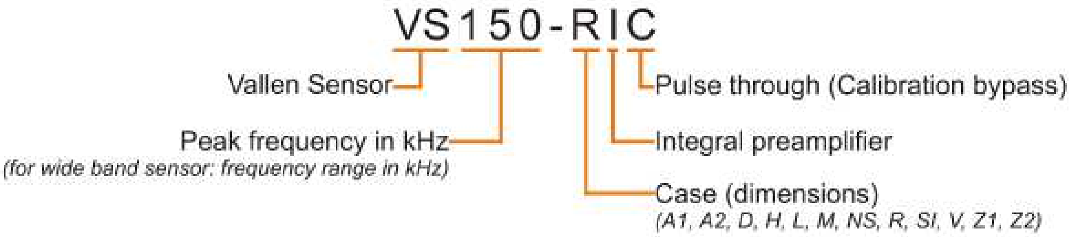

Figure C1: Explanation name classification of Vallen sensor types [59].

AE-sensor Model	Freq. Range [kHz]	f_{Peak} [kHz]	Freq. Resp. curve on page	Size DxH [mm]	Weight [g]	Case Material	Wear Plate	Temp. Range [°C]	Connector	Capa-city [pF]	Comment	Magnetic holder
VS150-M	100-450	150	14	20.3 x 14.3	23	Stainless steel	Ceramics	-50 to +100	Microdot	350		MAG4M

Figure C2: Sensor specification [59].

VS150-M

The VS150-M AE-sensor has a very high sensitivity and is the ideal choice for integrity testing of metal as well as composite structures.

Figure C3: Sensor sensitivity curve.

The piezoelectric coupling matrix relates stress to charge and it is constructed in the following manner. A state of stress in a medium is generally specified by a second order tensor with nine entries. The polarization of any crystal is specified for three components in the three main directions, this leads then to 27 electrical coupling constants. Based on thermodynamic reasoning it can be proven that $d_{ijk} = d_{ikj}$ [67]. This reduces the amount of constants to 18, which can be written using Voigt notation see Table 2.4.1 & Figure 2.4.3.

Table C1: Tensor notation, Voigt notation and Cartesian notation, which are visualized in Figure BNM.

Tensor notation	11	22	33	23, 32	31, 13	12, 21
Voigt notation	1	2	3	4	5	6
Cartesian notation	X	y	z	zy,yz	zx,xz	xy, yx

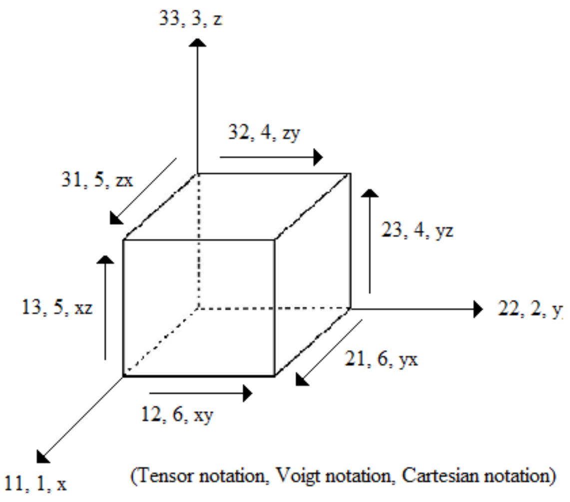

Figure C4: Tensor sub indices notation visualized for: Voigt and Cartesian notation.

PROPERTIES OF PIEZOCERAMIC MATERIAL NCE 51

Properties	Symbol & Unit	Value
DIELECTRICAL PROPERTIES (tolerances ±10%)		
Permittivity	$\varepsilon^T_{33} / \varepsilon_o$	1850
Dielectric Loss Factor	$tg\delta$ $[10^{-4}]$	190
ELECTROMECHANICAL PROPERTIES (tolerances ±5%)		
Coupling Factor	K_p	0.65
Coupling Factor	K_{31}	0.37
Coupling Factor	K_{33}	0.72
Coupling Factor	K_t	0.51
Piezoelectric Charge Constant	$-d_{31}$ $[10^{-12}\ C/N]$	195
Piezoelectric Charge Constant	d_{33} $[10^{-12}\ C/N]$	460
Piezoelectric Voltage Constant	$-g_{31}$ $[10^{3}\ Vm/N]$	13
Piezoelectric Voltage Constant	g_{33} $[10^{3}\ Vm/N]$	27
MECHANICAL PROPERTIES (tolerances ±5%)		
Elastic Compliance	s^E_{11} $[10^{-12}\ m^2/N]$	16
Elastic Compliance	s^E_{33} $[10^{-12}\ m^2/N]$	19
Radial Frequency Constant	N^E_p [m/s]	1940
Thickness Frequency Constant	N^D_t [m/s]	2010
Transverse Frequency Constant	N^E_1 [m/s]	1400
Longitudal Frequency Constant	N^D_3 [m/s]	1390
Mechanical Quality Factor	Q_m	80
Density	ρ $[10^3\ kg/m^3]$	7.8
THERMAL PROPERTIES		
Curie Temperature	T_c [°C]	340

Figure C5: Material specifications active element of VS150-M sensor.

Height piezoelectric element is 6.35 mm
Diameter piezoelectric element is 12.7 mm.

Appendix D: Background Noise levels

From Figure D1 it can be seen that the noise level at the hydraulic line is stronger than in the plate, indicating the source. Figure D2 and D3 zoom in and show that the measured response of this background noise in the sensors connected at the test specimen matches exactly the signal of channel 7.

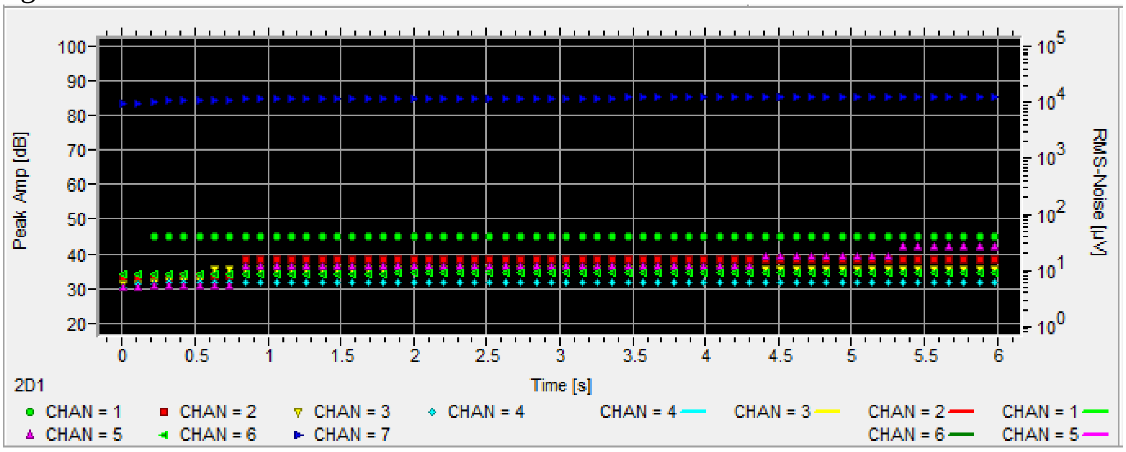

Figure D1: Background noise measurement.

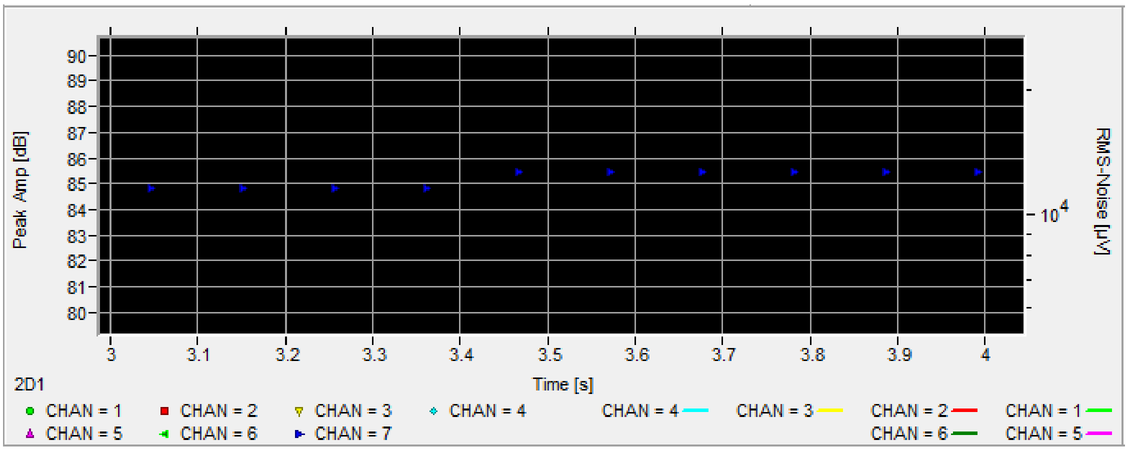

Figure D2: Close-up from sensor 7 at the hydraulic line from the fatigue bench.

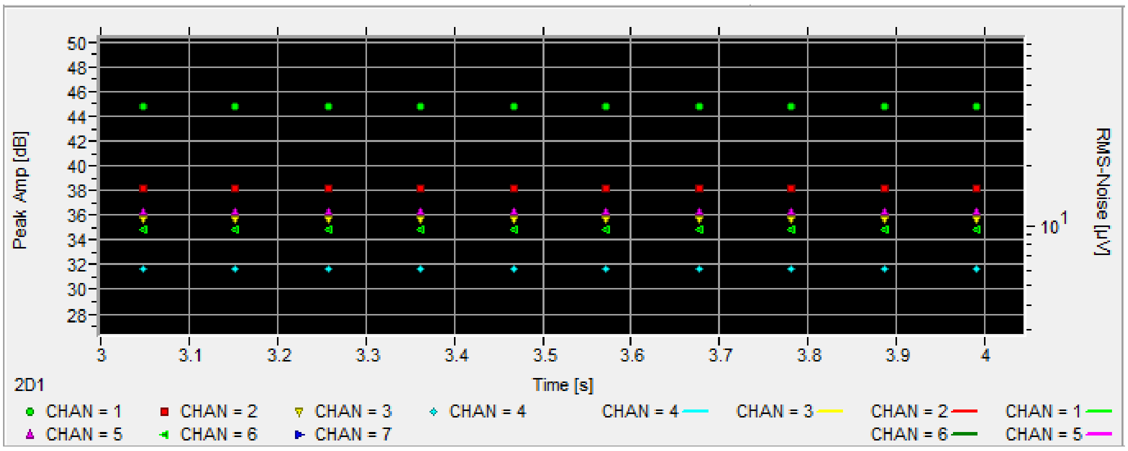

Figure D3: Close-up from sensors connected at the test-specimen.

Appendix E: Cluster Manual

Running in batch mode on the cluster

Manual for Comsol Multiphysics®, Comsol with Matlab, and Abaqus/CAE®

Authors: Rutger Stottelaar & Maurice Boon

Last update: 19/05/2014

This manual describes how to run Abaqus and Comsol Multiphysics® batch simulations on the cluster. First a short introduction is given that explains the general approach of running on the cluster. Then separate Sections for Comsol Multiphysics® and Abaqus® will discuss the details for each program in more detail.

Introduction

To run on the cluster the model input file and a job submission script (.pbs file) are required. When the two files have been produced they need to be uploaded to the cluster, this can be done by using filezilla or any other SSH client. Login entries are: Host (which is hpc12.tudelft.net), username, password and gate(which is: 22). Once the files have been uploaded onto the cluster the .pbs file can be executed to start running the model. The cluster can be controlled with PuTTY or Secure Shell Client (available on blackboard). To control your files on the cluster the commands in table 1 can be used.

Table E1: Cluster command to control cluster

ls	To see what files the current directory contains
cd	To go to beginning of directory on the cluster
cd ‘’*path*’’	To go to directory
Clear	Clears the screen of the interface
qsub ‘’*filename.pbs*’’	Submit .pbs file to the cluster
qsub -I	Submit a job file in which you can enter your own commands instead of having a .pbs file
qdel ‘’*job_ID_#*’’	Delete job, job-ID number can be found in list with ‘qstat’ command
qstat	To get overview of the submitted jobs on the cluster. This shows the total time of all CPU’s which have been running
qstat –a	To get more information of the submitted jobs, note: this shows how long jobs have been running on the cluster (real time)
qstat –u ‘’*netID*’’	Summarizes the jobs of the individual related to the netID
module avail	To show installed software packages on the cluster

When developing the job submission files (.pbs format), the link[3] explains some of the commands that are often used. In the next Sections examples will be shown these scripts.

[3] https://www.msi.umn.edu/resources/job-submission-and-scheduling-pbs-scripts

One convenient command from the link is the ‘’#PBS –q guest’’, which will run the batch on the cluster as a guest. This can significantly reduce waiting time.

<u>Comsol Multiphysics®</u>

To run in batch mode in Comsol multuphysics® first some internal settings need to be made. Note that these Figures are made in Comsol 4.4. Older versions of Comsol can have these options in different places.

In the model builder toolbar under the button select the advanced study options.

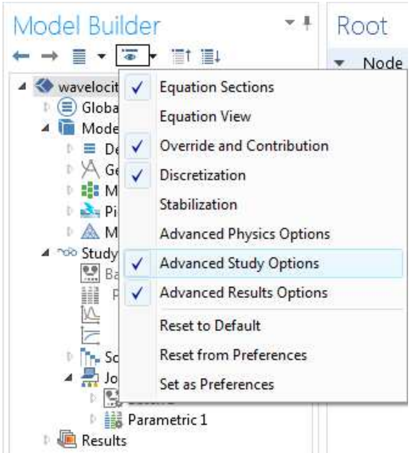

Then right mouse button on study and add ‘Batch‘.

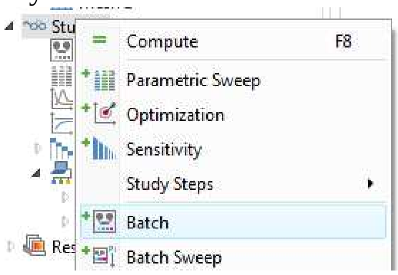

When clicking on the batch icon that just appeared will open a window on the right. In this window the filename, and directory on the cluster need to be specified. Next, right mouse button click on job configuration and again add batch.

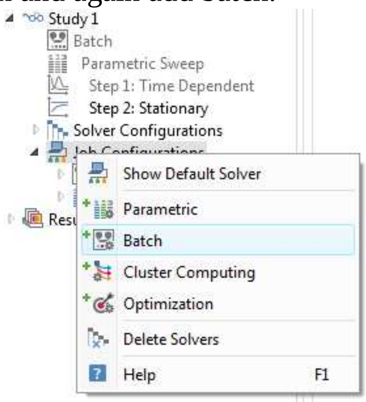

In the newly appeared batch menu select ‘Batch’ in the ‘Defined by study step’ line, and specify the number of ‘*jobs*’, ‘*alive time*’ and ‘*number of job restarts*’ if required.

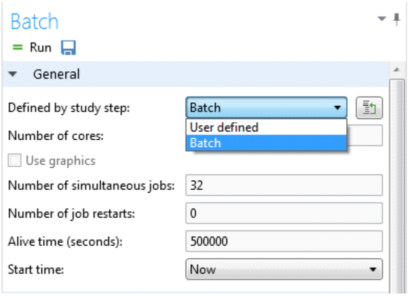

These are all the settings for the Comsol file to run, furthermore Comsol does not require to write an input file so the .mph file can be used to run on the cluster.
An example of a script in a .pbs file for Comsol is shown below:

```
#!/bin/bash
#PBS -N wavelocity            %specify name which is visible on the cluster
#PBS -l nodes=1:ppn=8              %specify nodes and cpu's (ppn), %this needs to
equal 'np' in
                                   the last line of this code
#PBS -M .......@student.tudelft.nl   %specify email address to get notification when job
                                   finishes.
#PBS -m abe                   %command required to send notifications
cd ~/wavevelocities           %specify folder where the documents are stored
inputfile=<file name>.mph          %specify input file
outputfile=<output file name>.mph  %specify output file
module load comsol/44              %specify Comsol version
comsol batch -np 8 -inputfile $inputfile -outputfile $outputfile -job b1 -batchlog
logpztFP02.log
```

Comsol with Matlab

Comsol with Matlab is used on the cluster if one wants to make use of the large amounts of memory available, or perform optimization runs. The use of Comsol with Matlab on the cluster is not as straightforward as using just Comsol. To start using Comsol with Matlab one first has to make a connection with the server manually, this is required just once.

Type in your command window of Putty (or other software you use to connect to the cluster): qsub –I

This enables a job where you can enter the commands instead of having a pbs file do that for you. Type: module load Matlab/2011b comsol/43b
This command will load the Matlab and Comsol modules which are available on the cluster, other versions of Matlab or Comsol are also possible. The next step is to type:
Comsol server

Wait for the cluster to respond, this may take a while. The cluster will ask for a username, type your netid without @tudelft.nl. The cluster will continue with asking your password, enter your password and confirm.

The next step is to prepare your Matlab script. Make sure two script lines are present in your file:
mphstart
model.save(<name of your mph document>)

Now you are ready to use the cluster to run your Matlab file to create a Comsol file. The Comsol file will be saved in the same folder as where the Matlab model is saved. Use the following .pbs script for the job.

```
#PBS -N Comsolopt                              %specify the name on the cluster
#PBS -o 'CNTMatlab.log'                        %specify your log file name
#PBS -l nodes=1:ppn=2                          % specify the amount of clusters
#PBS –M ……..@student.tudelft.nl                % specify email address to get notification when job finishes
#PBS -m abe                                    %command required to send notifications

module load Matlab/2011b comsol/43b            %specify which version you want to use
cd ~/model1/                                   %specify folder where the documents are stored
comsol server -np 2 -port 2036 < /dev/null > Comsolserver.log &
Matlab -nodesktop -nosplash -singleCompThread -r "addpath /opt/comsol43b/mli,
mphstart(2036), <your Matlab filename here>, exit" > Matlab.log
```

%specify the port number (this might take some trail and error). Furthermore change the Comsol version, and the amount of CPU’s if you have changed this value. The Matlab.log file will give the output of the Matlab command window.

Abaqus/CAE

Abaqus makes use of an input file on the cluster, which can be found under Analysis. Right mouse button click on jobs '*Create*'. Then under newly created job click with right mouse button and write input.

An example of a .pbs file for Abaqus looks almost the same as the previous pbs files shown. The file shown here contains more information than the Comsol version. A simple version as shown in the case of Comsol should be sufficient as well.

```
# Job for Torque PBS 2.0.0p8
# -----------------------------
#PBS -j oe
#PBS -o CF245_dam05_TR.LOG
#PBS -l nodes=1:ppn=16
#PBS -N CF245_dam05_TR
#PBS -S /bin/csh
# -------------------------------------
cd ${PBS_O_WORKDIR}
set wat=<File name>                                      %Input file name
set opt=(interactive cpus=16)                            %settings forAbaqus
# Note that in "Abaqus.$$" "$$" is an environment variable
#   which is replaced by the current unique process number
set waar=/var/tmp/Abaqus.$$
# Create temporary directory and copy files to it
mkdir ${waar}
#/bin/cp -p abaqus_v6.env ${waar}
/bin/cp -p ${wat}* ${waar}
# Go to temporary directory, run Abaqus and come back
pushd ${waar}
/opt/abaqus-6.11/Commands/abaqus job=${wat} ${opt}
popd
# Retrieve files and remove temporary directory
/bin/cp -p ${waar}/${wat}* .
/bin/rm -fr ${waar}
exit 0
```

Appendix F: Enlarged Figures of Chapter 5

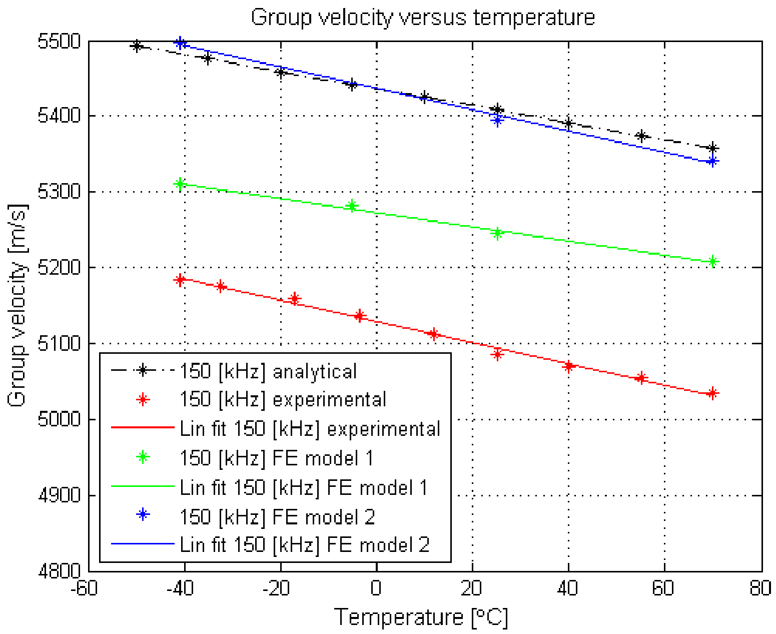

Figure 5.1.1a Wave group velocity versus temperature; analytical, experimental and FEM results for 150 kHz signal

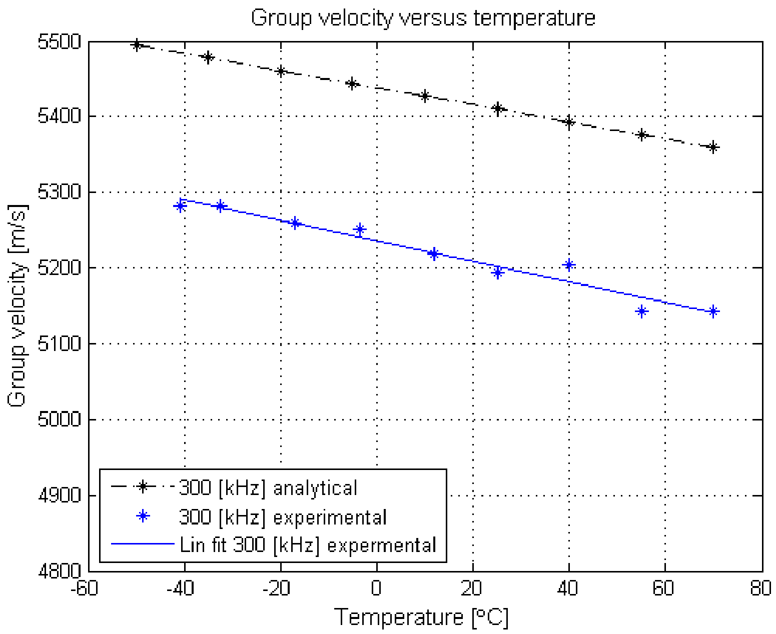

Figure 5.1.1b Wave group velocity versus temperature; analytical and experimental results for 300 kHz signal.

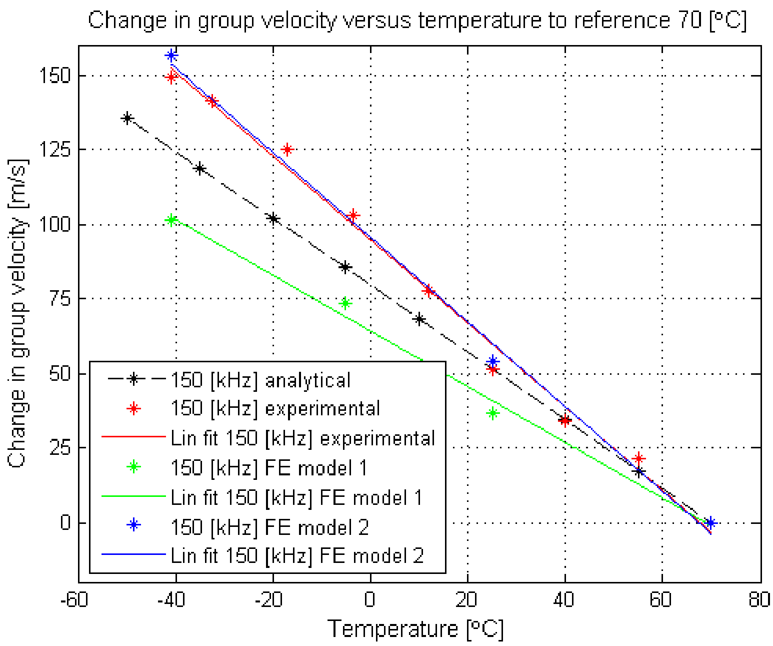

Figure 5.1.2a: Change in group velocity versus temperature with reference to 70 ˚C; analytical, experimental and FEM results for 150 kHz signal.

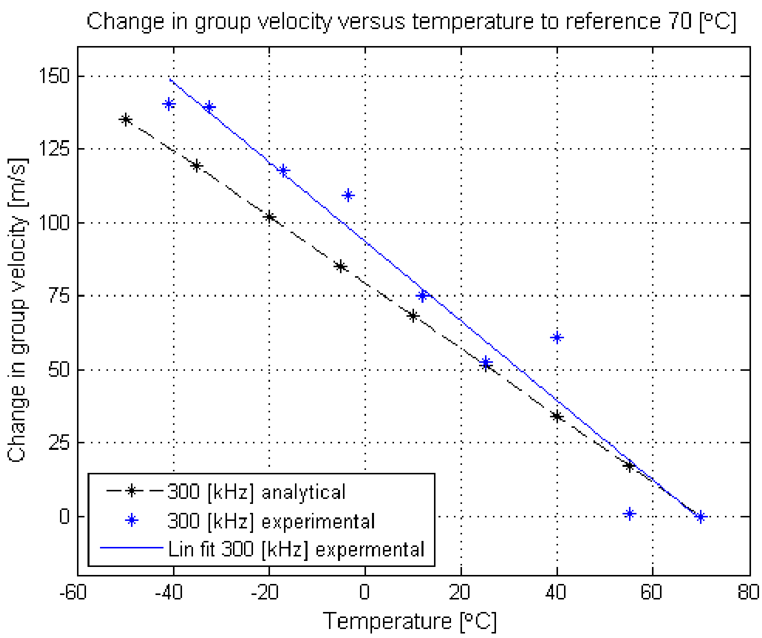

Figure 5.1.2b: Change in group velocity versus temperature with reference to 70 ˚C; analytical and experimental results for 300 kHz signal.

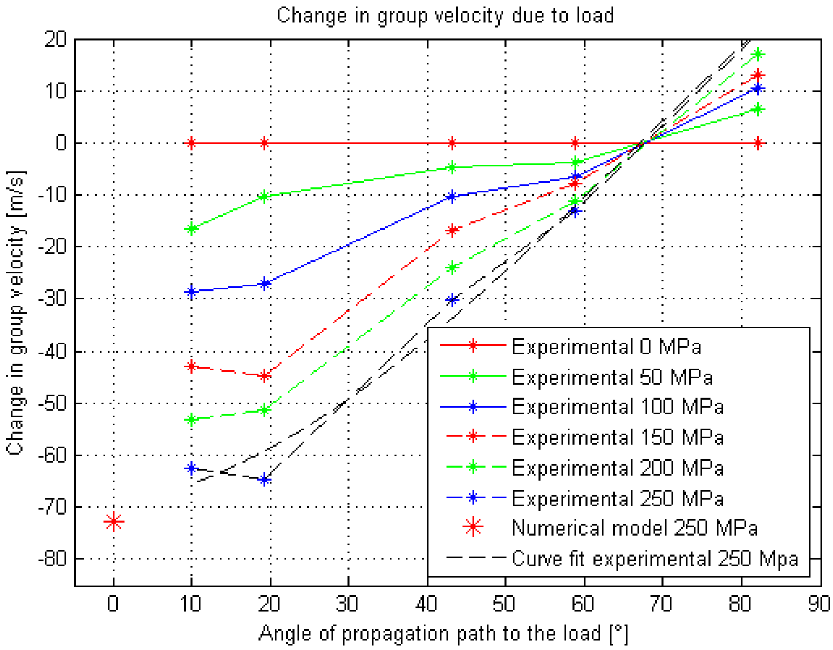

Figure 5.1.4a: Experimental results of the influence of load on change of wave group velocities. Change in group velocity for 150 kHz signal.

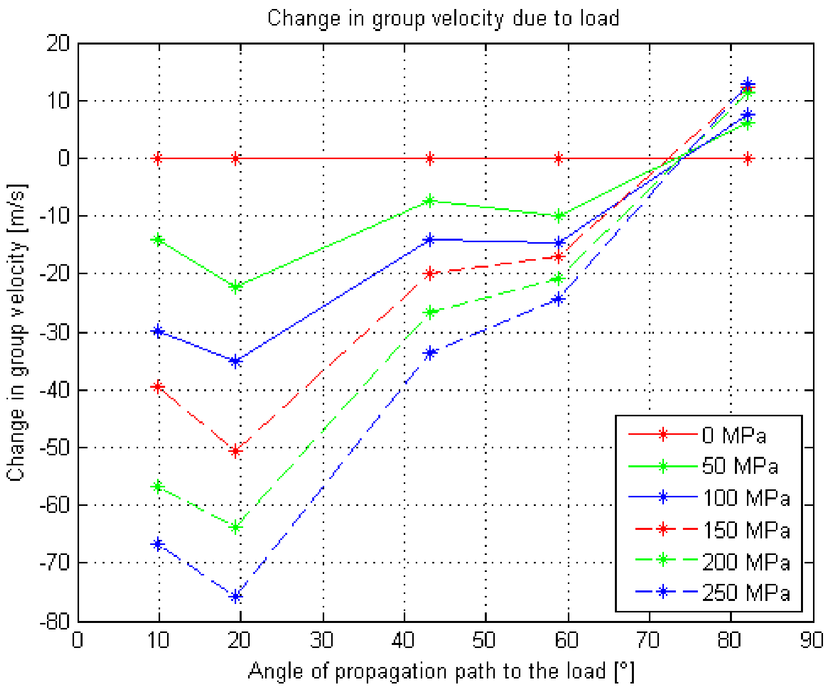

Figure 5.1.4b: Experimental results of the influence of load on change of wave group velocities. Change in group velocity for 300 kHz signal.

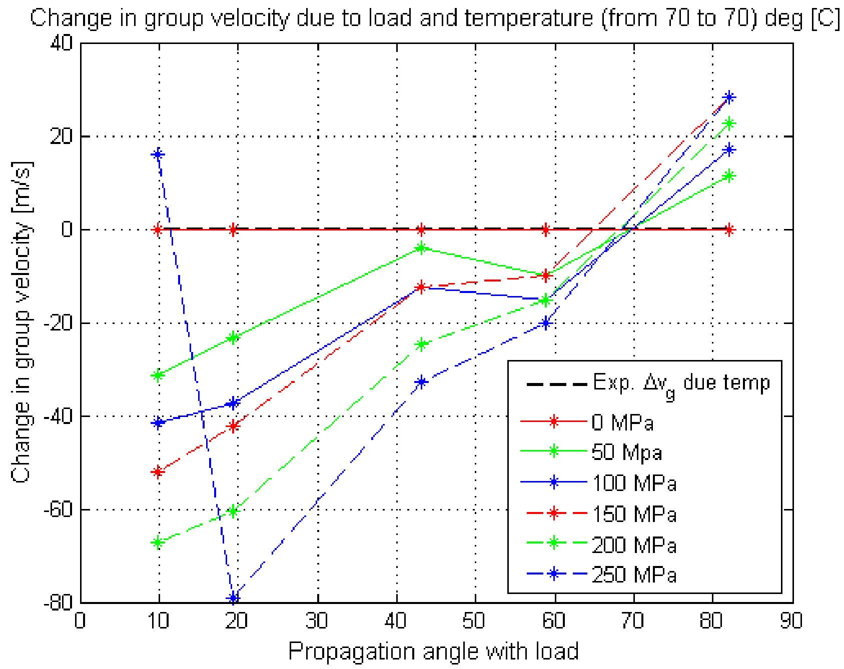

Figure 5.1.5a: The influence of load and temperature on change of wave group velocities, with reference to zero load case at 70 ˚C. Change in group velocity at -41 ˚C.

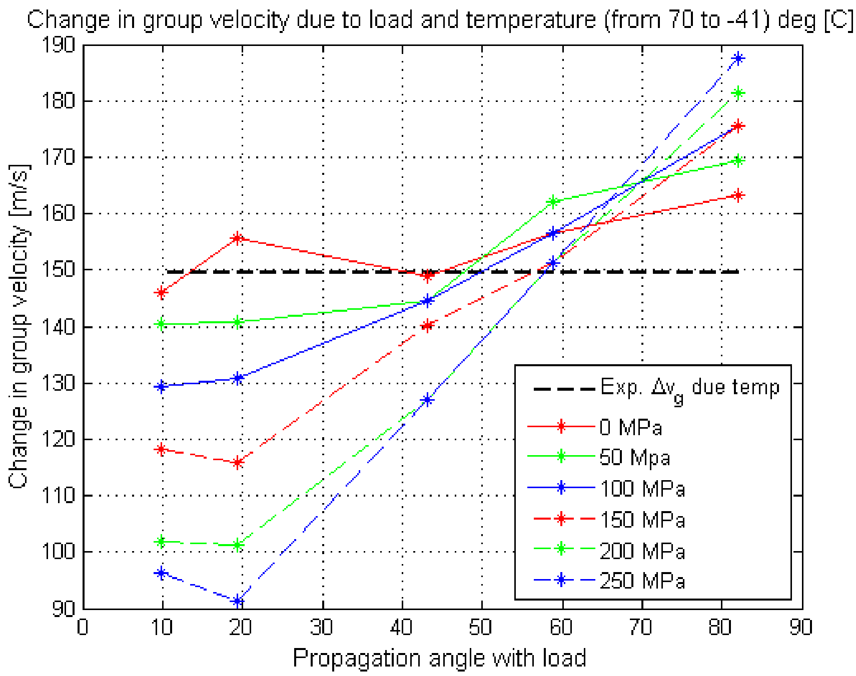

Figure 5.1.5b: The influence of load and temperature on change of wave group velocities, with reference to zero load case at 70 ˚C. Change in group velocity at -41 ˚C.

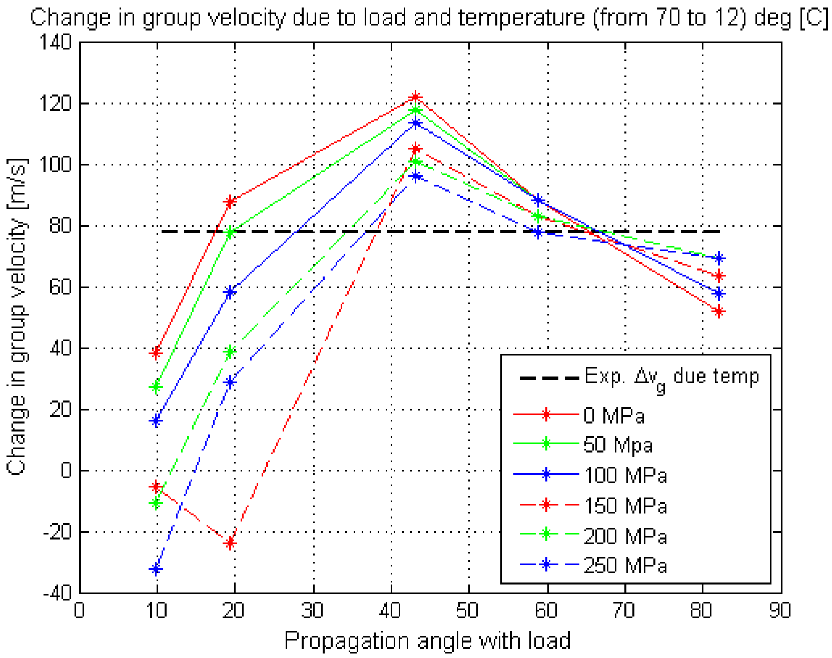

Figure 5.1.6a: The influence of load and temperature on change of wave group velocities, with reference to zero load case at 70 ˚C; for the case of 12 ˚C.

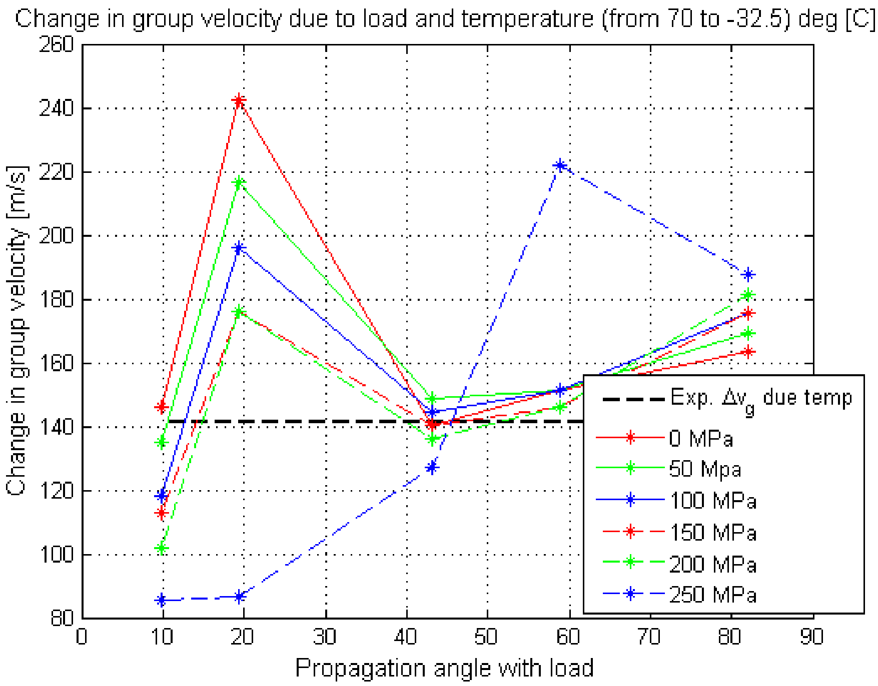

Figure 5.1.6b: The influence of load and temperature on change of wave group velocities, with reference to zero load case at 70 ˚C; for the case of -32.5 ˚C.

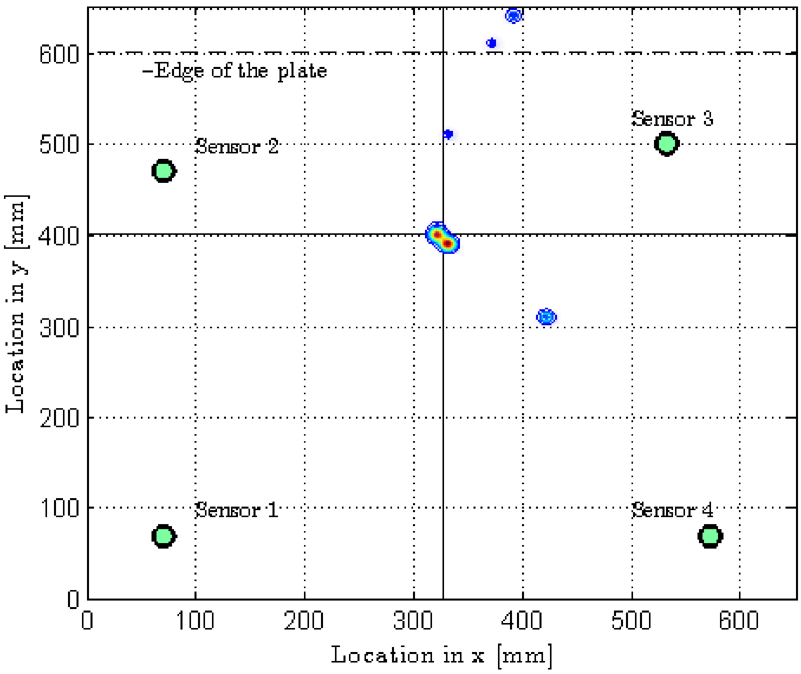

Figure 5.2.1a: Locations of AE signals for multiple EOC calculated by Vallen AE system, displayed with Parzen probability density; sensor and calculated locations for entire plate.

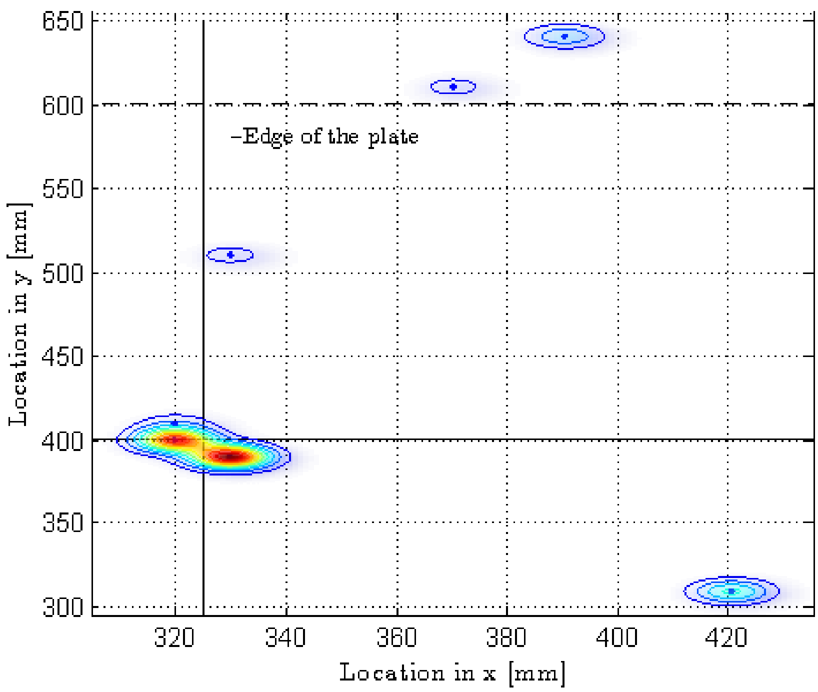

Figure 5.2.1b: Locations of AE signals for multiple EOC calculated by Vallen AE system, displayed with Parzen probability density; calculated locations for narrowed region.

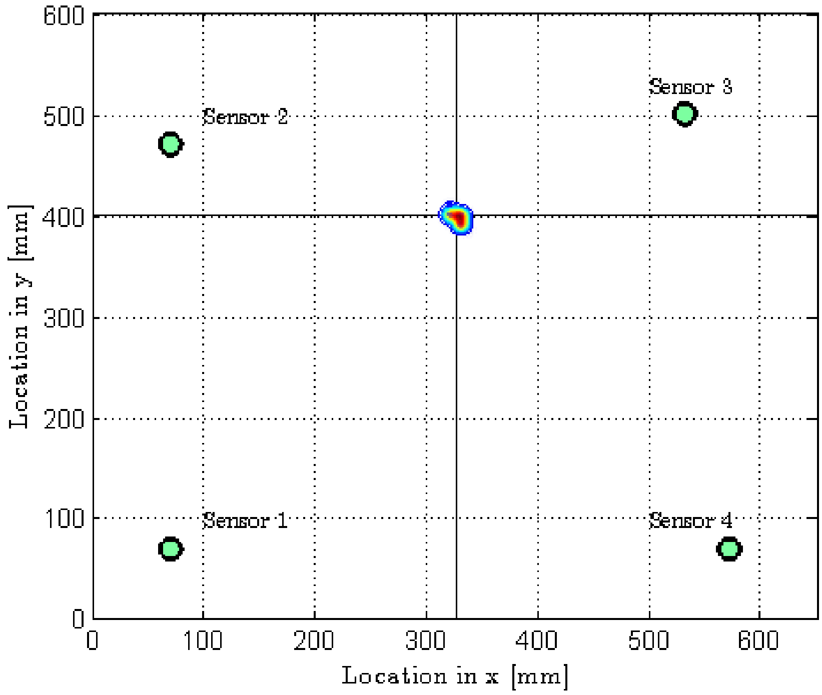

Figure 5.2.2a: Locations of Vallen internal pulse signals for multiple EOC calculated by Vallen AE system, displayed with Parzen probability density; sensor and calculated locations for entire plate.

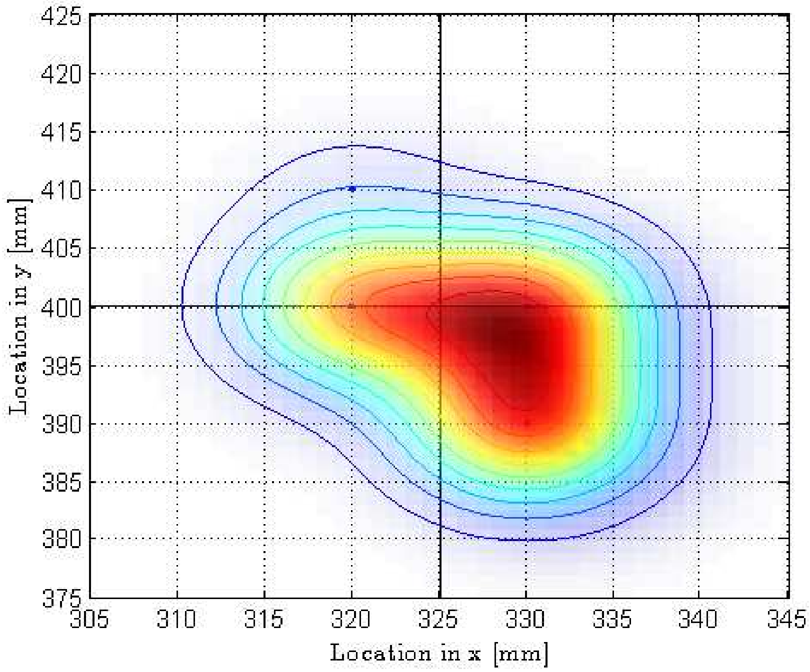

Figure 5.2.2b: Locations of Vallen internal pulse signals for multiple EOC calculated by Vallen AE system, displayed with Parzen probability density; calculated locations for narrowed region.